



POLITECNICO DI TORINO

Master Thesis in Electrical Engineering

# Black-box Commissioning of Grid Converters

*Author:* Luca Zeppegno

*Supervisor:* Prof. Radu Bojoi

*Advisor:* Fabio Mandrile

March 2020



# Abstract

The increase of grid-connected converters has highlighted the problem of harmonic interaction between multiple converters and the grid. This phenomenon can bring to network instabilities. A valid approach in order to study the stability of the overall system is to characterize the converter with a small-signal equivalent admittance model and stability analysis through the General Nyquist Criterion (GNC). This work analyses two different black-box methods to experimentally characterize the converter equivalent admittance model. The first method performs a voltage injection on grid side and evaluates the amplitude and phase of the converter current response. The second method performs steps on the grid voltage and evaluates the equivalent admittance based on the shape of the current transient response.

# Acknowledgements

I would first like to thank my thesis advisor Fabio Mandrile and my supervisor Radu Bojoi for their advice whenever I ran into a trouble spot or had a question about my research. They managed to steer me in the right the direction whenever they thought I needed it.

I must also express my very profound gratitude to my parents, my friends and to my girlfriend Francesca for providing me with unfailing support and continuous encouragement throughout my years of study and through the process of researching and writing this thesis. This accomplishment would not have been possible without them. Thank you.

Luca Zeppegno

# Contents

<b>List of Tables</b>	<b>iv</b>
<b>List of Figures</b>	<b>v</b>
<b>1 Introduction</b>	<b>1</b>
1.1 Forecasts on the Growth of Grid Converter Converters . . . . .	1
1.2 The Problem of Dynamic Interaction Between Converters . . . . .	5
1.3 The Small-Signal Admittance Model . . . . .	8
1.3.1 Example of the GNC applied to an equivalent admittance model . . . . .	10
1.4 Calculation of the Equivalent Admittance . . . . .	11
<b>2 Converter Model and Control</b>	<b>15</b>
2.1 Overall Circuit Scheme . . . . .	15
2.2 Overview of the Inverter Control Scheme . . . . .	18
2.2.1 Grid Synchronization Unit . . . . .	19
The Need for a Grid Synchronization Unit . . . . .	19
The $(d,q)$ Frame Based Phase-Locked Loop . . . . .	21
2.2.2 Tuning of the PLL PI Controller . . . . .	24
Normalized $(d,q)$ Frame Based Phase-Locked Loop . . . . .	25
Secondary Order Generalized Integrator (SOGI) . . . . .	28
2.2.3 Converter Current Control . . . . .	30
Converter Delay Transfer Function . . . . .	32
Current Loop Tuning . . . . .	33
Current Controller Feed Forward . . . . .	36

2.2.4	DC-Link Voltage Control . . . . .	37
2.2.5	Modulation Scheme . . . . .	40
2.3	DC/DC Converter Control . . . . .	44
2.4	PLECS Implementation . . . . .	46
2.5	C-Script Implementation . . . . .	46
<b>3</b>	<b>Impedance Measurement Through Signal Injection</b>	<b>55</b>
3.1	Problems of Signal Injection Methods Applied to Power Converters	56
3.2	Formulation of the Impedance Matrix . . . . .	57
3.2.1	Choice of the Perturbation Signal . . . . .	59
3.2.2	Signal Frequency Change in the $(d, q)$ Domain . . . . .	59
3.3	Mirror Frequencies Method . . . . .	60
3.4	RL Circuit Analysis Through Voltage Injection . . . . .	62
3.4.1	PLECS Implementation . . . . .	62
3.4.2	Processing of the Measurement . . . . .	65
3.5	RL Circuit Analysis Through Current Injection . . . . .	70
3.5.1	PLECS Implementation . . . . .	72
3.6	PLECS Simulation of Voltage Injection . . . . .	75
3.6.1	Inverter Average Value Equivalent Model . . . . .	76
3.6.2	Simulation Results . . . . .	77
	Equivalent admittance with Current Loop . . . . .	77
	Equivalent admittance with DC Voltage Loop . . . . .	78
	Equivalent admittance with Two-Stage Converter . . . . .	80
3.7	Experimental Validation of Voltage Injection . . . . .	82
3.7.1	Description of the Experimental Setup with an RL Circuit .	82
	Real-Time Simulator . . . . .	82
	Experimental Results . . . . .	85
3.7.2	Experimental Measurement with Grid-Connected Converter	87
<b>4</b>	<b>Impedance Estimation Through Transient Analysis</b>	<b>95</b>
4.1	System Identification Overview . . . . .	96
4.1.1	Identification Procedure . . . . .	96
4.1.2	Type of model . . . . .	98

4.1.3	Main Parametric Methods . . . . .	98
	AR Models . . . . .	100
	ARX Models . . . . .	100
4.1.4	OE Models . . . . .	102
4.1.5	ARMAX Models . . . . .	102
	BJ Models . . . . .	102
4.2	RL Circuit Identification . . . . .	103
4.2.1	PLECS Implementation . . . . .	103
4.2.2	Identification Procedure . . . . .	104
4.3	Simulation of Converter Identification . . . . .	109
4.3.1	Simulation Results of Equivalent Admittance Measurements	111
	Identification of Converter with Output Current Control . .	111
	Identification of Converter with Output Current and DC	
	Voltage Control . . . . .	113
<b>5</b>	<b>Conclusions</b>	<b>119</b>
<b>A</b>	<b>PLL Sizing Insights</b>	<b>123</b>
	PI Controller Sizing through the Open Loop Transfer Function	123
<b>B</b>	<b>Considered Transformation Matrices</b>	<b>127</b>
	Amplitude Invariant Clarke Transformation . . . . .	127
	Inverse Clarke Transformation . . . . .	128
	Rotation Transformation $\mathbf{R}(\theta)$ . . . . .	128
	Inverse Rotation Transformation $\mathbf{R}^{-1}(\theta)$ . . . . .	129
<b>C</b>	<b>PLECS Code for the C-Script Block</b>	<b>131</b>
	Output function code . . . . .	131
<b>D</b>	<b>Signal Injection Insights</b>	<b>137</b>
	(d,q) Impedance of an RL Circuit . . . . .	137
	PLECS Voltage Perturbation Generation Code . . . . .	139
	PLECS Signal Perturbation Data Processing Code . . . . .	140
	<b>Bibliography</b>	<b>145</b>

# List of Tables

2.1	Converter values. . . . .	16
2.2	PLL set-up values. . . . .	25
2.3	PLL set-up values with voltage normalization. . . . .	28
2.4	Errors of various Padè approximations with respect to the non approximated transfer function of the converter delay. . . . .	34
2.5	Current loop set-up values. . . . .	35
2.6	Voltage loop set-up values. . . . .	40
2.7	DC/DC converter current loop set-up values. . . . .	46
3.1	Converter values. . . . .	88
4.1	Values used in the PLECS simulation of Fig. 4.2 . . . . .	104
4.2	Admittance identification methods and orders for the admittance measurement with only current control. . . . .	112
4.3	Admittance identification methods and orders for the admittance measurement with current and voltage control. . . . .	113
A.1	PLL setup values. . . . .	124

# List of Figures

1.1	Forecast on solar and wind electricity gross production until 2050 (GWh). . . . .	2
1.2	Evolution of EV market shares divided by region. Source: [15] . . .	3
1.3	Scenarios of EV market share future trends. Source: [15] . . . . .	4
1.4	Trend of the last years on growth of the number of battery chargers. Source: [15]. . . . .	4
1.5	Thevenin and Norton equivalent circuit of a converter and Thevenin equivalent circuit of grid. . . . .	7
1.6	Thevenin equivalent circuit of multiple converters and Thevenin equivalent circuit of grid. . . . .	9
1.7	Closed loop equivalent of $\mathbf{H}(s)$ . . . . .	10
1.8	GNC example to determine the stability of an overall system. . . .	11
1.9	<i>PLECS</i> simulation with 10 converters working as active rectifiers. . .	11
1.10	Grid voltages and currents in a <i>PLECS</i> simulation with 10 converters working as active rectifiers. . . . .	12
2.1	Diagram of the considered system. . . . .	17
2.2	Overview of adopted control scheme. . . . .	18
2.3	Position of the voltage vector with respect to the different stationary and rotating reference frames. . . . .	19
2.4	Block diagram of the Phase-Locked Loop. . . . .	23
2.5	Block diagram of the Phase-Locked Loop in the Laplace domain. . .	23
2.6	Bode diagram of the PLL open and closed loop transfer functions. . .	26

2.7	<i>PLECS</i> simulation of a PLL calibrated as in Table 2.2 while feeded by an ideal voltage. . . . .	27
2.8	Structure of a <i>SOGI</i> resonant filter. . . . .	28
2.9	Comparison of various Padè approximations. . . . .	33
2.10	Block representation of the current loop in the Laplace domain. . .	34
2.11	Bode diagram of the open loop and closed loop transfer function of the current control. . . . .	36
2.12	Block representation of the feed forward of the current loop controller. .	37
2.13	Block representation of the inverter cascaded control. . . . .	37
2.14	Block representation of the inverter DC-Link voltage loop. . . . .	38
2.15	Bode diagram of the open loop and closed loop transfer function of the voltage control. . . . .	41
2.16	Block diagram representing the full control of the inverter. . . . .	42
2.17	Block diagram of the Balanced Envelope Modulation . . . . .	44
2.18	Adopted DC/DC converter (boost). . . . .	45
2.19	DC/DC converter current loop. . . . .	45
2.20	DC/DC converter Bode diagram for the current loop. . . . .	47
2.21	DC/DC converter control block diagram. . . . .	47
2.22	<i>PLECS</i> representation of the converter and grid circuit. . . . .	48
2.23	<i>PLECS</i> representation of the converter control. . . . .	49
2.24	<i>SOGI</i> block representation. . . . .	50
3.1	Simplified single-line diagrams of signal injection test circuits. . . .	56
3.2	Signal Injection Scheme. . . . .	61
3.3	<i>PLECS</i> equivalent of a voltage injection test for an RL circuit. . . .	63
3.4	Voltages and currents with a voltage perturbation at 1 Hz. . . . .	64
3.5	Flow Chart of the Voltage Injection Algorithm. . . . .	66
3.6	Voltages and currents in the $(d, q)$ frame with a voltage perturbation at 1 Hz. . . . .	67
3.7	Comparison between measured points (in blue) and analytical transfer function (in orange) for a RL circuit when injecting voltage perturbations. . . . .	69
3.8	Subsystem used for the current perturbation. . . . .	70

3.9	Thevenin equivalent circuit at different frequencies from the grid frequency. . . . .	71
3.10	Voltages and currents with a current perturbation at 1 Hz. . . . .	73
3.11	Comparison between measured points (in blue) and analytical transfer function (in orange) for a RL circuit when injecting current perturbations. . . . .	74
3.12	PLECS equivalent of a voltage injection test for a grid converter. . . . .	76
3.13	PLECS average value equivalent circuit of the three-phase inverter and DC imposed current. . . . .	76
3.14	Comparison between the theoretical calculation and the measured admittance when considering a simulation with only current loop and $I_d = 10A$ and $I_q = 0A$ in rectifier mode. . . . .	78
3.15	Comparison between the theoretical calculation and the measured admittance when considering a simulation with voltage and current control with $I_d = 10A$ and $I_q = 0A$ . The theoretical calculation does not consider a decoupling term on the output of the current controller. . . . .	79
3.16	Comparison between the theoretical calculation and the measured admittance when considering a simulation with voltage and current control with $I_d = 10A$ and $I_q = 0A$ . The theoretical calculation considers a decoupling term on the output of the current controller. . . . .	80
3.17	Comparison between the equivalent admittance of a two-stage converter and the one of a single stage converter with DC voltage loop and AC current loop. Both solutions were computed considering a rectifier operation with $I_d = 10A$ and $I_q = 0A$ . . . . .	81
3.18	Experimental setup components. . . . .	83
3.19	Single-line block diagram of the experimental setup. . . . .	84
3.20	<i>PLECS</i> RT Box model . . . . .	85
3.21	Flow chart of the frequency selection script. . . . .	86
3.22	Experimental results of the measurements of the RL circuit through voltage injection. . . . .	87
3.23	Converter experimental set-up pictures. . . . .	89

3.24	Experimental Measurement of PCC line voltages and output currents in the three-phase and in the $(d, q)$ reference frame. . . . .	90
3.25	Comparison between the experimental measurements of the equivalent admittance of the considered grid-connected converter and the theoretical solution. . . . .	91
3.26	Comparison between the experimental measurements of the equivalent admittance of the considered grid-connected converter and the theoretical solution. . . . .	92
4.1	Block diagrams of main identification models. . . . .	99
4.2	PLECS schematic of the RL transient analysis circuit used for the identification. . . . .	103
4.3	Voltage step and current transient in the three phase reference frame.	105
4.4	Voltage step and current transient in the $(d, q)$ reference frame. . .	106
4.5	Bode diagram of identified RL admittance transfer function (in blue) when data is sampled at 10 kHz. For comparison the correct theoretical admittance is also reported (orange). . . . .	107
4.6	Bode diagram of identified RL admittance transfer function (in blue) when data is sampled at 1 MHz. For comparison the correct theoretical admittance is also reported (orange). . . . .	108
4.7	Comparison between identification methods for the estimation of $Y_{dd}$	109
4.8	Test circuit for output voltage controlled VSI. . . . .	110
4.9	Transient analysis method test circuit. . . . .	111
4.10	Block diagrams of main identification models. . . . .	112
4.11	<i>PLECS</i> simulation of voltage steps and relative current transients for a converter with only current control. . . . .	115
4.12	Comparison between theoretical equivalent admittance and measured admittance through transient analysis method when only output current control is considered. . . . .	116
4.13	Comparison between theoretical equivalent admittance and measured admittance through transient analysis method when both output current control and DC voltage control are considered. . . . .	117

4.14	Comparison between estimated system response to a $v_d$ step through measured impedance and simulation data. . . . .	118
4.15	Comparison between estimated system response to a $v_q$ step through measured impedance and simulation data. . . . .	118
A.1	Bode diagram of $G_{OL,PLL}$ and $G_{CL,PLL}$ . . . . .	125

# Chapter 1

## Introduction

### 1.1 Forecasts on the Growth of Grid Converter Converters

The presence of grid connected converters has greatly increased in the past few decades and, according to the majority of forecasts, this growth is not going to stop in the following years. Almost all forecasts on future trends of renewable energy and battery chargers consider a relevant growth, and this is common even to the most conservative scenarios.

The first considered scenario is the *EU Reference Scenario 2016* [8], which is the European Commission's key analysis tool in the area of energy. It provides a reference scenario that forecasts variations in energy production and use up to 2050.

This scenario forecasts a great increase in energy production from solar and wind in the next 30 years, as shown in Fig. 1.1. Energy from solar sources is expected to grow 177% from 2020 to 2050, passing from 155 TWh in 2020 to 429 TWh in 2050. Energy from wind sources will grow by 112%, passing from around 463 TWh in 2020 to 980 TWh in 2050.

These renewable sources are interfaced with the grid through power converters, thus the increase in converters for renewables is expected to follow the same trend.

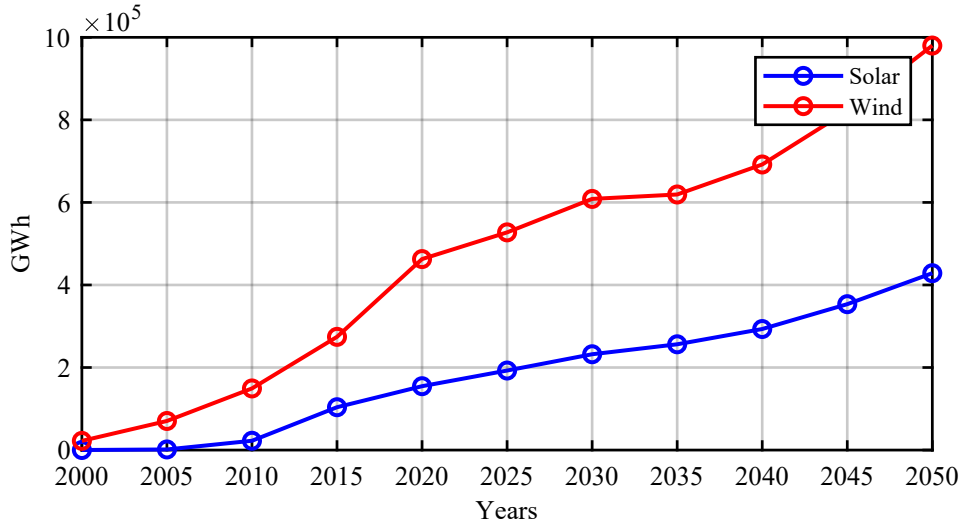


Figure 1.1: Forecast on solar and wind electricity gross production until 2050 (GWh).

Another example of future power electronics converters application are the EV<sup>1</sup> battery chargers. The most complete publication on recent developments and future trends in electric mobility is the *IEA Global EV Outlook 2019* [15]. According to this document, the number of electric cars that were sold in the recent years is considerably low if compared to conventional petrol and diesel based vehicles. However, Fig. 1.2 shows that in the past few years PHEV<sup>2</sup> and EV market share has continuously grown, with a great impulse given from the Chinese market. As for European market, there is a constant growing trend on the number of electric vehicles sold, with Northern Europe countries as leaders.

[15] presents some future scenarios that can be foreseen based on the EV and PHEV market share trend over the past few years. The main two are shown in Fig. 1.3. One of them, the *New Policies Scenario*, is more cautious than the other, and guesses a total number of around 50 million EV units in 2025 and a bit less than 150 million units in 2030. Despite this difference, both scenarios agree on a substantial increase on the number of electric vehicles.

Both EV and PHEV require chargers for their batteries. Such chargers may

<sup>1</sup>Electric vehicle

<sup>2</sup>Plug-In Hybrid Electric Vehicles

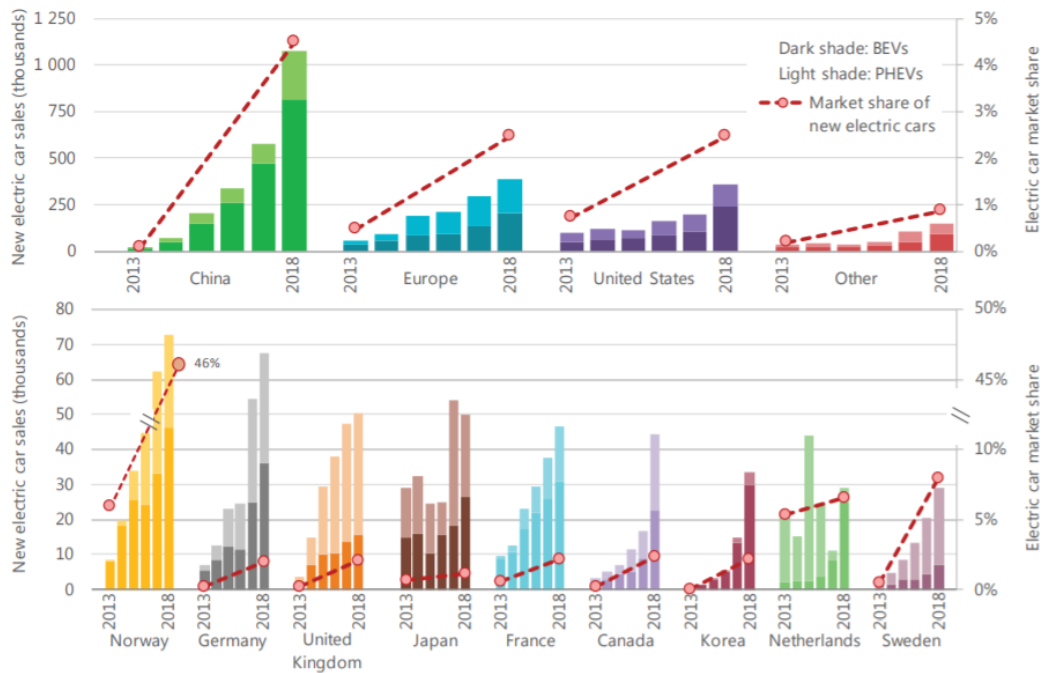


Figure 1.2: Evolution of EV market shares divided by region. Source: [15]

be on-board for lower power ratings or off-board for fast charging. In both cases, battery chargers are power electronics converters that are interfaced to the electric grid. Thus the increase in EV battery chargers is to follow the same trend of EV and PHEV growth. This forecast is confirmed by the trend of the last few years on the number of private and public EV battery chargers. This tendency has been described by [15] and is shown in Fig. 1.4. As the reader can notice, both private and public battery chargers have greatly increased from 2013 to 2018, passing from around half a million units in 2013 to over 5 million units in 2018.

These forecasts suggest that the following decades will see a great increase in grid connected converters. This will bring to many well-known technical and economical issues. As explained by [11], distributed generation (hereinafter called DG) will greatly affect distribution and transmission systems:

- Possible local increase of short circuit currents at the distribution system nodes. Therefore declared short circuit capability at the system nodes could be exceeded. Protection devices inside MV/LV substations could thus become insufficient and could need a new sizing.

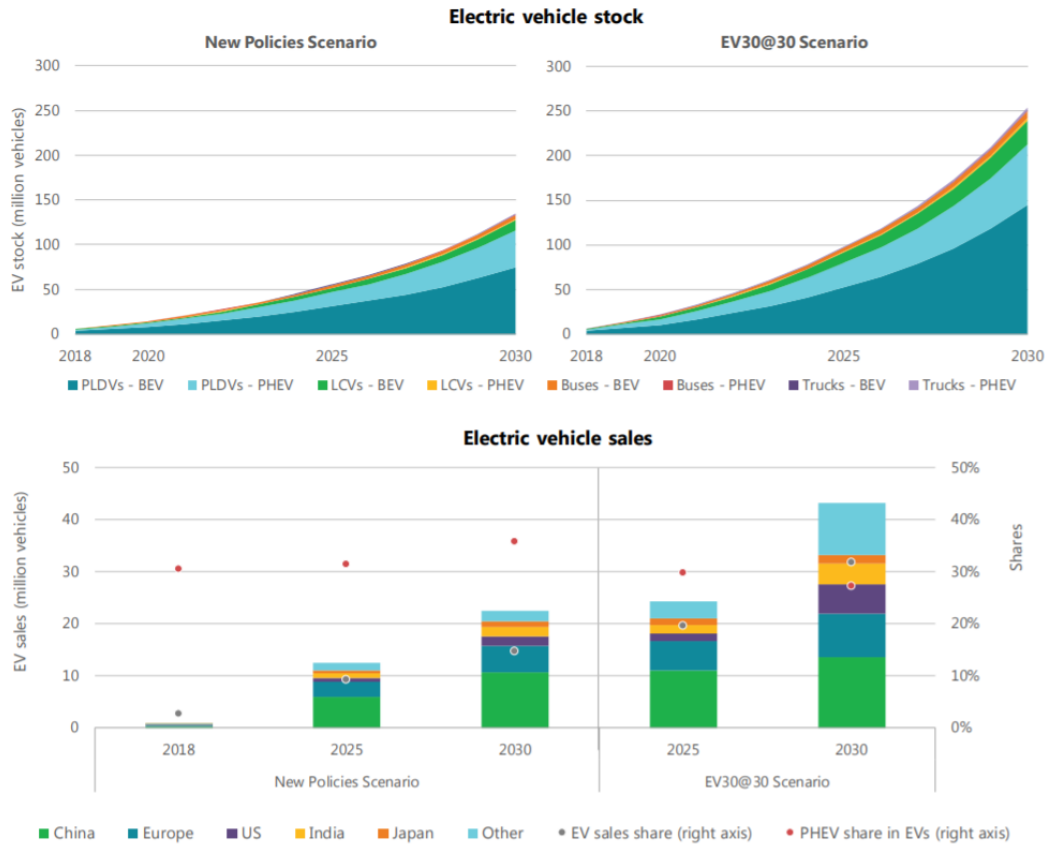


Figure 1.3: Scenarios of EV market share future trends. Source: [15]

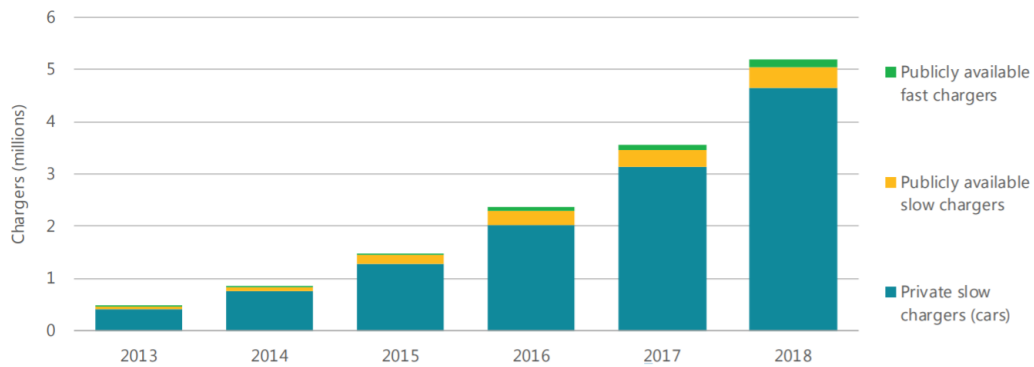


Figure 1.4: Trend of the last years on growth of the number of battery chargers. Source: [15].

- The quality of the electric supply is influenced by DG. With a high level of penetration voltage variations, harmonics and flicker events can increase.
- DG without Virtual Synchronous Compensator capabilities cannot provide transient support to the grid during frequency changes (since they have no inertial behaviour), harmonic compensation and reactive support during dips, as stated by [23].

Another issue that is less well-known and will arise is the problem of harmonic interaction between multiple grid connected converters, as explained in the following section. This work focuses on experimental characterization of converters to perform stability evaluations related to this last issue.

## 1.2 The Problem of Dynamic Interaction Between Converters

The increasing adoption of power converters due to the rapidly increasing penetration of renewable energy, distributed generation resources and EV charging stations can represent an issue because of the harmonic interaction between multiple converters. This can lead to instabilities and major harmonic resonances that cause power quality issues, even though the converters are individually stable and individually respect power quality requirements. The failure can occur in specific grid conditions, when for example many converters are connected to a weak grid. This causes unexpected current and voltage oscillations, that lead to the intervention of automatic protection equipment. It can thus be stated that the problem is not at converter level but at system level.

An example of this phenomenon already appeared in 1995, when in Zürich new generation trains equipped with high frequency switching converters failed because of harmonics [25]. After the Swiss national railway company *SBB* replaced many old locomotives with a new generation, which used high-frequency converters, on April 9, 1995 locomotives were automatically shut down by protective equipment because of excessively high harmonic currents. The incident occurred on a Sunday, thus during low traffic conditions, when only the modern locomotives were in use.

On the contrary, during normal conditions the losses of the older trains (the new ones had fewer losses because of the high switching inverter) were sufficient to damp the oscillations.

Because of this emerging issue, in [32] and [33] Italian Transmission Service Operator (TSO) Terna is starting to require dynamic models of the plants. However, the requirement is not precise. The owner of the wind plant or photovoltaic plant must communicate to Terna a dynamic model that can simulate the plant behaviour when the plant operates in the following conditions:

- electrical steady-state conditions
- electromechanical steady-state conditions, considering the grid operating in unbalanced conditions as well
- electromagnetic steady-state conditions
- steady-state conditions with the grid operating under presence of harmonics

The model can be provided in a format chosen by the user among Excel Sheets, block diagram (with explicit parameters used), transfer functions or equations. Therefore an equivalent impedance transfer function is a valid option that can be provided.

The problem of dynamic interaction must be studied before the connection of the converter to the grid, in order to anticipate possible instability issues. This analysis can be done through different methods. Since generally power electronic systems are non linear, this linear model can be considered valid only for small-signal analysis around a specific operating point. The most common methods in technical literature are:

- Eigenvalue analysis through linearized state space model. [20] [22] [36]. This method is based on the Component Connection Method (CCM), *i.e.* the system is divided into separate state-space hardware and software blocks, which are then connected through the CCM. This approach allows an easy reconfiguration of the overall model in case single blocks are varied - *e.g.* a different type of PLL is considered - and therefore has a great flexibility advantage. Another advantage is the possibility to study the effect of the various blocks

on each identified pole and zero through the utilization of participation factors. However this method only allows an analytical modelling, and requires detailed information on the hardware and control of the converter which are usually unavailable for commercial systems. It is therefore not suitable for black-box measurements.

- Frequency-domain analysis and application of the Nyquist criterion to a small-signal equivalent admittance model of the converter [29]. The goal of this method is to represent converters through a Thevenin or a Norton equivalent model, as shown in Fig. 1.5. Section 1.3 describes how the Nyquist criterion can be applied to an equivalent admittance converter model connected to the grid. This approach has many advantages:
  - The integration in system level studies is made very simple, since all converters are reduced to simple generator-admittance circuits.
  - By observing the Bode diagram of the equivalent admittances it is possible to highlight negative resistance behaviour in controllers (and thus a possible positive feedback at some frequencies).
  - It is possible to obtain the equivalent admittance through measurements. Therefore a black-box approach on commercial converters is feasible.

Because of the applicability to black-box measurements, the equivalent admittance model approach is the one considered in this work.

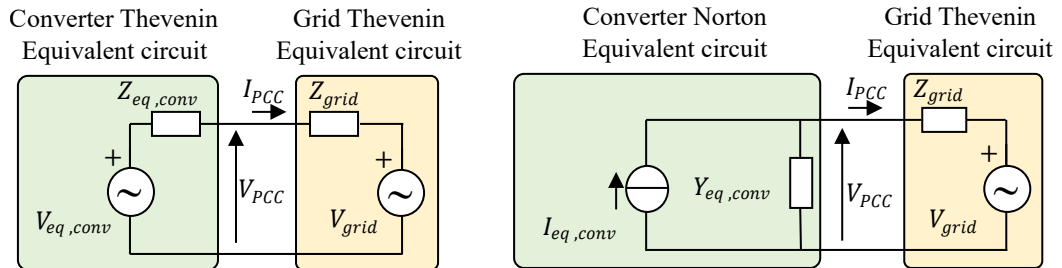


Figure 1.5: Thevenin and Norton equivalent circuit of a converter and Thevenin equivalent circuit of grid.

### 1.3 The Small-Signal Admittance Model

With the small-signal admittance model it is possible to evaluate the effects of the point of connection to the grid on the performance and stability of the inverter control. In fact, a high grid impedance could make the current control loop unstable and lead to resonance issues. Inverter instabilities due to high grid impedance are similar to source-load interaction problems found in many other power electronic systems. These are frequently studied with the impedance based stability criterion. This method does not require detailed information of the single inverters, which is often unavailable to those in charge of performing grid system stability analysis, but requires the knowledge of the equivalent impedance of every converter.

If we consider the small-signal Norton equivalent model, shown in Fig. 1.5, the Point of Common Coupling (PCC) voltage  $\mathbf{V}_{PCC}(s)$  in the  $(d, q)$  rotating reference frame can be calculated as:

$$\mathbf{V}_{PCC}(s) = [\mathbf{Z}_{grid}(s) \cdot \mathbf{I}_{eq,conv}(s) + \mathbf{V}_{grid}(s)] \cdot [\mathbf{I} + \mathbf{Z}_{grid}(s) \cdot \mathbf{Y}_{eq,conv}(s)]^{-1} \quad (1.1)$$

where

$$\mathbf{Z}_{grid}(s) = \begin{bmatrix} Z_{g,dd}(s) & Z_{g,dq}(s) \\ Z_{g,qd}(s) & Z_{g,qq}(s) \end{bmatrix} \quad \mathbf{Y}_{eq,conv}(s) = \begin{bmatrix} Y_{eq,dd}(s) & Y_{eq,dq}(s) \\ Y_{eq,qd}(s) & Y_{eq,qq}(s) \end{bmatrix} \quad (1.2)$$

and  $\mathbf{I}$  is the 2x2 identity matrix.

The off-diagonal terms of  $\mathbf{Y}_{eq,conv}(s)$  are not null, therefore there is a cross-coupling where the voltage on each axis is influenced by both the  $d$  and the  $q$ -axis current. Moreover, these mutual impedances are not equal, thus the cross-coupling effect is not symmetric.

The output current  $\mathbf{I}_{PCC}(s)$  can be calculated as:

$$\begin{aligned} \mathbf{I}_{PCC}(s) &= [\mathbf{V}_{PCC}(s) - \mathbf{V}_{grid}(s)] \cdot [\mathbf{Z}_{grid}(s)]^{-1} = \\ &= [\mathbf{I}_{eq,conv}(s) - \mathbf{Y}_{eq,conv}(s) \cdot \mathbf{V}_{grid}(s)] \cdot [\mathbf{I} + \mathbf{Z}_{grid}(s) \cdot \mathbf{Y}_{eq,conv}(s)]^{-1} \end{aligned} \quad (1.3)$$

Since  $\mathbf{V}_{grid}$  can be considered ideal and  $\mathbf{I}_{eq,conv}(s)$  is considered stable because of the correct sizing of the control loops, the stability of both  $\mathbf{V}_{PCC}(s)$  and  $\mathbf{I}_{PCC}(s)$

can be considered as dependant only on the ratio  $\mathbf{H}(s)$ :

$$\mathbf{H}(s) = [\mathbf{I} + \mathbf{Z}_{grid}(s) \cdot \mathbf{Y}_{eq,conv}(s)]^{-1} \quad (1.4)$$

The overall system of multiple converters can be represented by considering all

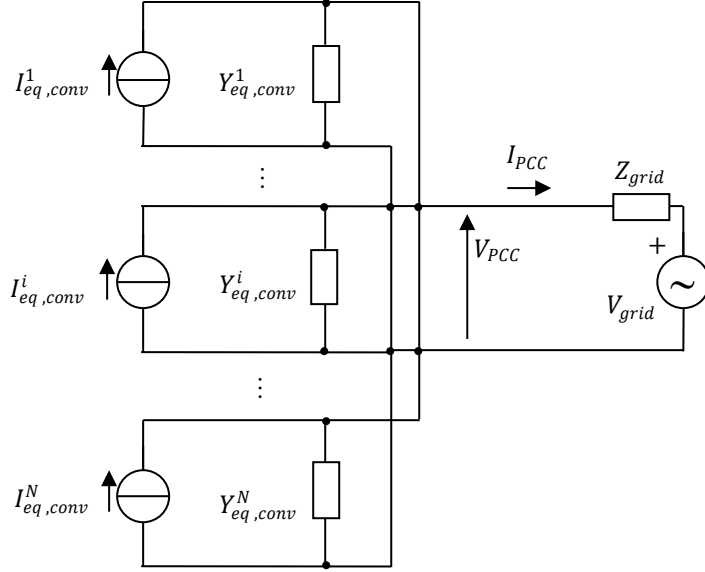
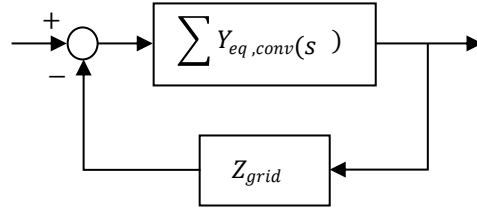


Figure 1.6: Thevenin equivalent circuit of multiple converters and Thevenin equivalent circuit of grid.

the equivalent models in parallel (Fig. 1.6). Considering multiple admittances the ratio  $\mathbf{H}(s)$  can be written as:

$$\mathbf{H}(s) = [\mathbf{I} + \mathbf{Z}_{grid}(s) \cdot \sum \mathbf{Y}_{eq,conv}(s)]^{-1} \quad (1.5)$$

This formulation is equivalent to the one of a closed loop, and can thus be represented as in Fig. 1.7 and studied as if it was a closed loop through the General Nyquist Criterion (GNC) [29]. The grid impedance and the converter admittance do not have right half plane open loop poles, since the converter is designed in order to be stable when the grid is ideal and the grid must be stable when the converter is not connected. Therefore in these conditions the GNC states that the converter-grid system is stable only if the gain  $\mathbf{Z}_{grid}(s) \cdot \sum \mathbf{Y}_{eq,conv}(s)$  does not enclose the critical point  $-1 + j0$  on the Nyquist plane.

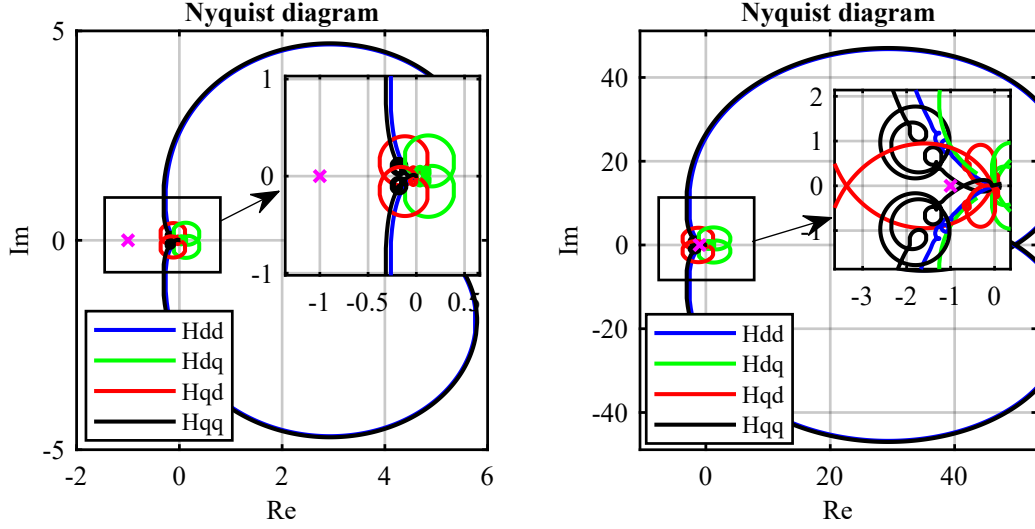
Figure 1.7: Closed loop equivalent of  $\mathbf{H}(s)$ .

### 1.3.1 Example of the GNC applied to an equivalent admittance model

The stability analysis with the equivalent admittance model and the GNC that was described in the previous section was applied to a system composed by 10 grid converters working as active rectifiers, thus in a similar situation to an EV charging station. These converters were connected to a weak grid, with  $L_g = 1.4$  mH and  $R_g = 100$  m $\Omega$ . This stability study was also applied to one single converter connected to the same grid. The equivalent admittance that was considered for each converter was the one measured in Section 3.6.2. The converter structure and control tuning were the ones described in Chapter 2.

The results of the analysis are shown in Fig. 1.8. As the reader can notice, the system with only one converter (Fig. 1.8a) is stable, while the system that considers 10 converters (Fig. 1.8b) reaches instability. This instability is therefore a system-level issue.

These results were then confirmed by a simulation on the *PLECS* power electronics simulation environment. The considered circuit is the one shown in Fig. 1.9, where the battery charger subsystems are the converter shown in Chapter 2 and not the equivalent admittance model. As the reader can notice, a switch was used in order to commute between a configuration with only one converter and one with 10 converters in parallel. If the multiple converter configuration is applied, the system becomes unstable, as the grid voltages and currents shown in Fig. 1.10 suggest.



(a) Nyquist diagram of a stable system. (b) Nyquist diagram of an unstable system.

Figure 1.8: GNC example to determine the stability of an overall system.

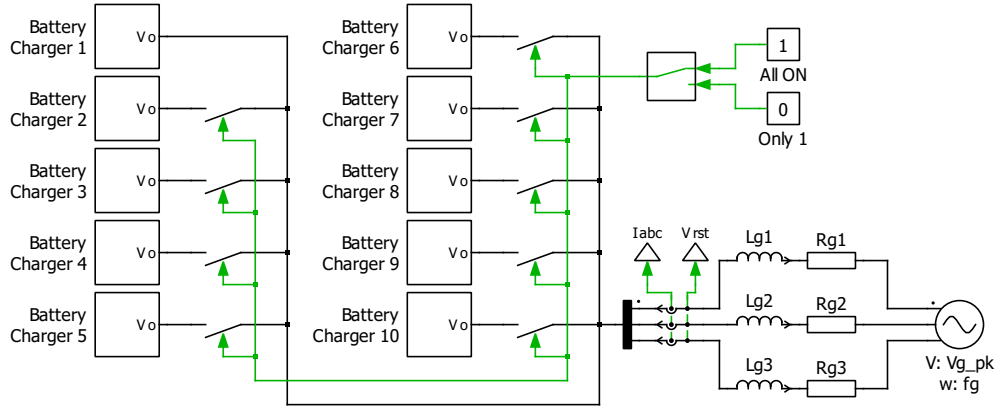
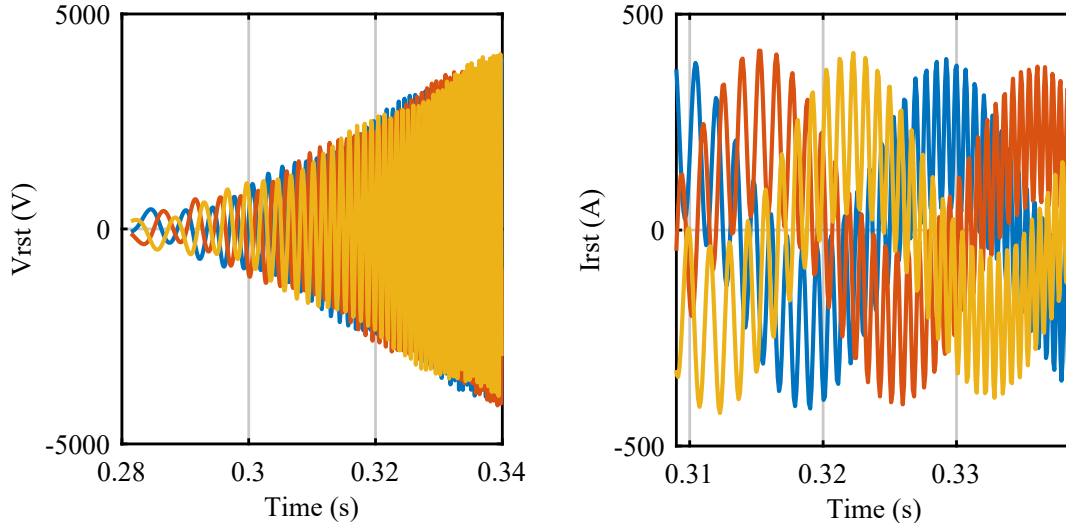


Figure 1.9: PLECS simulation with 10 converters working as active rectifiers.

## 1.4 Calculation of the Equivalent Admittance

The equivalent impedance of the converter depends on the control scheme. An analytical approach is possible and has been done by various publications, among which [37], [38] and [39].

In order to perform these calculations it is necessary to know the internal structure of the converter controller. However, for industrial secrecy reasons, the converter manufacturer may not provide detailed information on the control structure.



(a) Grid voltages in the *PLECS* simulation. (b) Grid currents in the *PLECS* simulation.

Figure 1.10: Grid voltages and currents in a *PLECS* simulation with 10 converters working as active rectifiers.

In these conditions, black-box impedance measurements techniques are required. Mainly two methods are available in technical literature in order to non-intrusively obtain the equivalent impedance of a grid converter:

- Signal Injection Technique. This is the most common method, and has been studied by [5], [12], [13], [16] and [27]. It is based on the injection of a perturbation signal at a specific frequency at the converter point of common coupling, and from system response it is possible to evaluate the converter response at that frequency. This procedure must be done for every frequency under study.
- Transient Response Measurements Technique. This method is less common than the signal injection technique, and has been studied by [35] and [34]. It is based on the perturbation of the converter with current steps, and by studying the voltage response it is possible to evaluate a transfer function of the converter impedance.

Since power converter systems are non linear, the equivalent models are valid and must be evaluated only around a precise operating point. Thus both techniques require the system to be operating during the measurements.

This thesis will focus on black-box measurements of the equivalent impedance of the converter. It is structured as follows: Chapter 2 introduces the converter structure and control which is used for the admittance measurement methods, and discusses the tuning of the control; Chapter 3 introduces the equivalent admittance measurement through the voltage injection method, and describes the implementation on a simulation environment and an experimental set-up; Chapter 4 describes the admittance measurement through the transient analysis method, and presents its implementation on a simulation environment; Chapter 5 compares the two methods and sums up the results.



## Chapter 2

# Converter Model and Control

The first step that was carried out after the review of the technical literature was the development of a simulated grid converter, in order to have the possibility to simulate the measurements and test the data processing scripts before physically testing in the laboratory.

The development involved the choice of a control structure and the development and implementation of the control scheme. Since the control was used on an already existing converter, sizing of the reactive elements was not necessary.

The values of the reactive elements in the existing converters were used for the sizing of the control loops, and are shown in Table 2.1.

### 2.1 Overall Circuit Scheme

The adopted grid converter is composed of:

- Load-side converter: a bidirectional DC/DC converter;
- Grid-side converter: a two level three phase inverter;

Fig. 2.1 shows an overview of the adopted circuit.

The considered system is bidirectional, thus it could represent both an active rectifier, *e.g.* a battery charger for electric vehicles, or a converter for generation

<b>Grid electrical data</b>		
Grid RMS phase voltage	$V_{g,RMS}$	120 V
Grid frequency	$f_g$	50 Hz
<b>Grid impedance</b>		
Grid inductance	$L_g$	270 $\mu$ H
Grid resistance	$R_g$	100 m $\Omega$
<b>Output LCL filter</b>		
Converter side inductor	$L_f$	545 $\mu$ H
Converter side inductor resistance	$R_f$	100 m $\Omega$
Grid side inductor	$L_{fg}$	120 $\mu$ H
Grid side inductor resistance	$R_{fg}$	100 m $\Omega$
Capacitor	$C_f$	22 $\mu$ F
Capacitor damping resistance	$R_{damp}$	2 $\Omega$
<b>DC-link</b>		
DC-link capacitor	$C_{DC}$	1.8 mF
DC-link set point	$V_{DC,ref}$	370 V
<b>Boost</b>		
Boost inductor	$L_{DC}$	10 mH
<b>Converter switching data</b>		
ISR update frequency	$f_{sw}$	10 kHz
ISR timing	$T_{sw}$	100 $\mu$ s
<b>Semiconductors</b>		
IGBT forward voltage	$V_{F,IGBT}$	1.2 V
IGBT forward resistance	$R_{on,IGBT}$	10 m $\Omega$
Diode forward voltage	$V_{F,d}$	1 V
Diode forward resistance	$R_{on,d}$	1 m $\Omega$
<b>Maximum ratings</b>		
Maximum output power	$S_{AC,max}$	15 kVA
<b>Load data</b>		
Load DC voltage	$V_{load}$	200 V

Table 2.1: Converter values.

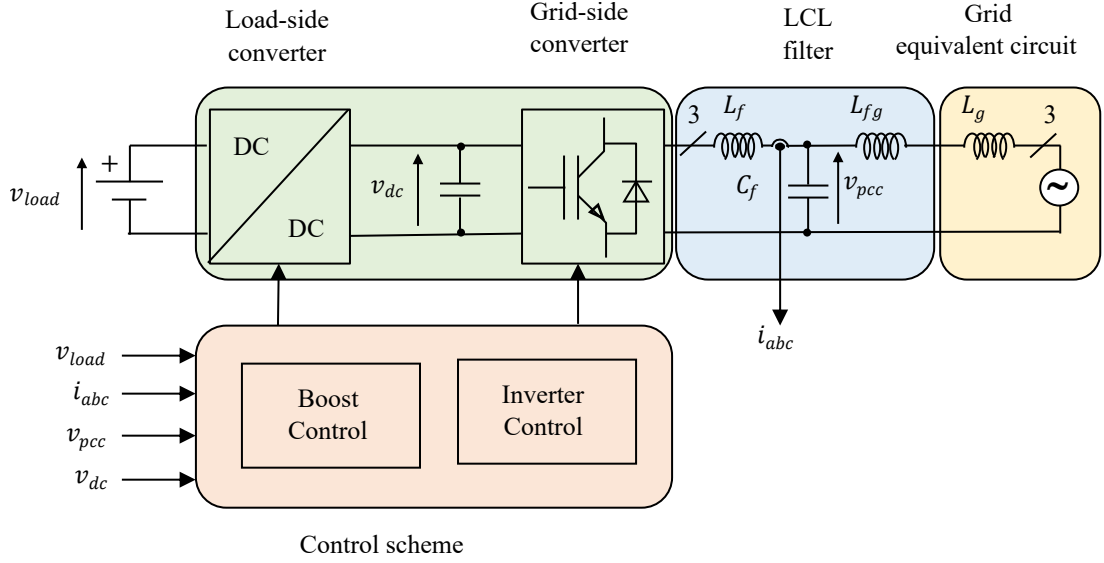


Figure 2.1: Diagram of the considered system.

purposes, e.g. a solar inverter. In fact, the DC/DC converter is controlled as a current generator that imposes either a load operation - a battery charger, for instance - or a generation operation, *e.g.* for a photovoltaic generation with MPPT<sup>1</sup>. In the first case  $v_{load}$  models a variable load, in the second case  $v_{load}$  models a variable source. In both cases  $v_{load}$  is a variable voltage, with a value that must be below the DC-link voltage set point in order to permit a correct operation.

The step up converter is a current controlled boost rectifier which regulates the current on the *load* side. This produces a perturbation on the DC-link capacitor, whose voltage is kept constant by the three-phase inverter. The power regulation is thus done on the *load* side, and the inverter follows the requested power indirectly by controlling the voltage on the DC-link capacitor.

In order to meet the power quality specifications requested by electrical energy distributors, an LCL filter is added to the output. This filter reduces greatly the current and voltage switching harmonics in the point of common coupling.

The grid is represented through its Thevenin equivalent. The equivalent impedance can be modified to emulate different points of connection to the grid.

<sup>1</sup>Maximum Power Point Tracker. This is a technique used in photovoltaic systems to maximize power production.

## 2.2 Overview of the Inverter Control Scheme

Most of the controls encountered in the review of the technical literature are similar. The most common control is a cascaded control with an outer DC-link voltage control and an inner grid current control. A PLL (phased-locked loop) is in charge of the synchronization with the grid voltage. Fig. 2.2 provides an overview of the adopted control scheme. As the reader can notice, the voltage control loop keeps

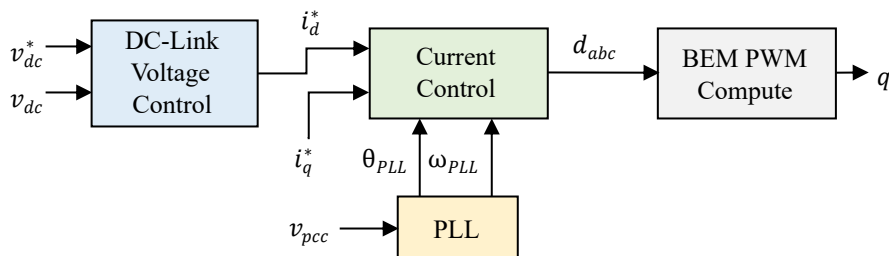


Figure 2.2: Overview of adopted control scheme.

the voltage on the DC-Link capacitor  $v_{dc}$  constant and equal to a reference  $v_{dc}^*$ . This loop calculates the necessary output current and sends it as a reference for the current control on the  $d$ -axis.

The current control is in the rotating reference frame  $(d, q)$ , where the  $d$ -axis is coincident with the voltage vector angle. The representation of the relation of the voltage vector with the reference frame is shown in Fig. 2.3. With this reference frame rotation it is possible to achieve a null steady state average error. The current control accepts a reference on the  $d$ -axis, in order to vary the absorbed or injected active power towards the grid, and a reference on the  $q$ -axis, in order to vary the reactive power.

The control calculates the necessary duty cycles to reach the references, and with these the inverter control functions  $q$  are obtained by considering a Balanced Envelope Modulation (BEM).

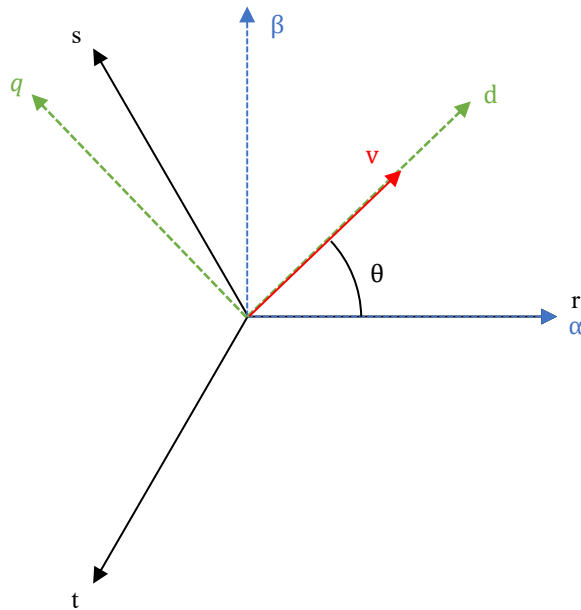


Figure 2.3: Position of the voltage vector with respect to the different stationary and rotating reference frames.

## 2.2.1 Grid Synchronization Unit

### The Need for a Grid Synchronization Unit

Synchronization with the grid voltage phase angle  $\theta_{v,PCC}$  is a matter of great importance in the control of grid connected converters. It is thus necessary to determine in an accurate and precise way  $\theta_{v,PCC}$  in order to enable the possibility of an independent regulation of the active and reactive power flow between the converter load side and the grid. The grid synchronization unit is responsible for a correct synchronization.

The quality of grid synchronization is a key factor for a proper operation of the control, since an error in the estimation will lead to an error in the generated output voltage, and a consequent error in the power flow or output current with respect to the chosen reference. For this reason the grid synchronization unit must be well designed and tested under different grid conditions, in order to ensure a correct operation even under a certain amount of grid voltage distortion.

Many possible events can cause grid voltage distortion. Examples are disturbances and resonances due to harmonic currents flowing through the power lines,

frequent connection and disconnection of loads, faults due to adverse weather conditions like lightnings and triggering of load-break switches. According to IEEE 1159 [14], these events can cause transients, long and short duration variations, unbalances, distortions, fluctuations and frequency variations. Because of these reasons grid variables such as voltage amplitude and frequency cannot be considered as constant magnitudes in the control. On the contrary, they must be continuously monitored.

Moreover, it must be pointed out that when the power involved by a converter is significant with respect to the grid rated power at the point of connection, grid voltage and frequency can be affected by the converter operation.

The knowledge of grid voltage frequency, which is obtained by deriving the phase angle, is also compulsory in order to determine whether the converter must remain connected to the grid. In fact, converters can actively participate in the support of the grid voltage and frequency, especially when high power ratings are considered. Grid stability and safety is thus related to the converter operation. For this reason national and international grid codes have been published in the last few years in order to establish the behaviour of power converters both in steady state and in transient conditions. The connection of users in Italy is regulated by three standards: *CEI 0-21* for active users connected to low voltages in the distribution network, *CEI 0-16* for active users connected to medium and high voltages in the distribution network and *Allegato A70 al Codice di Rete* [31] for distributed generation. These standards describe the conditions for the disconnections of users. This can depend on the variation of grid voltage and frequency. As for the variation of the grid voltage, predefined *Fault Ride Through capability* curves are defined, which correlate the variation of grid voltage with the duration of the variation in order to avoid an uncontrolled loss of generation concurrently with grid faults. As for the variation of the grid frequency, two conditions are defined for the disconnection in [31]. The first one depends on the magnitude, and states that users must be able to remain connected for grid frequency values contained in the range of 47.5 Hz and 51.5 Hz. The second condition for disconnection is defined on the Rate of Change of Frequency, known as ROCOF.

The problem of the disconnection of the converter according to grid conditions

was not implemented in the control since it is not the main objective of this work, and will not be further discussed.

### The $(d, q)$ Frame Based Phase-Locked Loop

Many methods are available in order to obtain the grid voltage phase angle  $\theta_{v,PCC}$ , as described in [30]. The most common of these, and one of the most robust as well, is the Phase-Locked Loop (hereinafter referred to as PLL).

Many PLL algorithms are available in the literature. They all have in common the goal of producing an internal reference signal for use in the control loops, calculated with a particular grid variable which usually is the fundamental component of the grid voltage. The adopted control in this work is based on the rotating reference frame transformation of a three phase voltage.

To understand the functioning of the  $(d, q)$ -based PLL, let's consider an ideal three phase voltage:

$$V_{rst} = \begin{bmatrix} \hat{V} \cdot \sin(\omega_I \cdot t) \\ \hat{V} \cdot \sin(\omega_I \cdot t + \frac{2\pi}{3}) \\ \hat{V} \cdot \sin(\omega_I \cdot t - \frac{2\pi}{3}) \end{bmatrix} \quad (2.1)$$

where  $\omega_I$  is the fundamental electrical pulsation defined as:

$$\omega_I = 2\pi \cdot f_I \quad (2.2)$$

and  $f_I$  is the voltage fundamental frequency.

Since the three phase voltages are ideal, we can simplify it by reducing it to only two phases by using the amplitude invariant Clarke transformation  $\mathbf{A}$ . This is defined in Appendix B.

The transformation results in:

$$V_{\alpha\beta 0} = \mathbf{A} \cdot V_{rst} = \begin{bmatrix} V_\alpha \\ V_\beta \\ V_0 \end{bmatrix} = \begin{bmatrix} \hat{V} \cdot \sin(\omega_I \cdot t) \\ \hat{V} \cdot \cos(\omega_I \cdot t) \\ 0 \end{bmatrix} \quad (2.3)$$

Since the considered system has only three wires, there cannot be homopolar components. We can thus consider only the  $(\alpha, \beta)$  components and pass to a two phase system  $V_{\alpha, \beta}$ .

Let's call  $\theta = \omega_I \cdot t$ . Then we can write  $V_{\alpha, \beta}$  as

$$\begin{bmatrix} V_\alpha \\ V_\beta \end{bmatrix} = \begin{bmatrix} \hat{V} \cdot \sin(\theta) \\ \hat{V} \cdot \cos(\theta) \end{bmatrix} \quad (2.4)$$

The next step is to move to the rotating reference frame  $(d, q)$ , where the  $V_{\alpha\beta}$  vector is rotated by an angle  $\hat{\theta}$ . The rotation is done using the rotation transformation  $\mathbf{R}(\theta)$ , defined in Appendix B.

This leads to the result:

$$\hat{\mathbf{V}}_{dq} = \mathbf{R}(\hat{\theta}) \cdot \mathbf{V}_{\alpha\beta} = \begin{bmatrix} \hat{V} \cdot \sin(\theta - \hat{\theta}) \\ \hat{V} \cdot \cos(\theta - \hat{\theta}) \end{bmatrix} \quad (2.5)$$

If the difference in the angles  $\theta$  and  $\hat{\theta}$  in (2.5) is small then  $\hat{\mathbf{V}}_{dq}$  can be approximated to:

$$\hat{\mathbf{V}}_{dq} = \begin{bmatrix} \hat{V}_d \\ \hat{V}_q \end{bmatrix} \simeq \begin{bmatrix} \hat{V} \cdot 1 \\ \hat{V} \cdot (\theta - \hat{\theta}) \end{bmatrix} \quad (2.6)$$

It can be noted from (2.6) that the more  $\theta$  and  $\hat{\theta}$  are similar, the more  $V_d$  is equal to the amplitude of the voltage vector and  $V_q$  is proportional to the error between the two angles  $\theta$  and  $\hat{\theta}$ .

The  $(d, q)$  frame based Phase-Locked Loop exploits the result in (2.6) by using  $V_q$  as an error signal for a position control loop. Fig. 2.4 shows the adopted block diagram.

The error signal  $V_q$  is sent to a Proportional-Integral controller (hereinafter referred to as PI controller), whose output is the electrical pulsation  $\omega_{PLL}$ . In order to obtain the angle position  $\theta_{PLL}$ , the pulsation is integrated.

In fact, if the observed position  $\hat{\theta}$  (hereinafter referred to as  $\theta_{PLL}$ ) is lower than  $\theta$ , the PLL increases the observed pulsation  $\omega_{PLL}$  in order to increase  $\theta_{PLL}$  faster, while if it is higher  $\omega_{PLL}$  will be reduced in order to increase  $\theta_{PLL}$  more slowly. At

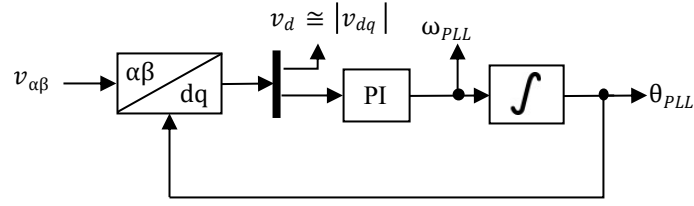


Figure 2.4: Block diagram of the Phase-Locked Loop.

steady state  $\theta_{PLL}$  will thus follow  $\theta$  according to the PLL dynamics, and the average value of  $\omega_{PLL}$  will be equal to  $\omega_I$ , *i.e.* the electrical pulsation of the fundamental voltage component.

In order to analyse the dynamics of the PLL, the open and closed loop transfer functions of the PLL must be studied. This can be done considering the Laplace equivalent of Fig. 2.4, which is shown in Fig. 2.5. At first the open loop transfer function is considered:

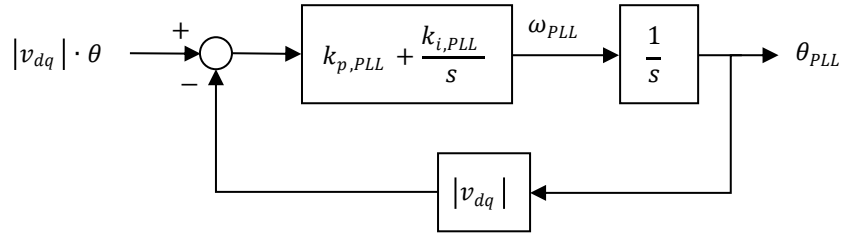


Figure 2.5: Block diagram of the Phase-Locked Loop in the Laplace domain.

$$G_{OL,PLL} = H_{PI} \cdot \frac{|V_{dq}|}{s} = k_{p,PLL} \cdot |V_{dq}| \cdot \frac{s + \omega_{z,PLL}}{s^2} \quad (2.7)$$

where

$$H_{PI} = k_{p,PLL} + \frac{k_{i,PLL}}{s} = k_{p,PLL} \cdot \frac{s + \omega_{z,PLL}}{s} \quad (2.8)$$

and

$$\omega_{z,PLL} = \frac{k_{i,PLL}}{k_{p,PLL}} \quad (2.9)$$

The closed loop transfer function can be written as:

$$G_{CL,PLL} = k_{p,PLL} \cdot |V_{dq}| \cdot \frac{s + \omega_{z,PLL}}{s^2 + k_{p,PLL} \cdot |V_{dq}| \cdot s + k_{p,PLL} \cdot |V_{dq}| \cdot \omega_{z,PLL}} \quad (2.10)$$

### 2.2.2 Tuning of the PLL PI Controller

To determine the bandwidth, two approaches are possible. The most common tuning method studies the open loop transfer function. However, since the closed loop transfer function is relatively simple, this can be directly studied for the tuning of the controller. During the development of this work, the open loop transfer function method was initially used. Then the closed loop transfer function method was used. Since the latter was then implemented in the experimental set-up, in the following lines the explanation of the tuning with the closed loop transfer function will be shown. However the tuning with the open loop transfer function is described in Appendix A.

In order to tune correctly the PI controller parameters through the closed loop transfer function, (2.10) is considered. Since it is a second order transfer function, the denominator can be written in the form:

$$s^2 + 2 \cdot \zeta \cdot \omega_0 \cdot s + \omega_0^2 \quad (2.11)$$

where  $\zeta$  is the damping factor and  $\omega_0$  is the resonance frequency. By equating (2.10) with (2.11) the controller gains are obtained:

$$k_{p,PLL} = \frac{2 \cdot \zeta \cdot \omega_0}{|V_{dq}|} \quad (2.12)$$

$$\omega_{z,PLL} = \frac{\omega_0^2}{k_{p,PLL} \cdot |V_{dq}|} = \frac{\omega_0}{2 \cdot \zeta} \quad (2.13)$$

$$k_{i,PLL} = \omega_{z,PLL} \cdot k_{p,PLL} = \frac{\omega_0^2}{|V_{dq}|} \quad (2.14)$$

The ratio between the resonance frequency  $\omega_0$  and the PI zero  $\omega_{z,PLL}$  is:

$$\frac{\omega_0}{\omega_{z,PLL}} = \frac{1}{2 \cdot \zeta} \quad (2.15)$$

The resonance frequency can be considered equal to the crossover frequency  $\omega_{bw,PLL}$ . From (2.13) the reader can notice that in order to have a PI zero that is lower than the crossover frequency the minimum damping factor  $\zeta$  is 0.5. However, in order to not have overshoots near the resonance frequency, in this work a critical damping was chosen, *i.e.*  $\zeta = 1/\sqrt{2}$ . This leads to a ratio between the crossover

frequency and the PI zero of  $\sqrt{2}/2$ . If one would want this ratio to be 10, as done for the open loop transfer function method in Appendix A, a damping factor of 5 would be necessary, which is very high and not necessary. Therefore the controller gains obtained with this method provide better dynamic performances than the ones calculated in Appendix A. The results of the tuning obtained by using the equations above are shown in Table 2.2.

Parameter	Value
$f_{bw,PLL}$	5 Hz
$\omega_{bw,PLL}$	31.4159 rad/s
$f_{z,PLL}$	3.5355 Hz
$\omega_{z,PLL}$	22.2144 rad/s
$k_{p,PLL}$	0.2618 1/(V·s)
$k_{i,PLL}$	5.8157 rad/(V·s <sup>2</sup> )
$\zeta$	0.7071

Table 2.2: PLL set-up values.

A Bode diagram of the PLL open and closed loop transfer functions tuned with parameters in Table 2.2 is shown in Fig. 2.6.

In order to validate the performance of the system, a simulation was performed on the power electronics simulation software *PLECS* with the PI controller calibrated as in Table 2.2. The input voltage was an ideal three phase voltage, with no unbalancing or harmonics different from the fundamental. Results are shown in Fig. 2.7.

### Normalized $(d,q)$ Frame Based Phase-Locked Loop

The reader can notice that the PLL adopted in Section 2.2.1 has a bandwidth that is dependant on the amplitude of the voltage vector. In general, in a simple  $(d,q)$  based PLL, dynamics depend on grid voltage amplitude. This can be an issue when voltage transients are involved (*e.g.* during short circuit events in the grid).

It is therefore necessary to make the PLL insensible to the amplitude. In order to achieve this goal, it is possible to normalize voltages in the  $(\alpha, \beta)$  frame over the peak amplitude before transforming them in the  $(d,q)$  frame. If this operation is

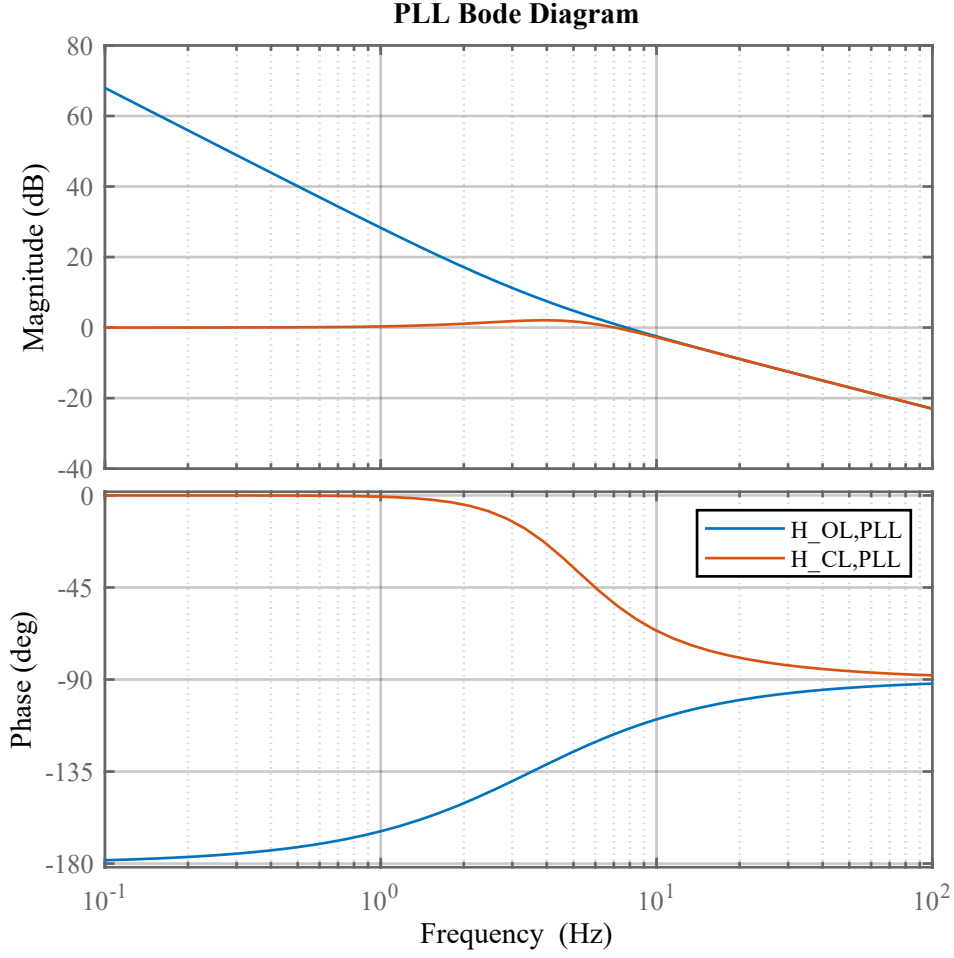


Figure 2.6: Bode diagram of the PLL open and closed loop transfer functions.

considered, the tuning equations calculated in Subsection 2.2.2 need to be modified by considering  $|V_{dq}|$  as unitary. Therefore:

$$k_{p,PLL} = 2 \cdot \zeta \cdot \omega_{bw,PLL} \quad (2.16)$$

$$k_{i,PLL} = \omega_{z,PLL} \cdot k_{p,PLL} = \omega_{bw,PLL}^2 \quad (2.17)$$

where a critical damping is considered.

The results of the tuning obtained by using the equations above are shown in Table 2.3.

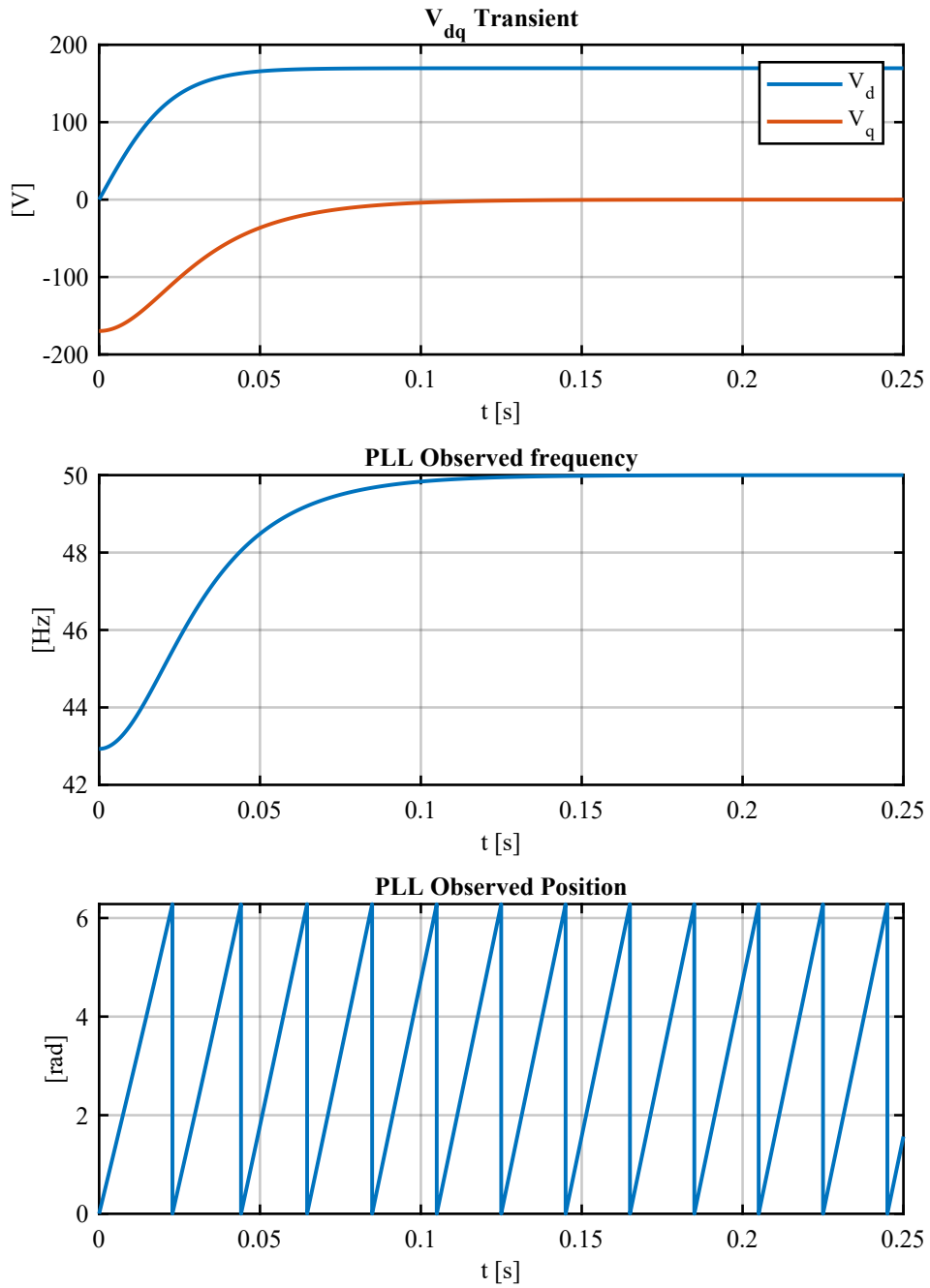


Figure 2.7: *PLECS* simulation of a PLL calibrated as in Table 2.2 while fed by an ideal voltage.

Parameter	Value
$f_{bw,PLL}$	5 Hz
$\omega_{bw,PLL}$	31.4159 rad/s
$f_{z,PLL}$	3.5355 Hz
$\omega_{z,PLL}$	22.2144 rad/s
$k_{p,PLL}$	44.4288 1/(V·s)
$k_{i,PLL}$	986.96 rad/(V·s <sup>2</sup> )
$\zeta$	0.7071

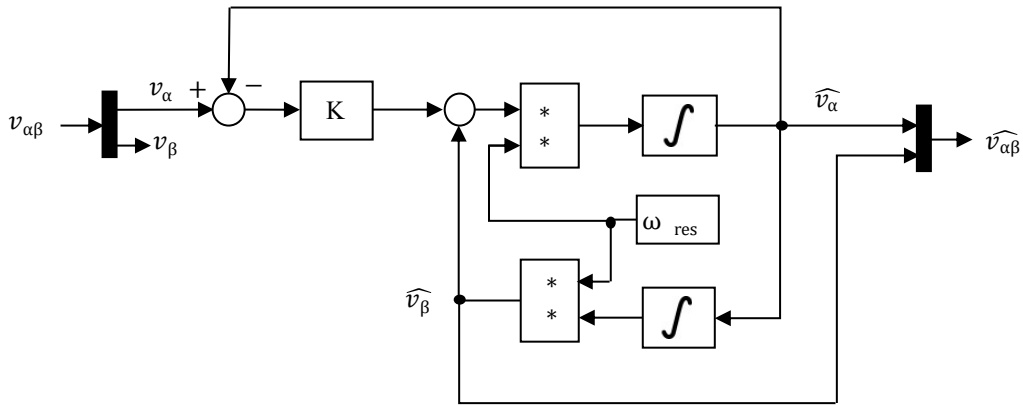
Table 2.3: PLL set-up values with voltage normalization.

### Secondary Order Generalized Integrator (SOGI)

The normalization of voltages over their amplitudes described in Section 2.2.2 solves the PLL output disturbances generated by voltage transients, but not disturbances generated by voltage harmonics and unbalances.

The only harmonic which has an energetic value is the fundamental one, and thus the PLL should observe only this one. It is necessary to filter out all harmonics that are superior to the fundamental one.

This process can be done with a resonant filter centred on grid frequency. The solution adopted for this project is a Second Order Generalized Integrator (SOGI). Fig. 2.8 shows its structure.


 Figure 2.8: Structure of a *SOGI* resonant filter.

The only voltage component that is considered is the one on the  $\alpha$  axis  $v_\alpha$ . The

gain  $k$  is the damping factor.

As for  $v_\alpha$ , the open loop transfer function of the system is:

$$H_{OL} = 2 \cdot k \cdot \frac{\omega_{res} \cdot s}{s^2 + \omega_{res}^2} \quad (2.18)$$

While the closed loop transfer function is:

$$H_{CL} = \frac{\hat{v}_\alpha}{v_\alpha} = \frac{2 \cdot k \cdot \omega_{res} \cdot s}{s^2 + 2 \cdot k \cdot \omega_{res} \cdot s + \omega_{res}^2} \quad (2.19)$$

The damping factor  $k$  has an effect on the selectivity of the input frequency. This can be seen by studying the frequency interval where the open loop transfer function has an amplifying effect.

$$|H_{OL}| = \frac{|2 \cdot k \cdot \omega_{res} \cdot j \cdot \omega|}{|-\omega^2 + \omega_{res}^2|} = 1 \quad (2.20)$$

The numerator is always positive, while for the denominator two cases have to be considered.

1. As for the first case:

$$\omega_{res}^2 - \omega^2 \geq 0 \quad (2.21)$$

$$0 \leq \omega \leq \omega_{res} \quad (2.22)$$

In this frequency range we can consider:

$$\frac{2 \cdot k \cdot \omega_{res} \cdot j \cdot \omega}{\omega_{res}^2 - \omega^2} = 1 \quad (2.23)$$

This can be rewritten as:

$$\omega^2 + 2 \cdot k \cdot \omega - \omega_{res}^2 = 0; \quad (2.24)$$

The solutions of the second order polynomial are:

$$\omega_{1,2} = -k \pm \sqrt{k^2 + \omega_{res}^2} \quad (2.25)$$

Since only positive frequencies are acceptable because of the existence conditions in (2.22), the only solution of the polynomial is:

$$\omega_1 = -k + \sqrt{k^2 + \omega_{res}^2} \quad (2.26)$$

2. As for the second case, valid where  $\omega > \omega_{res}$ , the function becomes:

$$\frac{2 \cdot k \cdot \omega_{res} \cdot j \cdot \omega}{\omega^2 - \omega_{res}^2} = 1 \quad (2.27)$$

Which becomes:

$$\omega^2 - 2 \cdot k \cdot \omega - \omega_{res}^2 = 0; \quad (2.28)$$

The solutions of the polynomial are:

$$\omega_{1,2} = k \pm \sqrt{k^2 + \omega_{res}^2} \quad (2.29)$$

Because of the existence conditions the only acceptable solution is:

$$\omega_2 = k + \sqrt{k^2 + \omega_{res}^2} \quad (2.30)$$

The frequency range in which the harmonics are not attenuated can be therefore calculated in rad/s by calculating the difference between  $\omega_2$  and  $\omega_1$ :

$$\Delta\omega = \omega_2 - \omega_1 = 2 \cdot k \quad (2.31)$$

In Hz:

$$\Delta f = \frac{k}{\pi} \quad (2.32)$$

The reader must consider that the aim of the *SOGI* is not to make the completely PLL insensible to the grid functioning, but only to reject unwanted harmonics. Moreover, the set point of grid frequency is not fixed and could be slightly different from the considered one during the design stage. [31] describes when the converter should remain connected to the grid even though there is a variation from *50 Hz* on the grid frequency. Therefore a damping factor between 50 and 100 is a good compromise. For this work a *k* of 50 was used. Thus converter harmonics are damped when their frequencies are out of the  $50 \pm 8$  Hz range.

### 2.2.3 Converter Current Control

The current control is implemented in the  $(d, q)$  rotating frame, synchronous with the grid voltage vector. This has the following advantages:

- It is possible to cancel the steady state error on the reference current through a proportional-integral controller. In fact in any control system it can be demonstrated that the steady state error depends on the polynomial order of the desired response and on the number of poles in zero in the open loop transfer function. To gain a null steady state error, the number of poles in zero must be greater than the order of the input. For a constant reference, thus with a zero order, one pole in zero is sufficient. However, it must be noted that with a sinusoidal reference a null steady state error can still be obtained by using a *P-Res* resonant controller, tuned on the frequency of the sinusoidal reference.
- The computational burden is reduced, since only two regulators, instead of three are necessary. This was useful in the past, when the implementation was done on low performance microcontrollers. Nowadays this advantage is less crucial but still useful if the control designer wants to implement a great number of operations on the control, *e.g.* for an on-line commissioning.
- According to the  $p - q$  Instantaneous Power Theory [3], the active power  $p$  and the reactive power  $q$  can be written as:

$$\begin{bmatrix} p \\ q \end{bmatrix} = \frac{3}{2} \cdot \begin{bmatrix} v_d & v_q \\ -v_q & v_d \end{bmatrix} \cdot \begin{bmatrix} i_d \\ i_q \end{bmatrix} \quad (2.33)$$

Since through the PLL the  $(\alpha, \beta)$  voltages are rotated so that all the voltage amplitude is on the  $d$ -axis and  $v_q$  is null, the current on the  $d$ -axis is proportional to the active power, and the one on the  $q$ -axis is proportional to the reactive power.

$$p = \frac{3}{2} \cdot v_d \cdot i_d \quad (2.34)$$

$$q = \frac{3}{2} \cdot v_d \cdot i_q \quad (2.35)$$

With this simple formulation, the possibility of power control is made easier.

The reference on the  $d$ -axis comes from the voltage loop, so it is not possible to perform an active power control directly from this loop. On the contrary, it is

possible to set the  $q$ -axis reference. This allows to vary the absorbed or injected reactive power to comply to the requests of the grid codes.

### Converter Delay Transfer Function

The current loop was designed in order to obtain the highest possible bandwidth while maintaining stability. In order to do so, the converter delay transfer function has to be considered:

$$H_{conv}(s) = e^{-s \cdot \tau} \quad (2.36)$$

Where  $\tau_{conv}$  is the converter delay. To estimate it, a digital control with single sampling and single refresh per ISR<sup>2</sup> was considered. Since variables are sampled at a generic instant  $t_k$  and the output values of the ISR are updated to the modulator value after a switching period  $T_{sw}$ , at the time instant  $t_{k+1} = t_k + T_{sw}$ , the new output values are the correction for the physical system at the previous instant  $t_k$ . Thus the sampling and ISR operation introduce a sampling delay equal to  $T_{sw}$ . Then the modulator is compared with the triangular carrier, and the result, *i.e.* the inverter leg control signal, varies after a period of time between 0 and  $T_{sw}$ . This is called implementation delay, and an average value of it is half of a switching period. The total delay introduced by the converter is:

$$\tau_{conv} = T_{sw} + \frac{1}{2} \cdot T_{sw} = \frac{3}{2} \cdot T_{sw} \quad (2.37)$$

Often a low pass filter approximation of (2.36) is used, in order to simplify the exponential into a first order linear transfer function:

$$H_{conv}(s) \simeq \frac{1}{1 + s \cdot \tau_{conv}} \quad (2.38)$$

This is equivalent to a Padè approximant of order [0,1]. The pole of the simplified converter delay transfer function is:

$$p_{conv} = \frac{1}{\tau_{conv}} = \frac{2}{3} \cdot \frac{1}{T_{sw}} = \frac{2}{3} \cdot f_{sw} \quad (2.39)$$

---

<sup>2</sup>Interrupt Service Routine, *i.e.* the routine that is called by the microcontroller every switching period. All the control loops are written in this routine.

More precise approximations can be obtained by using Padè approximants of higher order. Fig. 2.9 compares the phase of the transfer functions of different approximations with respect to (2.36). The considered orders are [0,1], [1,1], [2,2], [3,3]:

$$H_{conv,[1,1]} = \frac{1 - s \cdot \frac{\tau_{conv}}{2}}{1 + s \cdot \frac{\tau_{conv}}{2}} \quad (2.40)$$

$$H_{conv,[2,2]} = \frac{1 - s \cdot \frac{\tau_{conv}}{2} + s^2 \cdot \frac{\tau_{conv}^2}{12}}{1 + s \cdot \frac{\tau_{conv}}{2} + s^2 \cdot \frac{\tau_{conv}^2}{12}} \quad (2.41)$$

$$H_{conv,[3,3]} = \frac{1 - s \cdot \frac{\tau_{conv}}{2} + s^2 \cdot \frac{\tau_{conv}^2}{10} - s^3 \cdot \frac{\tau_{conv}^3}{120}}{1 + s \cdot \frac{\tau_{conv}}{2} + s^2 \cdot \frac{\tau_{conv}^2}{10} + s^3 \cdot \frac{\tau_{conv}^3}{120}} \quad (2.42)$$

The reader can notice how the error greatly decreases as the order of the approximation increases. The [0,1] case shows already a satisfactory result, while [3,3] is an almost exact approximation. Table 2.4 shows the phase error between (2.36)

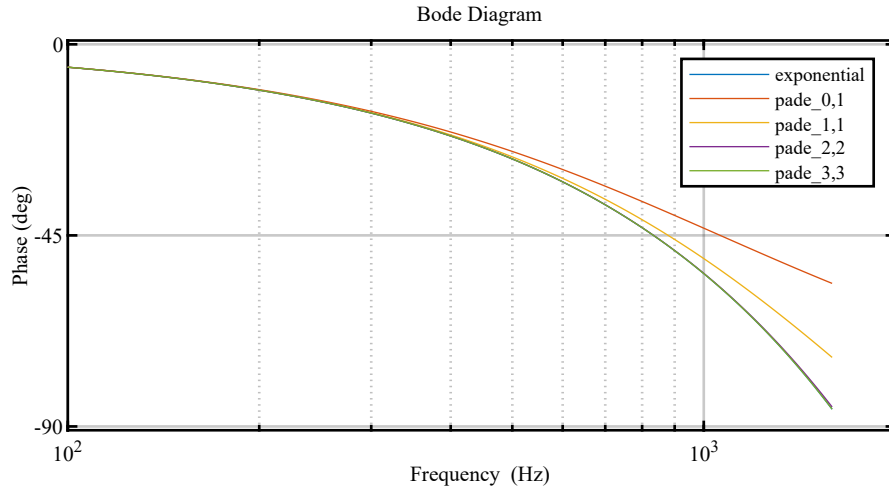


Figure 2.9: Comparison of various Padè approximations.

and the approximations at the frequency of 1000 Hz.

### Current Loop Tuning

The best dynamics while maintaining stability are obtained by setting the gain of the current loop in order to achieve a bandwidth frequency that is approximately equal to the pole of the [0,1] order Padè approximant of the converter delay transfer

Padè Order	Approximation Error
[0,1]	10.696193°
[1,1]	3.536726°
[2,2]	0.056057°
[3,3]	0.000363°

Table 2.4: Errors of various Padè approximations with respect to the non approximated transfer function of the converter delay.

function:

$$\omega_{bw,i} = p_{conv} = \frac{2}{3} \cdot f_{sw} \quad (2.43)$$

In  $Hz$  this can be written as:

$$f_{bw,i} = \frac{\omega_{bw,i}}{2 \cdot \pi} = \frac{2}{3} \cdot \frac{1}{2 \cdot \pi} \cdot f_{sw} = \frac{f_{sw}}{3 \cdot \pi} \simeq \frac{f_{sw}}{10} \quad (2.44)$$

Therefore the regulators were sized so that the bandwidth frequency was positioned a decade before the PWM switching frequency.

The block representation of the current loop in the Laplace domain is shown in Fig. 2.10. The current flowing through the inverter side inductor is controlled. The voltage across the filter capacitors  $C_f$  is considered constant. The inductor equivalent series resistance is neglected. Therefore, the plant is equivalent to a single inductor  $L_f$ .

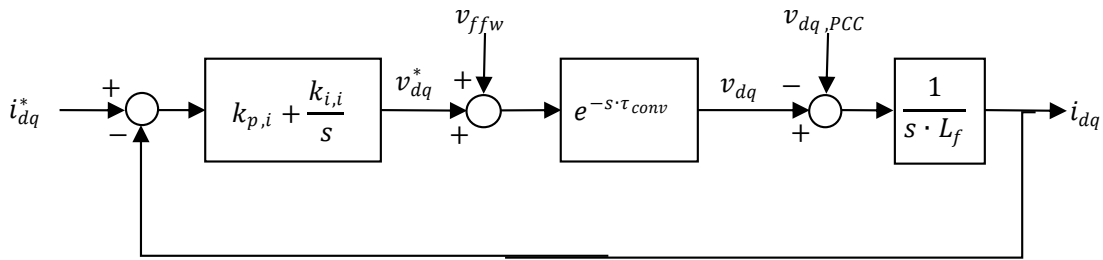


Figure 2.10: Block representation of the current loop in the Laplace domain.

The open loop transfer function is:

$$H_{OL,i}(s) = \left( k_{p,i} + \frac{k_{i,i}}{s} \right) \cdot e^{-s \cdot \tau_{conv}} \cdot \frac{1}{s \cdot L_f} \quad (2.45)$$

To study the crossover frequency of (2.45), an approximation of the open loop transfer function at high frequencies can be considered by neglecting the converter delay:

$$H_{OL,i}(s) \Big|_{hf} \simeq \frac{k_{p,i}}{s \cdot L_f} \quad (2.46)$$

At the crossover frequency the open loop gain is unitary:

$$|H_{OL,i}(\omega_{bw,i})| = 1 \simeq \frac{k_{p,i}}{\omega_{bw,i} \cdot L_f} \quad (2.47)$$

The proportional gain of the controller can therefore be calculated as:

$$k_{p,i} = \omega_{bw,i} \cdot L_f \quad (2.48)$$

As for the zero of the PI controller  $\omega_{z,i}$ , it was placed a decade before the bandwidth frequency.

$$\omega_{z,i} = \frac{\omega_{bw,i}}{10} \quad (2.49)$$

The integral gain of the controller is calculated as:

$$\omega_{z,i} = \frac{k_{i,i}}{k_{p,i}} \quad (2.50)$$

$$k_{i,i} = k_{p,i} \cdot \omega_{z,i} \quad (2.51)$$

Results of tuning using the described equations are shown in Table 2.5.

Parameter	Value
$f_{bw,i}$	1000 Hz
$\omega_{bw,i}$	6283.19 rad/s
$f_{z,i}$	100 Hz
$\omega_{z,i}$	628.32 rad/s
$k_{p,i}$	3.424 $\Omega$
$k_{i,i}$	2151.574 $\Omega \cdot \text{rad/s}$
Phase margin	30°

Table 2.5: Current loop set-up values.

Using the values of Table 2.5 in (2.45) the Bode diagrams of the open and closed loop transfer function can be calculated, as shown in Fig. 2.11. In order to obtain these diagrams, the non approximated converter delay transfer function was considered (Eq. (2.36)).

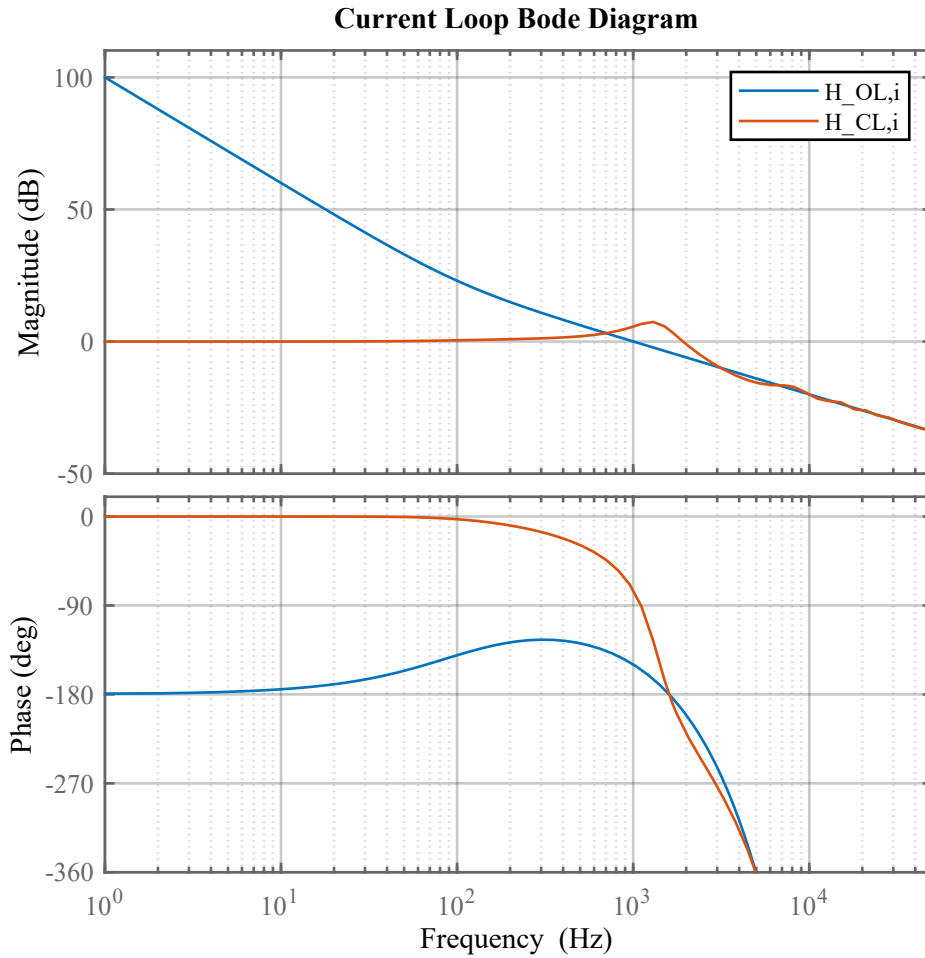


Figure 2.11: Bode diagram of the open loop and closed loop transfer function of the current control.

### Current Controller Feed Forward

In order to increase the performance of the loop under transients, a feed forward is used to reduce the effort of the integral part of the PI regulator. Its representation through a block diagram is shown in Fig. 2.12. The input is the same input reference as the PI controller input, while the output voltage  $v_{FFW}$  is added at the output of the controller. The cross product is an effect of the rotation transformation, which introduces a motional term. The more the estimation of the feed

forward voltage is accurate, and thus the more the PLL is accurate and the more the  $L_f$  is well known, the more the controller work load is relieved.

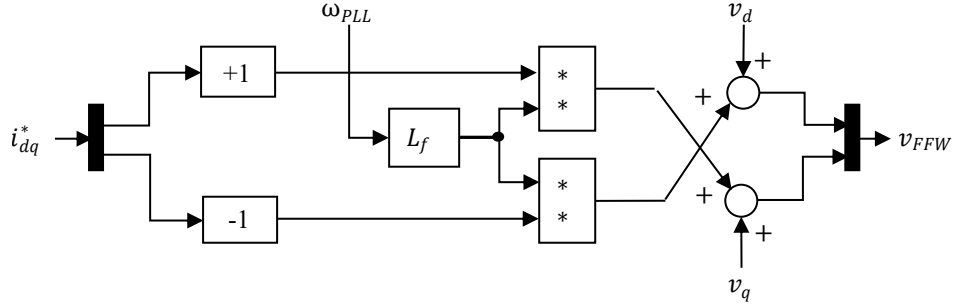


Figure 2.12: Block representation of the feed forward of the current loop controller.

### 2.2.4 DC-Link Voltage Control

A complete block representation of the inverter cascaded control is shown in Fig. 2.13.

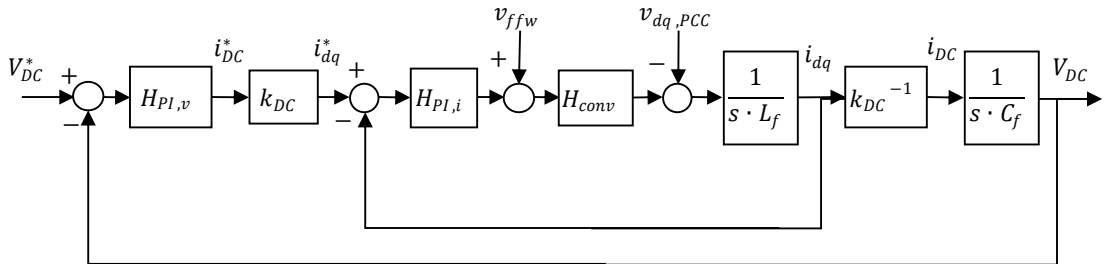


Figure 2.13: Block representation of the inverter cascaded control.

The output of the voltage control is a current referred to the DC side. However, since this forcing term is given as a reference input for the  $(d, q)$  current control, a proportionality factor  $k_{DC}$  can be used to consider the difference root mean square voltages on the DC and the AC side. If we equal the active power on both sides, and

if we consider all the voltage vector on the  $d$ -axis on the AC side, we can consider:

$$P_{DC} = P_{(d,q)} \quad (2.52)$$

$$V_{DC} \cdot I_{DC} = \frac{3}{2} \cdot (v_d \cdot i_d) \quad (2.53)$$

$$i_d = \frac{2}{3} \cdot \frac{V_{DC}}{v_d} \cdot I_{DC} \quad (2.54)$$

$$i_d = k_{DC} \cdot I_{DC} \quad (2.55)$$

where

$$k_{DC} = \frac{2}{3} \cdot \frac{V_{DC}}{v_d} \quad (2.56)$$

In this work the DC-Link was controlled at 400 V and the grid RMS phase voltage was at 120 V. Therefore a  $k_{DC}$  of  $20/9$  ( $\simeq 2.22$ ) can be considered.

In order to decouple the tuning of the current loop and the voltage loop, their transfer functions should not interfere with each other. If they interfere, the resulting transfer function would have a higher order and would present resonances that could be dangerous for the control operation. To avoid this interference, the bandwidth frequency of the voltage loop should be at least a decade smaller than the bandwidth frequency of the current loop. If this occurs, the current control loop can be approximated with an unitary gain, and the block representation becomes as shown in Fig. 2.14.

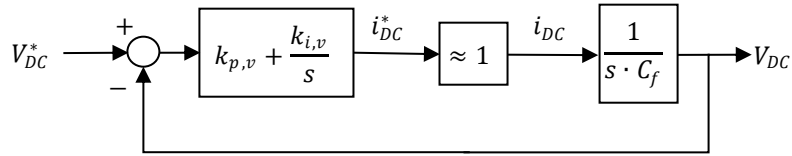


Figure 2.14: Block representation of the inverter DC-Link voltage loop.

The reader should notice that the DC-Link generally operates at a constant voltage reference which is chosen in the design stage and which does not vary, therefore the aim of the voltage control is to overcome small voltage variations due to changes in the absorbed or generated power, but does not need fast dynamics. The tuning in this work was thus done with the hypothesis that the voltage loop bandwidth was sufficiently smaller than the current loop bandwidth.

Referring to the simplification shown in Fig. 2.14, the open loop transfer function is:

$$H_{OL,v}(s) = \left( k_{p,v} + \frac{k_{i,v}}{s} \right) \cdot \frac{1}{s \cdot C_{DC}} \quad (2.57)$$

In order to study the bandwidth of (2.57), an approximation of the open loop transfer function at high frequencies is:

$$H_{OL,v}(s) \Big|_{hf} \simeq \frac{k_{p,v}}{s \cdot C_{DC}} \quad (2.58)$$

The crossover frequency can be calculated as:

$$|H_{OL,v}(\omega_{bw,v})| = 1 \simeq \frac{k_{p,v}}{\omega_{bw,v} \cdot C_{DC}} \quad (2.59)$$

$$\omega_{bw,v} = \frac{k_{p,v}}{C_{DC}} \quad (2.60)$$

The proportional gain of the voltage controller can therefore be calculated as:

$$k_{p,v} = \omega_{bw,v} \cdot C_{DC} \quad (2.61)$$

In order to reject disturbances on the DC-Link, a crossover frequency of 20 Hz was considered. As for the zero of the controller  $\omega_{z,v}$ , the same criteria used for the current controller was adopted. Thus it was positioned a decade before the voltage bandwidth frequency.

$$\omega_{z,v} = \frac{\omega_{bw,v}}{10} \quad (2.62)$$

The integral gain of the controller can be therefore calculated as:

$$k_{i,v} = k_{p,v} \cdot \omega_{z,v} \quad (2.63)$$

Results of the tuning are shown in Table 2.6.

Using the values of Table 2.6 in (2.57) the Bode diagram of the open and closed loop transfer function can be calculated, as shown in Fig. 2.15.

The full control of the inverter, which contains the current control, the voltage control and the PLL, is shown through a block diagram in Fig. 2.16.

Parameter	Value
$f_{bw,v}$	20 Hz
$\omega_{bw,v}$	125.66 rad/s
$f_{z,v}$	2 Hz
$\omega_{z,v}$	12.57 rad/s
$k_{p,v}$	0.2262 S
$k_{i,v}$	2151.574 rad·S/s
Phase margin	84.3°

Table 2.6: Voltage loop set-up values.

## 2.2.5 Modulation Scheme

For a three-phase inverter, many types of PWM techniques are available. The most common are:

- **Sinusoidal PWM (SPWM):** this is the most simple type of modulation. It consists in the comparison of a three phase balanced sinusoidal reference signal with a high frequency carrier signal. The result of the comparison, *i.e.* 1 if the reference is greater than the carrier and 0 otherwise, is used as input to the inverter gate drivers. The total harmonic distortion of the output voltage is reduced by increasing the frequency of the carrier, but this leads to major switching losses as well. The main advantage is its simplicity in implementation and low computational burden, since only a multiplication per phase is required.
- **Third harmonic injection:** this technique exploits the advantage of third harmonic rejection of three phase systems in order to produce a 15 % higher output voltage without over modulation. In fact, third harmonics are in phase with each other on the three output voltages and therefore their contribute is absent on line to line voltages. Moreover, on a system with three wires third harmonic currents cannot circulate. By exploiting this phenomenon, we can use a reference signal with a fundamental component which is greater than the peak of the carrier signal with a third harmonic component phased so that the resulting reference signal is lower than the peak of the carrier. Only the

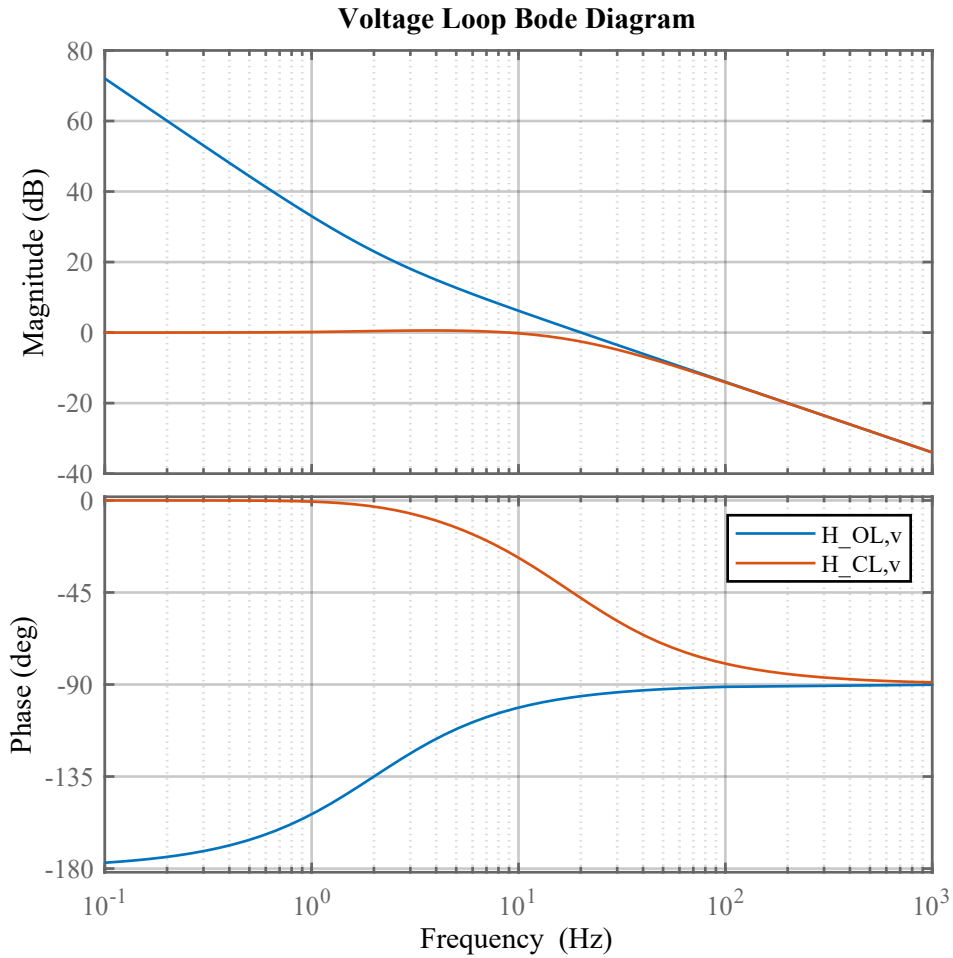


Figure 2.15: Bode diagram of the open loop and closed loop transfer function of the voltage control.

fundamental component will affect the load, while the third harmonic will be rejected.

- **Space Vector Modulation (SVM)**: this is the most popular technique among three phase VSIs<sup>3</sup>. It differs from the third harmonic injection only on the over modulation region, where it allows a higher fundamental voltage.

---

<sup>3</sup>VSI = Voltage Source Inverter

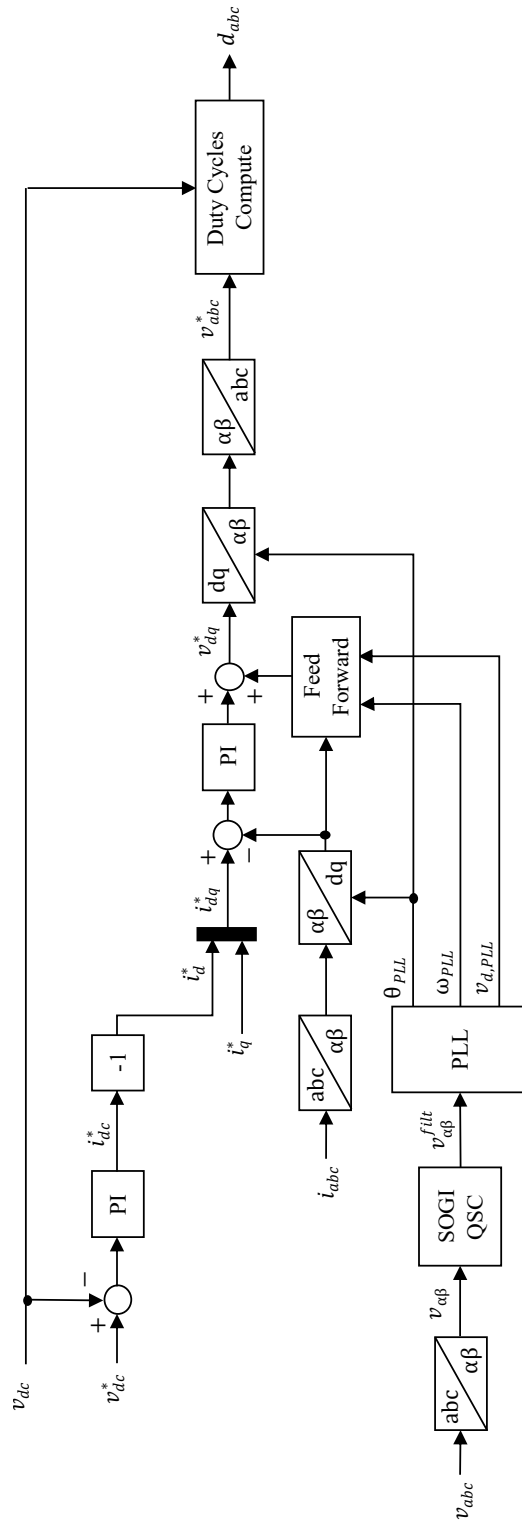


Figure 2.16: Block diagram representing the full control of the inverter.

It is, however, much more complex and computationally heavier than the third harmonic injection.

Since the main goal of this work is not to maximize the performances of the control, for a major simplicity space vector modulation is not used. Instead, a modulation technique with a third harmonic injection was used. The most optimal technique is called *Balanced Envelope Modulation* (BEM), and uses as third harmonic a common mode signal that balances the envelopes of the sinusoidal references.

If the positive envelope is  $s_p$  and the negative is  $s_n$ :

$$s_p = \max(v_r, v_s, v_t) \quad (2.64)$$

$$s_n = \min(v_r, v_s, v_t) \quad (2.65)$$

We want to find a common mode signal that balances the envelopes  $s_{cm}$ . If we call the balanced envelopes  $s'_p$  and  $s'_n$ , we can write:

$$s'_p = s_p + s_{cm} \quad (2.66)$$

$$s'_n = s_n + s_{cm} \quad (2.67)$$

Since  $s'_p$  and  $s'_n$  are balanced, their sum is zero:

$$s'_p + s'_n = 0 \quad (2.68)$$

By substituting (2.66) and (2.67) in (2.68),  $s_{cm}$  can be calculated as:

$$s_{cm} = -\frac{s_p + s_n}{2} \quad (2.69)$$

Since the sum of the voltages is equal to zero, (2.69) can be rewritten as:

$$s_{cm} = \frac{s_t}{2} \quad (2.70)$$

Where  $s_t$  is the voltage in transition between the positive envelope  $s_p$  and the negative envelope  $s_n$ . Both (2.69) and (2.70) produce the same results.

This modulation can be represented through a block diagram as shown in Fig. 2.17.

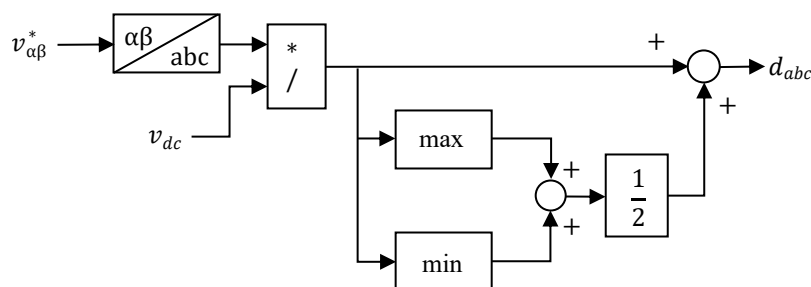


Figure 2.17: Block diagram of the Balanced Envelope Modulation

## 2.3 DC/DC Converter Control

A DC/DC converter on the DC side of the inverter can be useful for various reasons:

- It minimizes the overall converter cost in applications where the input voltage can vary in a fairly wide range. A battery system for automotive applications, for instance, can have a nominal voltage that is typically around 350 V, but the actual voltage depends on its state of charge and can vary of various tens of volts. In order to reduce the overall cost of semiconductors and reactive elements, it can be useful to use a DC/DC converter that adapts the output DC voltage to the maximum possible voltage for the load or generation application. This minimizes the current sizing of the inverter semiconductors.
- Depending on the application, a DC/DC converter could be mandatory to manage the DC load. For instance, it is necessary in order to manage a battery charging process, or to manage the MPPT in a solar array.

For these reasons, the converter in this work considers an input voltage which can vary but does not exceed 400 V, which is the DC-Link set-point.

The DC/DC converter that was considered for this work is a step-up converter with a simple boost structure, as shown in Fig. 2.18.

The converter is controlled by a closed loop current control. This is independent from the inverter control, although executed during the same ISR. Using a Laplace domain block representation, it can be considered as shown in Fig. 2.19. The open loop transfer function is thus:

$$H_{OL,boost}(s) = \left( k_{p,boost} + \frac{k_{i,boost}}{s} \right) \cdot e^{-s \cdot \tau_{conv}} \cdot \frac{1}{s \cdot L_{DC}} \quad (2.71)$$

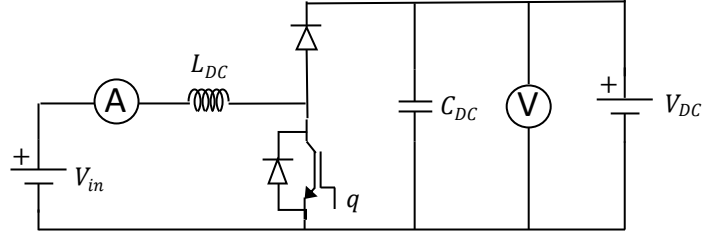


Figure 2.18: Adopted DC/DC converter (boost).

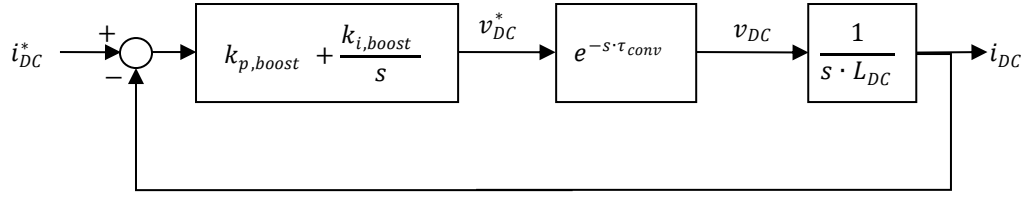


Figure 2.19: DC/DC converter current loop.

Due to the independence of the control from the control of the inverter, the maximum obtainable bandwidth is a decade inferior to the switching frequency, *i.e.* 1000 Hz. The formulas for the tuning of the control loop are analogous to the ones of the inverter current control, and thus will not be explained again.

As done before, a PI controller is used. The zero of the controller is positioned a decade before the crossover frequency of the loop. The gains can therefore be calculated as follows:

$$k_{p,boost} = \omega_{bw,boost} \cdot L_{DC} \quad (2.72)$$

$$k_{i,boost} = k_{p,boost} \cdot \omega_{z,boost} \quad (2.73)$$

Table 2.7 shows the loop crossover frequencies, the PI controller settings and the phase margin considered in this work for the DC/DC converter.

The Bode diagram was obtained using the values in Table 2.7, and is shown in Fig. 2.20. The non approximated converter delay transfer function was considered.

The adopted current control can be represented through a block diagram as shown in Fig. 2.21.

Parameter	Value
$f_{bw,boost}$	1000 Hz
$\omega_{bw,boost}$	6283.2 rad/s
$f_{z,boost}$	100 Hz
$\omega_{z,boost}$	628.3 rad/s
$k_{p,boost}$	62.83 S
$k_{i,boost}$	39478.4 rad·S/s
Phase margin	30°

Table 2.7: DC/DC converter current loop set-up values.

## 2.4 PLECS Implementation

The converter control was first implemented on the power electronics simulation platform PLECS, in order to validate the controller design. At first it was realized through blocks to test if the logical procedure was correct. Then it was written in a C-Script block to test the code that would have been implemented on the real converter.

The PLECS representation of the electrical circuit with the converter connected to a grid equivalent model is shown in Fig. 2.22, while the control is shown in Fig. 2.23.

## 2.5 C-Script Implementation

The real implementation of the control on the converter is done on a ISR<sup>4</sup> script written in C. Therefore, after the realization of the control through PLECS blocks, it was implemented in a C-Script block. The full code is reported in the Appendix for reference.

This section will highlight the differences from the block control (Fig. 2.23).

With respect to the block control, in the C-Script (and therefore in the control implemented on the physical converter) some parts were added:

---

<sup>4</sup>Interrupt Service Routine

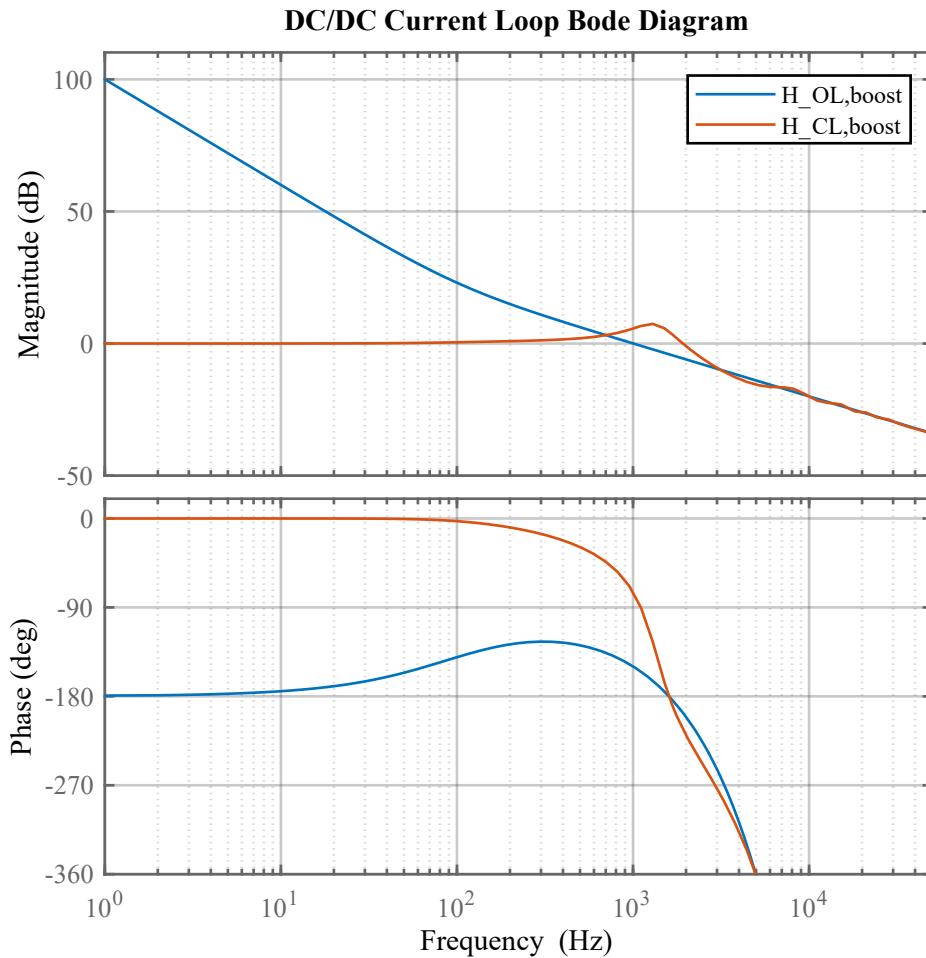


Figure 2.20: DC/DC converter Bode diagram for the current loop.

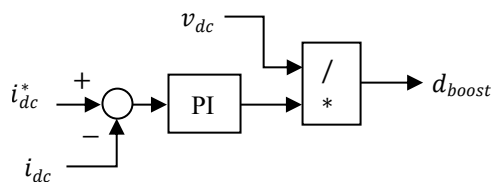


Figure 2.21: DC/DC converter control block diagram.

- **Over current/Over voltage protection:** Since on a real converter semi-conductors have to be protected against currents and voltages that are higher to their rated values with a safety margin, the first check that is done on the

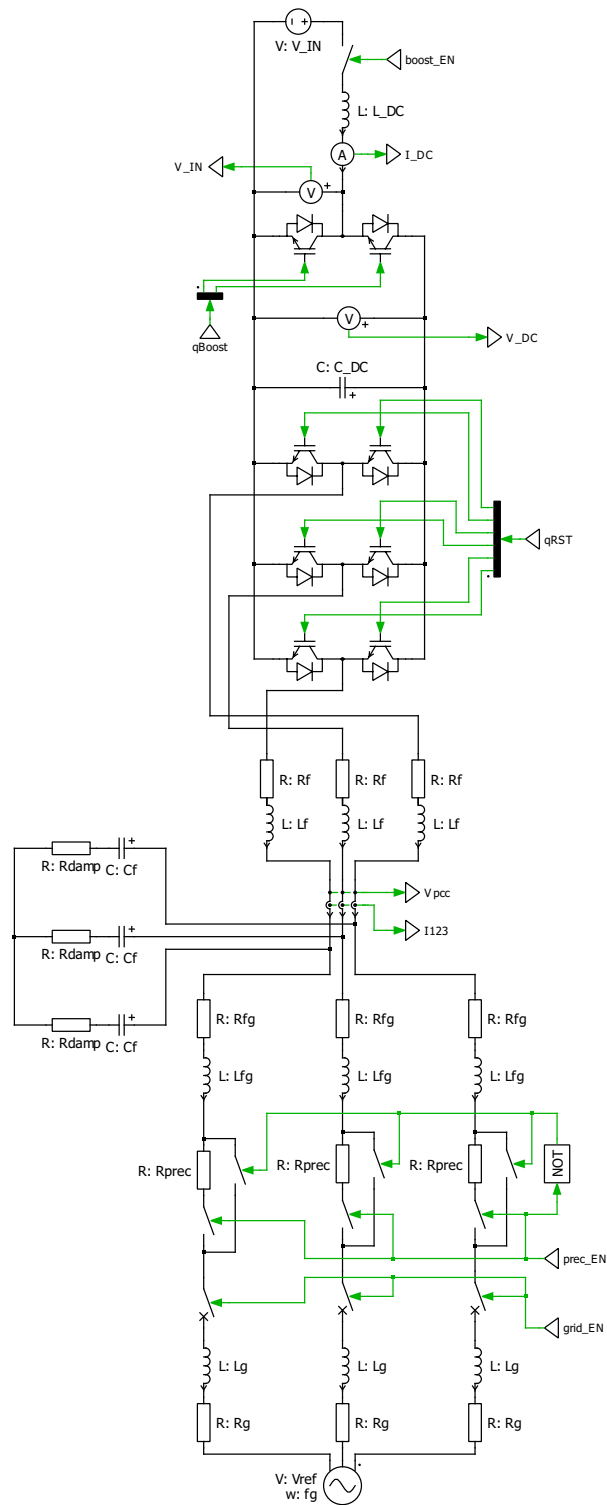


Figure 2.22: PLECS representation of the converter and grid circuit.



```

1 tmp1      = (Iabc.a + Iabc.b + Iabc.c)*one_third;
2 Iabc.a    -= tmp1;
3 Iabc.b    -= tmp1;
4 Iabc.c    -= tmp1;

```

- **Voltage filtering:** The DC-link voltage has a very low ripple, but due to measurement noise a false disturbance may appear in the control. For this reason, it is good practice to filter the sampled DC voltage with a first order digital low pass filter with a pole set at the crossover frequency of the voltage loop (*i.e.* 20 Hz).

$$H_{LPF} = \frac{1}{s + 2 \cdot \pi \cdot 20} \quad (2.74)$$

The discretization of the filter is done in the following way:

```

1 Vdc_filt  += k_LPF_v*(Vdc - Vdc_filt);

```

where  $k\_LPF\_v$  is:

$$k\_LPF\_v = T_s \cdot 2 \cdot \pi \cdot 20 \quad (2.75)$$

and  $T_s$  is the period of the ISR.

- **SOGI state space implementation:** Since the SOGI filter is a second order transfer function, in order to obtain a good discretization it is necessary to pass to a state space representation and then discretize it. This process has been done by [7] and [19]. If we consider the SOGI block representation through the dynamic system represented in Fig. 2.24, a state space representation can be obtained by writing the equations of  $x_1$  and  $x_2$ .

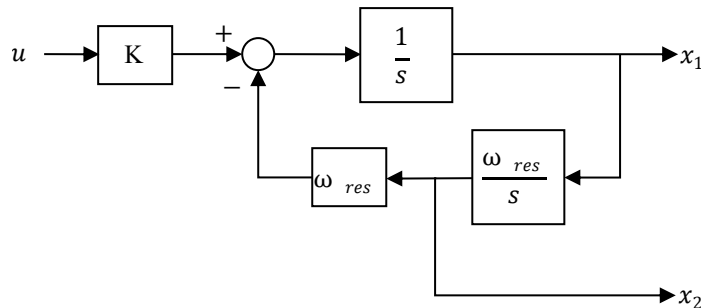


Figure 2.24: SOGI block representation.

$$x_1 = \frac{k \cdot u - x_2 \cdot \omega_{res}}{s} \quad (2.76)$$

$$x_2 = x_1 \cdot \frac{\omega_{res}}{s} \quad (2.77)$$

We can therefore consider:

$$\begin{cases} \dot{x} = A \cdot x + B \cdot u \\ y = C \cdot x + u \end{cases} \quad (2.78)$$

where

$$\mathbf{A} = \begin{bmatrix} 0 & -\omega_{res} \\ \omega_{res} & 0 \end{bmatrix} \quad \mathbf{B} = K \quad (2.79)$$

$$\mathbf{C} = \begin{bmatrix} 1 & 1 \end{bmatrix} \quad \mathbf{D} = 0$$

The discretization can be done with the following formulas:

$$\mathbf{A}_d = e^{\mathbf{A} \cdot T_s} \quad (2.80)$$

$$\mathbf{B}_d = \mathbf{B} \cdot \int_0^{T_s} e^{\mathbf{A} \cdot T_s} d\tau = \mathbf{A}^{-1} \cdot (\mathbf{A}_d - \mathbf{I}) \cdot \mathbf{B} \quad (2.81)$$

Although an analytic evaluation of (2.80) and (2.81) is possible and has been done by [7] and [19], it is not the aim of this work. Therefore the numeric matrices of  $\mathbf{A}$  and  $\mathbf{B}$  were considered and (2.80) and (2.81) were directly computed through MATLAB.

- **First estimation of PLL angle:** in the simulation done through blocks the voltage vector angle starts at zero, and reaches the correct value after a transient. In the C-Script, at the first ISR the angle is estimated performing an arc-tangent of the  $(\alpha, \beta)$  frame voltages. This reduces the PLL transient and speeds up the start-up of the converter. This estimation is done in the following way:

```

1  if (FIRST_TIME) {
2      Sin_Cos_theta.cos = Vab.alpha/Vab_peak;
3      Sin_Cos_theta.sin = Vab.beta/Vab_peak;
4      theta_PLL = atan2(Sin_Cos_theta.sin, Sin_Cos_theta.cos);
5      FIRST_TIME = 0;
6  }
```

- **ERROR state:** the initial state is an ERROR state. Here all the control variables are reset. The control starts up when a user button is pressed, to emulate the real functioning of the physical converter. A pulse generator with a low frequency emulates the user that presses the user button. The variable USER\_BUTTON is an input which was not present in the block control. Moreover, when over voltages and over currents occur, the control is set to the ERROR state. In this state the variable GRID\_EN, which controls the circuit breaker that connects the converter to the grid, is set to 0. Therefore the converter gets disconnected to the grid in case of over currents and voltages.
- **Start-up states:** before the control loops are started, the C-Script control waits that the capacitors are charged and the PLL is synced. This is done through two states:
  - *PRECHARGE state:* this state is in charge of the precharge of the capacitors. At first the converter is connected to the grid by setting the GRID\_EN variable to 1. Then the precharge is started by setting the PREC\_EN variable to 1. This variable opens the circuit breaker on the short circuit over the precharge resistors and closes the circuit breaker before the resistors. Then a counter counts the time. Since the DC-Link capacitor is much bigger than the LCL filter capacitors, only this voltage is checked, assuming that when the DC-Link capacitor is charged the LCL filter capacitors are surely charged. The conditions to end this state and pass to the next one are a minimum time of 0.2 seconds and the DC-Link voltage over 90% of the peak of the grid voltage. The reader should notice that, since precharge resistors are activated, due to the voltage drop across the resistors the DC-Link voltage cannot be equal to the peak of the grid voltage. When these conditions are met PREC\_EN is set to 0 and the state is set to SYNC. This state is evaluated in the following way:

```

1  case PRECHARGE:
2      GRID_EN = 1; // Connection to grid
3      PREC_EN = 1; // Precharge resistors are connected
4      counter++;
5      if ( (counter > 2000) & (Vdc > 0.9 * VgLL_pk) ){

```

```

6     counter    = 0;
7     PREC_EN    = 0;
8     STATE      = SYNC;
9     }
10    break;

```

- *SYNC state*: this state waits for the PLL to synchronize with the grid. When PLL is synchronized, the voltage on the  $q$ -axis tends to zero. The condition to exit this state is to have a  $v_q$  inferior to a threshold contained in the variable `th_PLL` and set to 0.1. Since  $v_q$  starts from zero and increases through an initial transient, a time of 0.1 seconds has to pass before the check is done. This state is evaluated in the following way:

```

1    case SYNC:
2        counter++;
3        if ( (counter > 1000) & (Vdq.q <= th_PLL) ){
4            counter = 0;
5            STATE = READY;
6        }
7    break;

```

- *READY state*: when both the PRECHARGE and SYNC states have ended, the control waits in a READY state that is connected to the grid but does not modulate the switches, waiting for an input from the user through the user button. When this is pressed, the control passes to the START state and the control loops are evaluated.



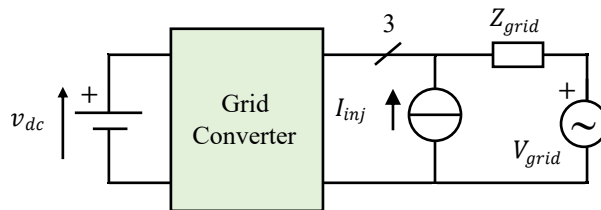
## Chapter 3

# Impedance Measurement Through Signal Injection

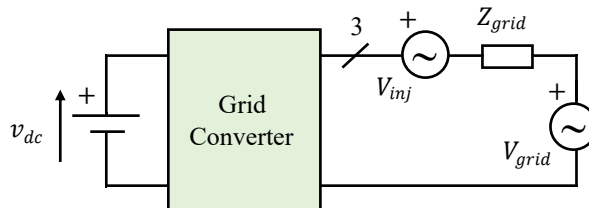
The measurement of the converter impedance can be carried out by considering a perturbation signal injected in the converter system. These methods have been analysed in technical literature by many authors, among which [5], [12], [13], [16] and [27].

All of these methods have in common the injection of a perturbation signal and the computation of an equivalent impedance based on the observation of the system response. Two types of injection can be considered:

- **Current source perturbation:** a current generator is connected in parallel with a converter and injects a current at a test frequency. Since the converter is a non-linear system, it must be connected to the grid and work at a chosen operating point upon which to perform linearisation. The obtained equivalent impedance will be therefore valid around that point. A simplified single-line diagram is shown in Fig. 3.1a.
- **Voltage source perturbation:** a voltage generator is connected in series with the converter and the grid. The considerations done for the current injection method on non-linearity are still valid. A simplified single-line diagram is shown in Fig. 3.1b.



(a) Single-line diagram of a circuit with current source perturbation.



(b) Single-line diagram of a circuit with voltage source perturbation.

Figure 3.1: Simplified single-line diagrams of signal injection test circuits.

All of the considered solutions in literature used a current injection, although cited the possibility to adopt a voltage injection as well. Moreover, most of the solutions considered simple situations of converters connected to passive loads or other converters and controlled without cascaded controls. Only [5] considered a grid-connected converter. This work explores the possibility of impedance characterization through voltage injection with multiple-stadium grid-connected converters with cascaded controls.

### 3.1 Problems of Signal Injection Methods Applied to Power Converters

Since only one measurement at a time is possible, all of the signal injection techniques require as a fundamental hypothesis that the system is working in a stable operating point at steady state, *i.e.* sequential or simultaneous measurements would produce the same results. Moreover, measurements can be repeated as many times as necessary, always retrieving the same results.

The non-linearity of the system and therefore the necessity to work at a specific operating point in order to take measurements is an issue. In fact, many power

converters are designed to work at high power levels and this reflects the operating points to be considered. This usually precludes the possibility to use commercially available impedance analyser equipments, which produce accurate results but cannot be used on an active converter at a high power operating point.

DC impedance measurement through signal perturbation for DC systems has been already widely analysed in technical literature. These systems require as well an operating point for the measurements to be taken. However there is no need to process voltages and currents in order to transform the measurements into a  $(d, q)$  rotating reference frame, as requested instead in a three-phase AC system. Therefore commercial impedance analysers can be directly connected to amplifiers in order to perform injections. This is not the case of impedance measurement for AC systems, where a change of coordinates is necessary to refer the measured outputs to a rotating reference frame.

## 3.2 Formulation of the Impedance Matrix

In impedance estimation through signal injection, the measurements must be referred to a  $(d, q)$  rotating reference frame. In order to obtain the fundamental voltage vector on the  $d$ -axis, the PLL output angle  $\hat{\theta}$  is used for the reference frame rotation. We can therefore consider through the Ohm's Law the link between  $(d, q)$  currents and voltages:

$$\begin{bmatrix} V_d \\ V_q \end{bmatrix} = \begin{bmatrix} Z_{dd} & Z_{dq} \\ Z_{qd} & Z_{qq} \end{bmatrix} \cdot \begin{bmatrix} I_d \\ I_q \end{bmatrix} \quad (3.1)$$

where  $V_d$ ,  $V_q$ ,  $I_d$  and  $I_q$  can all be peak values or all RMS values without difference in the impedance matrix  $\mathbf{Z}$ .

As explained in [12], in order to find an expression of  $\mathbf{Z}$  two tests have to be considered with two linearly independent perturbation signals:

$$\begin{cases} V_{d,1} = Z_{dd} \cdot I_{d,1} + Z_{dq} \cdot I_{q,1} \\ V_{q,1} = Z_{qd} \cdot I_{d,1} + Z_{qq} \cdot I_{q,1} \end{cases} \quad (3.2)$$

$$\begin{cases} V_{d,2} = Z_{dd} \cdot I_{d,2} + Z_{dq} \cdot I_{q,2} \\ V_{q,2} = Z_{qd} \cdot I_{d,2} + Z_{qq} \cdot I_{q,2} \end{cases} \quad (3.3)$$

As for the expressions of  $V_d$ , (3.2) and (3.3) can be rewritten as:

$$\begin{cases} V_{d,1} = Z_{dd} \cdot I_{d,1} + Z_{dq} \cdot I_{q,1} \\ V_{d,2} = Z_{dd} \cdot I_{d,2} + Z_{dq} \cdot I_{q,2} \end{cases} \quad (3.4)$$

and in matrix form (3.4) becomes:

$$\begin{bmatrix} V_{d,1} \\ V_{d,2} \end{bmatrix} = \begin{bmatrix} I_{d,1} & I_{q,1} \\ I_{d,2} & I_{q,2} \end{bmatrix} \cdot \begin{bmatrix} Z_{dd} \\ Z_{dq} \end{bmatrix} \quad (3.5)$$

Therefore an expression of  $Z_{dd}$  and  $Z_{dq}$  can be obtained by rearranging (3.5):

$$\begin{bmatrix} Z_{dd} \\ Z_{dq} \end{bmatrix} = \begin{bmatrix} I_{d,1} & I_{q,1} \\ I_{d,2} & I_{q,2} \end{bmatrix}^{-1} \cdot \begin{bmatrix} V_{d,1} \\ V_{d,2} \end{bmatrix} \quad (3.6)$$

The same reasoning can be applied to  $V_q$  in order to find  $Z_{dd}$  and  $Z_{dq}$ , allowing to rewrite (3.2) and (3.3) as:

$$\begin{bmatrix} Z_{qd} \\ Z_{qq} \end{bmatrix} = \begin{bmatrix} I_{d,1} & I_{q,1} \\ I_{d,2} & I_{q,2} \end{bmatrix}^{-1} \cdot \begin{bmatrix} V_{q,1} \\ V_{q,2} \end{bmatrix} \quad (3.7)$$

Then (3.6) and (3.7) can be united in:

$$\begin{bmatrix} Z_{dd} & Z_{qd} \\ Z_{dq} & Z_{qq} \end{bmatrix} = \begin{bmatrix} I_{d,1} & I_{q,1} \\ I_{d,2} & I_{q,2} \end{bmatrix}^{-1} \cdot \begin{bmatrix} V_{d,1} & V_{q,1} \\ V_{d,2} & V_{q,2} \end{bmatrix} \quad (3.8)$$

The reader should notice that the impedance matrix of (3.8) is not correct, since its transpose has to be considered:

$$\begin{aligned} \begin{bmatrix} Z_{dd} & Z_{dq} \\ Z_{qd} & Z_{qq} \end{bmatrix} &= \left( \begin{bmatrix} I_{d,1} & I_{q,1} \\ I_{d,2} & I_{q,2} \end{bmatrix}^{-1} \cdot \begin{bmatrix} V_{d,1} & V_{q,1} \\ V_{d,2} & V_{q,2} \end{bmatrix} \right)^t \\ &= \begin{bmatrix} V_{d,1} & V_{q,1} \\ V_{d,2} & V_{q,2} \end{bmatrix}^t \cdot \left( \begin{bmatrix} I_{d,1} & I_{q,1} \\ I_{d,2} & I_{q,2} \end{bmatrix}^t \right)^{-1} \\ &= \begin{bmatrix} V_{d,1} & V_{d,2} \\ V_{q,1} & V_{q,2} \end{bmatrix} \cdot \begin{bmatrix} I_{d,1} & I_{d,2} \\ I_{q,1} & I_{q,2} \end{bmatrix}^{-1} \end{aligned} \quad (3.9)$$

We can therefore consider a compact notation:

$$\mathbf{Z} = \mathbf{V} \cdot \mathbf{I}^{-1} \quad (3.10)$$

where

$$\mathbf{Z} = \begin{bmatrix} Z_{dd} & Z_{dq} \\ Z_{qd} & Z_{qq} \end{bmatrix} \quad \mathbf{V} = \begin{bmatrix} V_{d,1} & V_{d,2} \\ V_{q,1} & V_{q,2} \end{bmatrix} \quad \mathbf{I} = \begin{bmatrix} I_{d,1} & I_{d,2} \\ I_{q,1} & I_{q,2} \end{bmatrix}$$

### 3.2.1 Choice of the Perturbation Signal

It is necessary to remind and highlight how the two perturbation signals must be linearly independent. If this is not true, it is impossible to compute the inverse of the current matrix. Various approaches are available to achieve perturbation independence:

- [12] considers a perturbation vector with different phase in the two cases. This approach can be called *Phase Variation Method*.
- [27] considers two different frequencies in the three phase reference frame that transformed into  $(d, q)$  produce the same perturbation frequency. Subsection 3.2.2 explains this approach. This approach can be called *Mirror Frequencies Method*.

### 3.2.2 Signal Frequency Change in the $(d, q)$ Domain

When a three phase sequence is transformed into the  $(d, q)$  frame using a rotation angle that is different from the one of the sequence rotating vector, its frequency in the  $(d, q)$  changes, and the new frequency depends on the sequence rotation direction. A positive sequence is considered:

$$\begin{cases} V_{r,p} = \hat{V}_p \cdot \cos(\omega_p \cdot t) \\ V_{s,p} = \hat{V}_p \cdot \cos(\omega_p \cdot t - \frac{2\pi}{3}) \\ V_{t,p} = \hat{V}_p \cdot \cos(\omega_p \cdot t + \frac{2\pi}{3}) \end{cases} \quad (3.11)$$

An amplitude invariant Clarke transformation is applied:

$$\begin{cases} V_{\alpha,d} = \hat{V}_p \cdot \cos(\omega_p \cdot t) \\ V_{\beta,d} = \hat{V}_p \cdot \sin(\omega_p \cdot t) \end{cases} \quad (3.12)$$

A rotation transformation is applied with frequency  $\omega_r$ :

$$\begin{cases} V_{d,d} = \hat{V}_p \cdot \cos((\omega_p - \omega_r) \cdot t) \\ V_{d,d} = \hat{V}_p \cdot \sin((\omega_p - \omega_r) \cdot t) \end{cases} \quad (3.13)$$

Therefore:

$$\omega_{dq} = \omega_p - \omega_r \quad (3.14)$$

If the same transformations are applied to a negative sequence:

$$\begin{cases} V_{d,n} = \hat{V}_n \cdot \cos((\omega_n + \omega_r) \cdot t) \\ V_{d,n} = -\hat{V}_n \cdot \sin((\omega_n + \omega_r) \cdot t) \end{cases} \quad (3.15)$$

Therefore

$$\omega_{dq} = \omega_r + \omega_n \quad (3.16)$$

The same  $(d, q)$  perturbation signal can be obtained with two different frequencies. If a perturbation frequency  $\omega_{dq}$  in the  $(d, q)$  frame is needed, it can be obtained with two different three phase signals:

- a positive sequence rotating in the three phase frame at  $\omega_p = \omega_{dq} + \omega_r$
- a negative sequence rotating in the three phase frame at  $\omega_n = \omega_{dq} - \omega_r$

If the rotation frequency  $\omega_r$  is the PLL output frequency (*i.e.* the fundamental voltage frequency), then positive and negative sequence perturbations are defined at two different frequencies which are shifted by twice the fundamental frequency. These frequencies are called by [27] *mirror frequencies*.

### 3.3 Mirror Frequencies Method

As already described in Section 3.2.1, the Mirror Frequencies Method considers for the two tests two perturbation signals at different frequencies in the three phase reference frame. Once these signals are transformed into the  $(d, q)$  frame, however, they are at the same frequency (as explained in Section 3.2.2). Fig 3.2 shows the procedure.

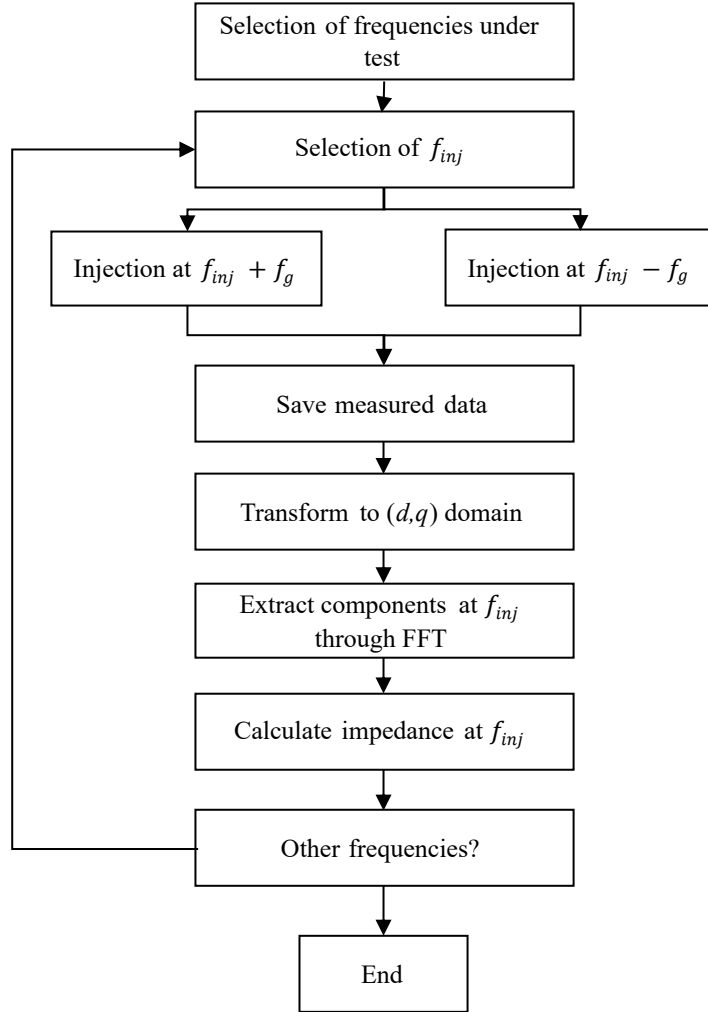


Figure 3.2: Signal Injection Scheme.

At first a list of  $(d, q)$  frequencies to test must be generated. In order to obtain equally spaced points on the Bode diagram, a logarithmically spaced vector should be considered. Then frequencies must be selected one by one and two tests are performed: the first one is with a direct sequence at higher mirror frequency, while the second one is with an inverse sequence at the lower mirror frequency. The measurements are then transformed to the  $(d, q)$  frame and the harmonic frequency of interest is extracted through a Fast Fourier Transform. Depending on the resolution of the FFT, if few data are available the perturbation could not be found exactly at  $f_{inj}$  but near to this value. Therefore a search for the highest harmonic amplitude in frequencies near  $f_{inj}$  could be necessary. However, if this solution is

chosen, the input perturbation must produce a response which high enough to be distinguishable from possible disturbances. When average peak or RMS value of currents and voltages at the perturbation frequency are found, impedance can be calculated through 3.9. This procedure is repeated for every frequency.

## 3.4 RL Circuit Analysis Through Voltage Injection

At first, to validate the methodology, an attempt to measure an impedance through the injection of a perturbation signal was performed through simulation in a simple circuit. In order to check if the computed impedance was coherent with the real one, a basic RL circuit was considered.

The  $(d, q)$  impedance of an RL circuit  $Z_{RL}$  is:

$$Z_{RL} = \begin{bmatrix} R + s \cdot L & -\omega_r \cdot L \\ \omega_r \cdot L & R + s \cdot L \end{bmatrix} \quad (3.17)$$

This impedance can be easily obtained through the procedure shown in Appendix D.

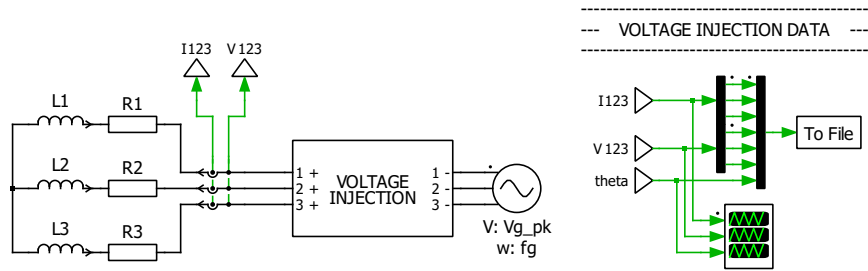
The adopted approach was a voltage perturbation injection with the Mirror Frequencies Method, as explained in Section 3.3.

### 3.4.1 PLECS Implementation

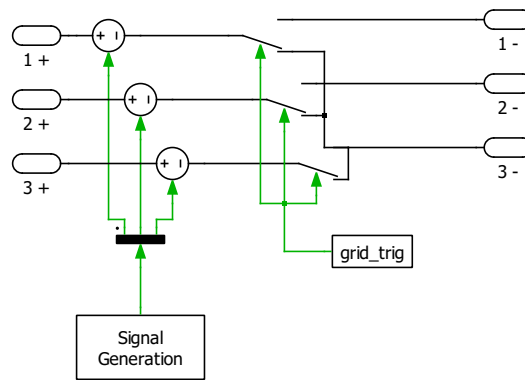
These tests were performed in a *PLECS* simulation, as shown in Fig. 3.3.

As the reader can notice, the voltage injection generators are connected in series with the impedance under test. They are controlled by a subsystem that generates:

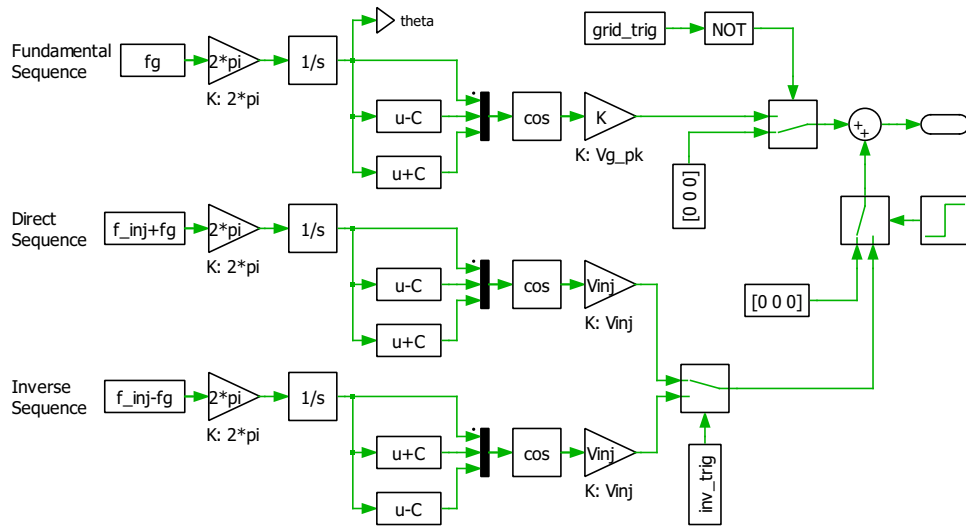
- a fundamental three phase signal at the grid frequency  $f_g$ . This signal can be activated or deactivated by the variable `grid_trig` depending on the presence or not of a three phase generator connected to the voltage injection block.
- a positive sequence three phase signal at the frequency  $f_{inj} + f_g$ .



(a) PLECS equivalent of the electrical circuit.



(b) Voltage Injection Subsystem.



(c) Signal Generation Subsystem.

Figure 3.3: PLECS equivalent of a voltage injection test for an RL circuit.

- a negative sequence three phase signal at the frequency  $f_{inj} - f_g$ .

The variable `inv_trig` selects the positive or negative sequence input depending on the test. A step activates the signal injection only when the RL circuit connected to the three phase generator has reached a steady state.

Figure 3.4 shows a fragment of a measurement of three-phase values with a positive sequence injection at 1 Hz at steady state.

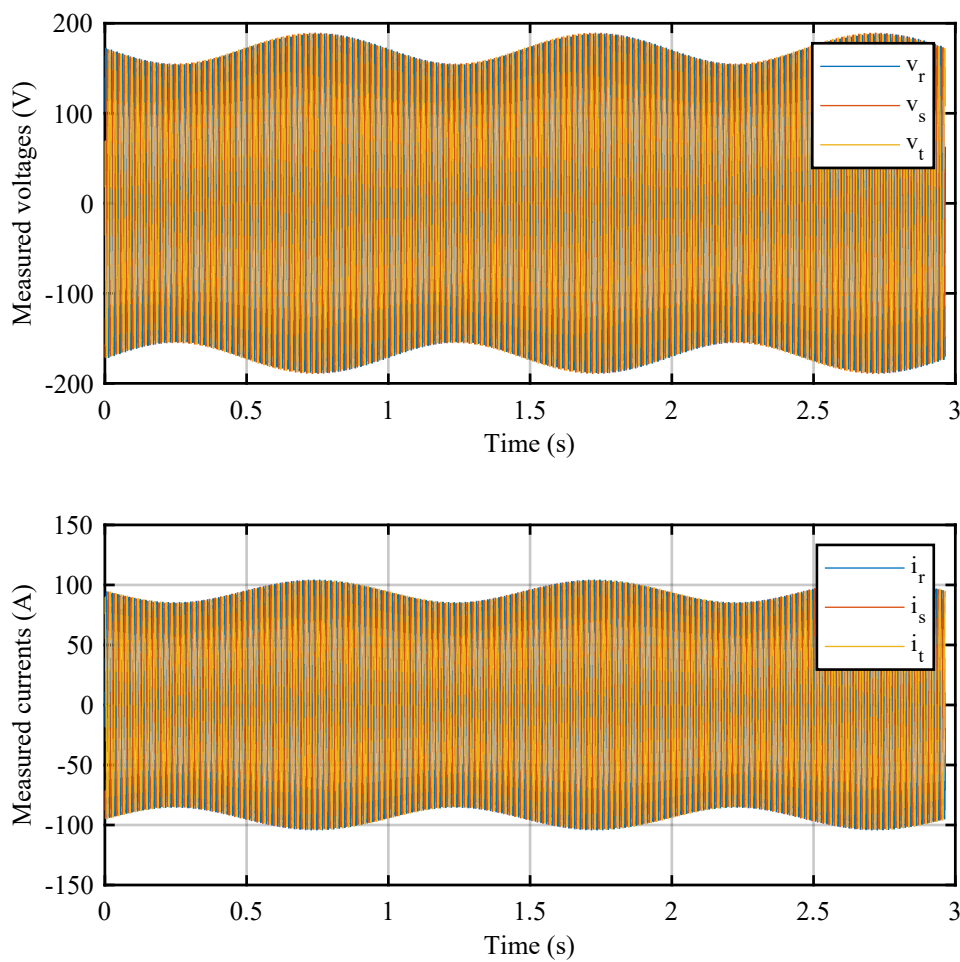


Figure 3.4: Voltages and currents with a voltage perturbation at 1 Hz.

An Octave-based simulation script is responsible for choosing the injected frequency and the sequence direction rotation. The code is available in Appendix D.

The script generates a vector of 100 logarithmically spaced frequencies that will be used for the perturbation. Then the necessary simulation time is calculated by considering from the start of the injection either 20 periods at the selected injected frequency if the total time is superior to 1 second or 1 second of simulation time otherwise. The start of the injection is set at a certain time in order to let the circuit reach a steady state. Then a first test is performed with a positive sequence perturbation at  $f_{inj} + f_g$  and the results are saved in a file. At the end of the first test a second one is performed with a negative sequence at the frequency  $f_{inj} - f_g$  and results are saved. Therefore two files are generated for each frequency: one for the positive and one for the negative sequence.

### 3.4.2 Processing of the Measurement

At the end of all the simulations the result files are processed by a MATLAB script that performs a loop in which saved data for every considered frequency is analysed. A flow chart of the algorithm is shown in Fig. 3.5.

The adopted procedure is explained below:

1. A frequency vector is generated. This must be the same as the vector used in the Octave script.
2. The first step is to choose a frequency among the ones of the frequency vector. Then at first the positive sequence is selected.
3. The file containing the measurements under analysis is imported, and only the data in a chosen time period is selected and saved. The considered time range is 10 periods of the injected signal, and therefore must be calculated for each frequency.
4. The three-phase currents and voltages are transformed to the  $(\alpha, \beta)$  frame through an amplitude invariant Clarke transformation function.
5. The considered injected frequency is such only in the  $(d, q)$  frame, the  $(\alpha, \beta)$  currents and voltages are transformed with a rotation transformation function. Fig. 3.6 shows voltages and currents after the rotation transformation when a 1 Hz voltage perturbation is injected. The reader should note that the rotation

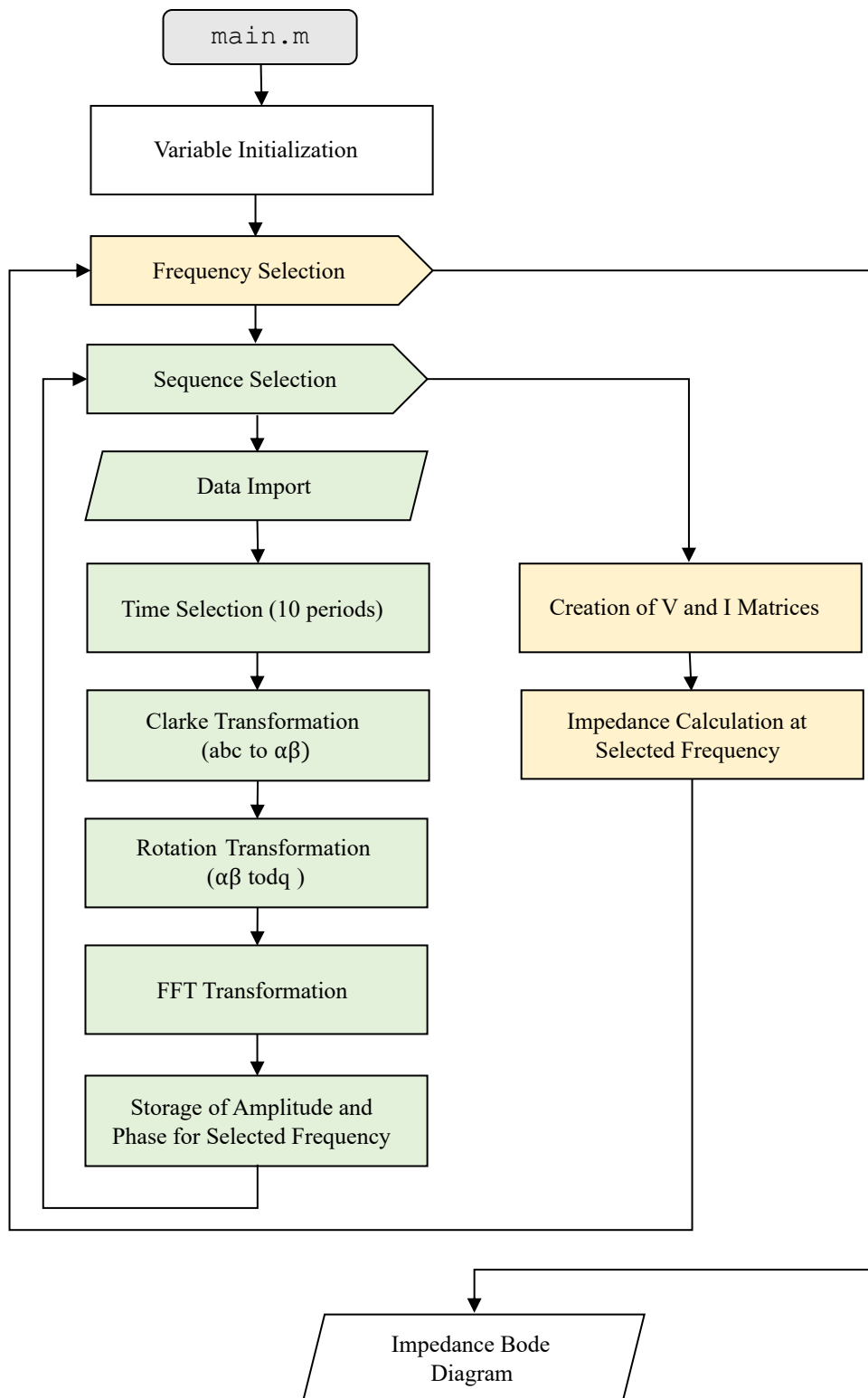


Figure 3.5: Flow Chart of the Voltage Injection Algorithm.

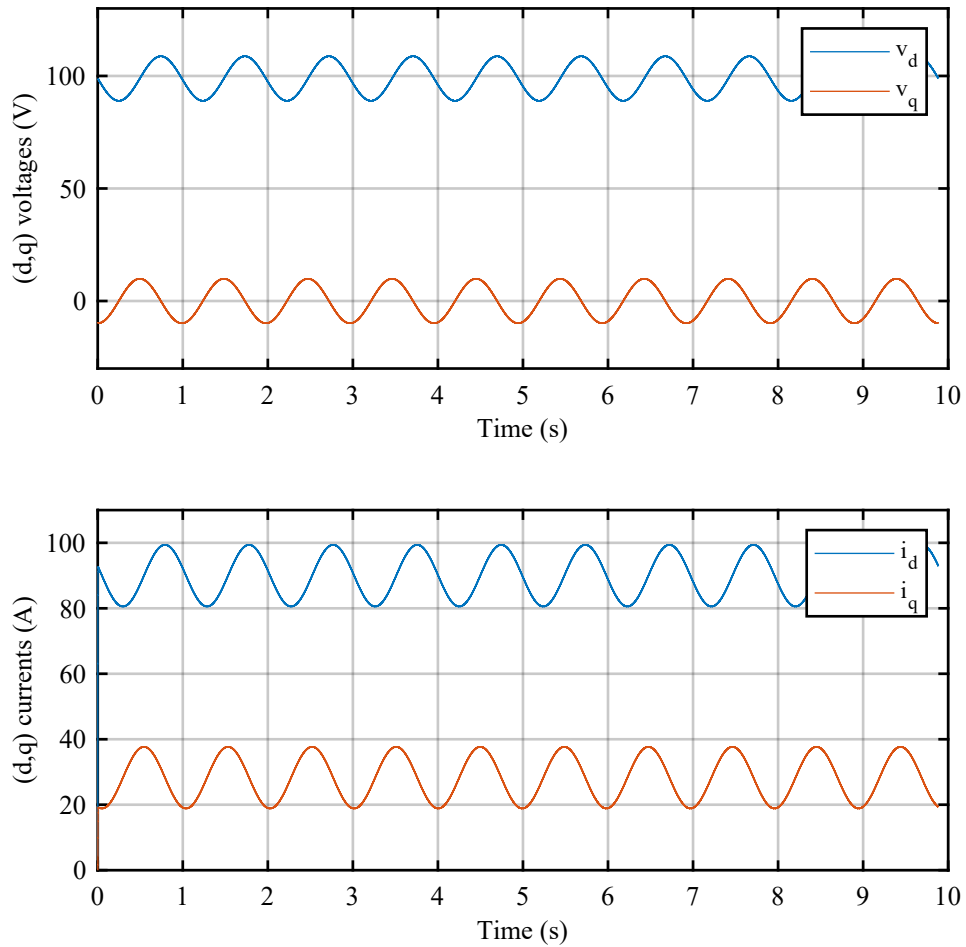


Figure 3.6: Voltages and currents in the  $(d, q)$  frame with a voltage perturbation at 1 Hz.

angle  $\theta$  cannot be directly computed through an arctangent function from the  $(\alpha, \beta)$  measured voltages because of the overlapped perturbation signal. Therefore two possibilities are available. The most effective and most simple to use is to save from simulation the electric angle that is used for generating the signal of the reference fundamental voltage and that is obtained through integration of the chosen fundamental frequency. This is the method used in the simulation. However, this is not possible when the fundamental sequence reference is not known, *e.g.* when the fundamental voltage is not generated

from the the voltage injection block or when in a real experimentation the injection is obtained from a voltage controlled power converter connected to the grid. In these cases, the measured voltage must be filtered with a second order narrow bandpass filter tuned on the grid frequency (*i.e.* that emulates the functioning of a SOGI).

6. An FFT is performed on the  $(d, q)$  voltages and currents in order to isolate the perturbation frequency. The phase and amplitude of the perturbation currents and voltages are transformed into complex numbers  $I_{d,1}$ ,  $I_{q,1}$ ,  $V_{d,1}$ ,  $V_{q,1}$  and therefore saved. One could complain that for a passive circuit with no other frequency other than the fundamental and the injected one, as the simulated circuit is, a DFT would be an excessive solution. In fact, it would be sufficient to subtract the average value from the  $(d, q)$  signals and only the perturbation effect would remain. This solution, however, would not be not applicable to active circuits such as power converters, where switching harmonics cannot be neglected. Moreover, in a real experimentation measurements are affected by noise as well, and this needs to be filtered out in order to obtain a reliable measurement. Therefore an FFT analysis is mandatory.
7. Steps 3 to 6 are repeated for the negative sequence measurement at the same  $(d, q)$  frequency, and the phase and amplitude of the signals at the injection frequencies are transformed into complex numbers  $I_{d,2}$ ,  $I_{q,2}$ ,  $V_{d,2}$ ,  $V_{q,2}$  and saved.
8. With two complex voltages and currents for each of the two tests the voltage and current matrices are created. From these, the four impedances are computed as:

$$\begin{bmatrix} Z_{dd} & Z_{dq} \\ Z_{qd} & Z_{qq} \end{bmatrix} = \begin{bmatrix} V_{d,1} & V_{d,2} \\ V_{q,1} & V_{q,2} \end{bmatrix} \cdot \begin{bmatrix} I_{d,1} & I_{d,2} \\ I_{q,1} & I_{q,2} \end{bmatrix}^{-1} \quad (3.18)$$

The resulting matrix contains the computed impedances for the specific injected frequency.

9. Steps 2 to 8 are repeated for every considered perturbation frequency and results are saved in a vector for each impedance

10. After every frequency has been processed, the bode diagram of the results can be obtained.

The results were then compared to the analytical transfer functions. Fig. 3.7 shows the results of a simulation with 30 different injected frequencies logarithmically spaced with a sampling at 100 kHz, which is decimated by 10 for the picture generation. The obtained results have a very low deviation from the analytical

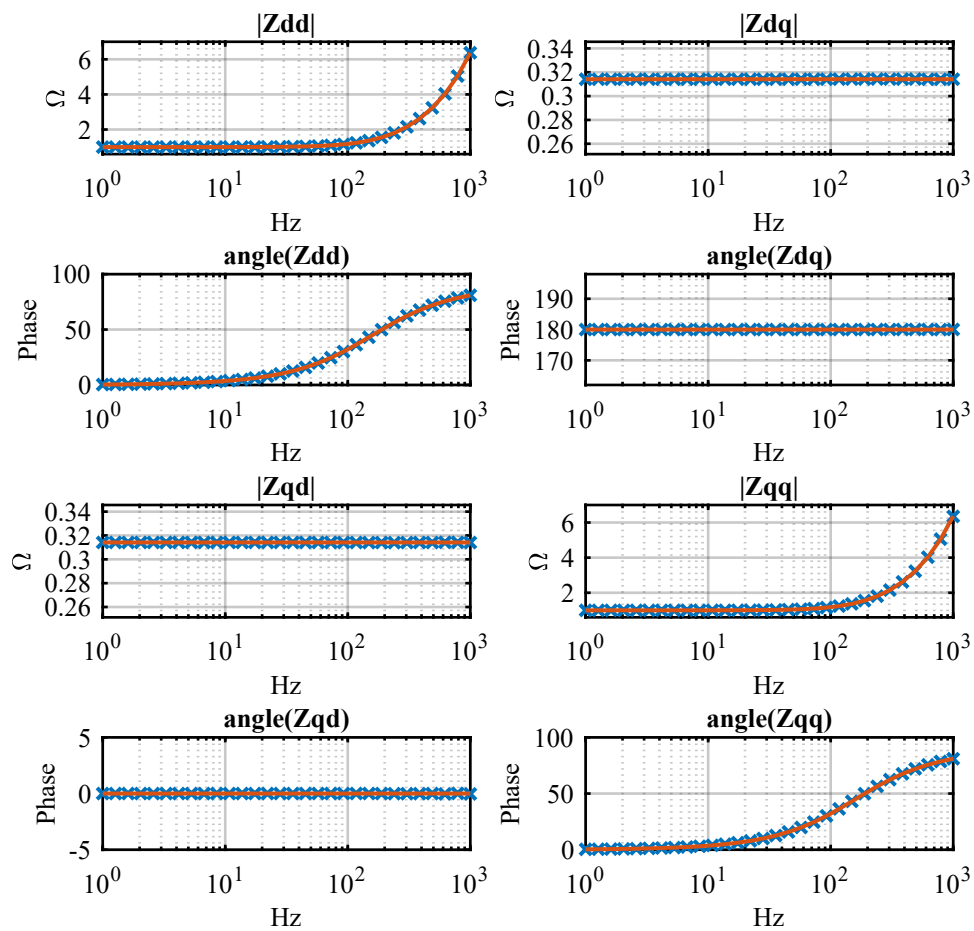
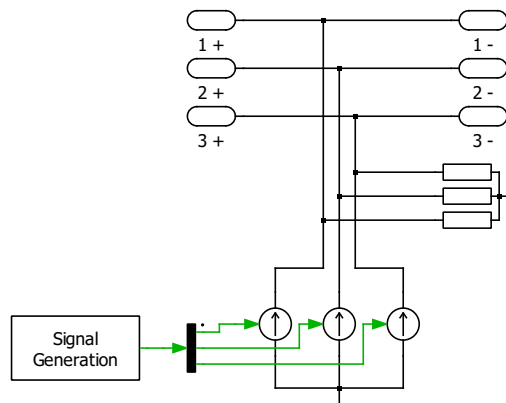


Figure 3.7: Comparison between measured points (in blue) and analytical transfer function (in orange) for a RL circuit when injecting voltage perturbations.

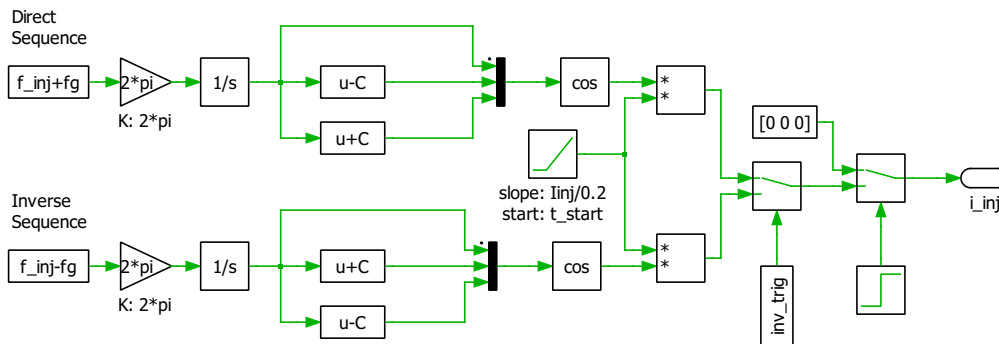
results. Therefore they are acceptable and validate the voltage injection algorithm.

### 3.5 RL Circuit Analysis Through Current Injection

The impedance of the RL circuit was then measured in another *PLECS* simulation by using a current injection as a perturbation. The adopted circuit is shown in Fig. 3.8.



(a) Subsystem used for the injection of the current perturbation.  $(1,2,3)_-$  and  $(1,2,3)_+$  are connected in series between the load and the grid.



(b) Subsystem used for the generation of the current perturbation signal.

Figure 3.8: Subsystem used for the current perturbation.

The approach is very similar to the voltage injection, but the current generator is connected in parallel with the load under test. Therefore the current will divide between the load and the grid. The division is interesting to study in order to determine the magnitude of the perturbation. A simplified single phase equivalent circuit is represented in Fig. 3.9. The grid and the load are represented with

their Thevenin equivalent, but no generator is considered since the aim is to study the division of  $I_p$ , which has a frequency  $f_{dq}$  which is generally different from the frequency of the grid equivalent voltage generator  $f_g$ .

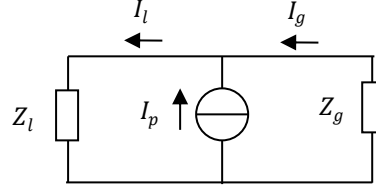


Figure 3.9: Thevenin equivalent circuit at different frequencies from the grid frequency.

As already studied by [12], the current divider can be studied as done in the following lines. For simplicity, matrices are represented through the following compact form:

$$\mathbf{I}_l = \begin{bmatrix} I_{l,d} \\ I_{l,q} \end{bmatrix} \quad \mathbf{I}_p = \begin{bmatrix} I_{p,d} \\ I_{p,q} \end{bmatrix} \quad \mathbf{I}_g = \begin{bmatrix} I_{g,d} \\ I_{g,q} \end{bmatrix}$$

$$\mathbf{V}_l = \begin{bmatrix} V_{l,d} \\ V_{l,q} \end{bmatrix} \quad \mathbf{V}_p = \begin{bmatrix} V_{p,d} \\ V_{p,q} \end{bmatrix} \quad \mathbf{V}_g = \begin{bmatrix} V_{g,d} \\ V_{g,q} \end{bmatrix} \quad \mathbf{V} = \begin{bmatrix} V_d \\ V_q \end{bmatrix}$$

$$\mathbf{Z}_l = \begin{bmatrix} Z_{l,dd} & Z_{l,dq} \\ Z_{l,qd} & Z_{l,qq} \end{bmatrix} \quad \mathbf{Z}_g = \begin{bmatrix} Z_{g,dd} & Z_{g,dq} \\ Z_{g,qd} & Z_{g,qq} \end{bmatrix}$$

The currents respect the following equation:

$$\mathbf{I}_l = \mathbf{I}_g + \mathbf{I}_p \quad (3.19)$$

While the voltages are:

$$\mathbf{V}_s = \mathbf{V}_p = \mathbf{V}_g = \mathbf{V} \quad (3.20)$$

(3.19) can be written as:

$$\mathbf{Z}_l^{-1} \cdot \mathbf{V} = \mathbf{I}_p + \mathbf{Z}_g^{-1} \cdot \mathbf{V} \quad (3.21)$$

$$\mathbf{I}_p = (\mathbf{Z}_g^{-1} + \mathbf{Z}_l^{-1}) \cdot \mathbf{V} \quad (3.22)$$

$$\mathbf{V} = [\mathbf{Z}_g^{-1} + \mathbf{Z}_l^{-1}]^{-1} \cdot \mathbf{I}_p \quad (3.23)$$

The load current is:

$$\mathbf{V}_l = \mathbf{Z}_l \cdot \mathbf{I}_l = [\mathbf{Z}_g^{-1} + \mathbf{Z}_l^{-1}]^{-1} \cdot \mathbf{I}_p \quad (3.24)$$

$$\mathbf{I}_l = \mathbf{Z}_l^{-1} \cdot [\mathbf{Z}_g^{-1} + \mathbf{Z}_l^{-1}]^{-1} \cdot \mathbf{I}_p \quad (3.25)$$

Similarly, for the perturbation current that goes into the grid:

$$\mathbf{V}_g = -\mathbf{Z}_g \cdot \mathbf{I}_g = [\mathbf{Z}_g^{-1} + \mathbf{Z}_l^{-1}]^{-1} \cdot \mathbf{I}_p \quad (3.26)$$

$$\mathbf{I}_g = -\mathbf{Z}_g^{-1} \cdot [\mathbf{Z}_g^{-1} + \mathbf{Z}_l^{-1}]^{-1} \cdot \mathbf{I}_p \quad (3.27)$$

If an estimate of the grid and load impedance is available it is possible to estimate the magnitude of  $\mathbf{I}_p$  from (3.25) in order to obtain a reasonable  $\mathbf{I}_l$ :

$$\mathbf{I}_p = \mathbf{Z}_l \cdot (\mathbf{Z}_g^{-1} + \mathbf{Z}_l^{-1}) \cdot \mathbf{I}_l \quad (3.28)$$

It is also interesting to consider:

$$\mathbf{Z}_l \cdot \mathbf{I}_l = -\mathbf{Z}_g \cdot \mathbf{I}_g \quad (3.29)$$

$$\mathbf{I}_l = -\mathbf{Z}_l^{-1} \cdot \mathbf{Z}_g \cdot \mathbf{I}_g \quad (3.30)$$

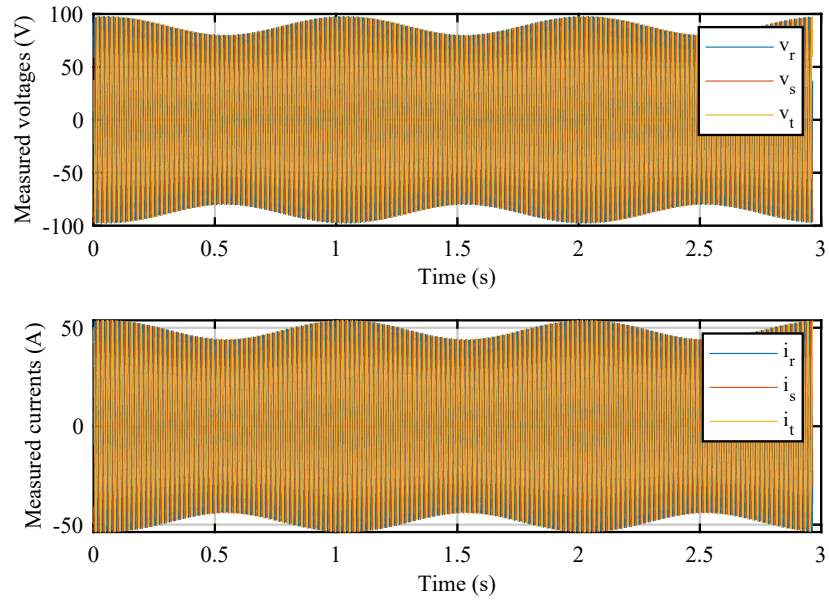
If the grid impedance is much lower than the inverter impedance it will be difficult to measure the current perturbation on the load side.

### 3.5.1 PLECS Implementation

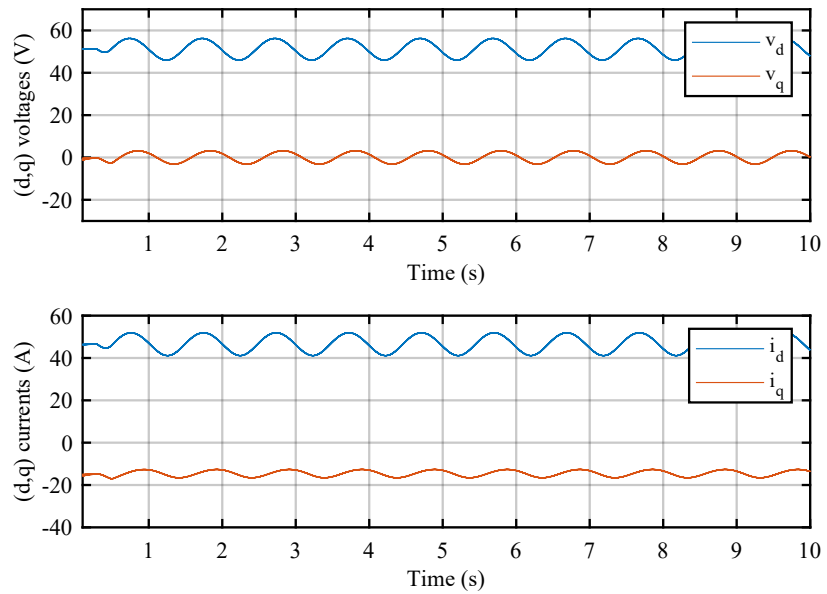
The injection block considers three current generators connected in parallel with the load and the grid. The signal generation subsystem is almost identical to the one used for the voltage injection simulation, but differently from this last case there is no possibility to generate the fundamental voltage. Moreover, at the start of the injection, the peak of the perturbation grows with a ramp that lasts 200 ms, for compatibility with the inductor dynamics.

Fig. 3.10a shows a fragment of three phase currents and voltages when a 1 Hz sinusoidal current perturbation with 10 A amplitude is injected, while Fig. 3.10b shows the perturbation in the  $(d, q)$  reference frame.

Differently from the voltage injection simulation, grid voltage position is not known. Therefore an angle estimator must be used. Moreover, this must be able



(a) Three phase voltages and currents with a current perturbation at 1 Hz.



(b) Voltages and currents in the  $(d, q)$  frame with a current perturbation at 1 Hz.

Figure 3.10: Voltages and currents with a current perturbation at 1 Hz.

to reject the voltage perturbation and isolates the fundamental component. This is realized with a SOGI that filters out frequencies different from the fundamental and passes the results to an `atan2` function that calculates the angle.

The measured three phase currents and voltages are processed with the same MATLAB script used for the voltage injection. The results are shown in Fig. 3.11.

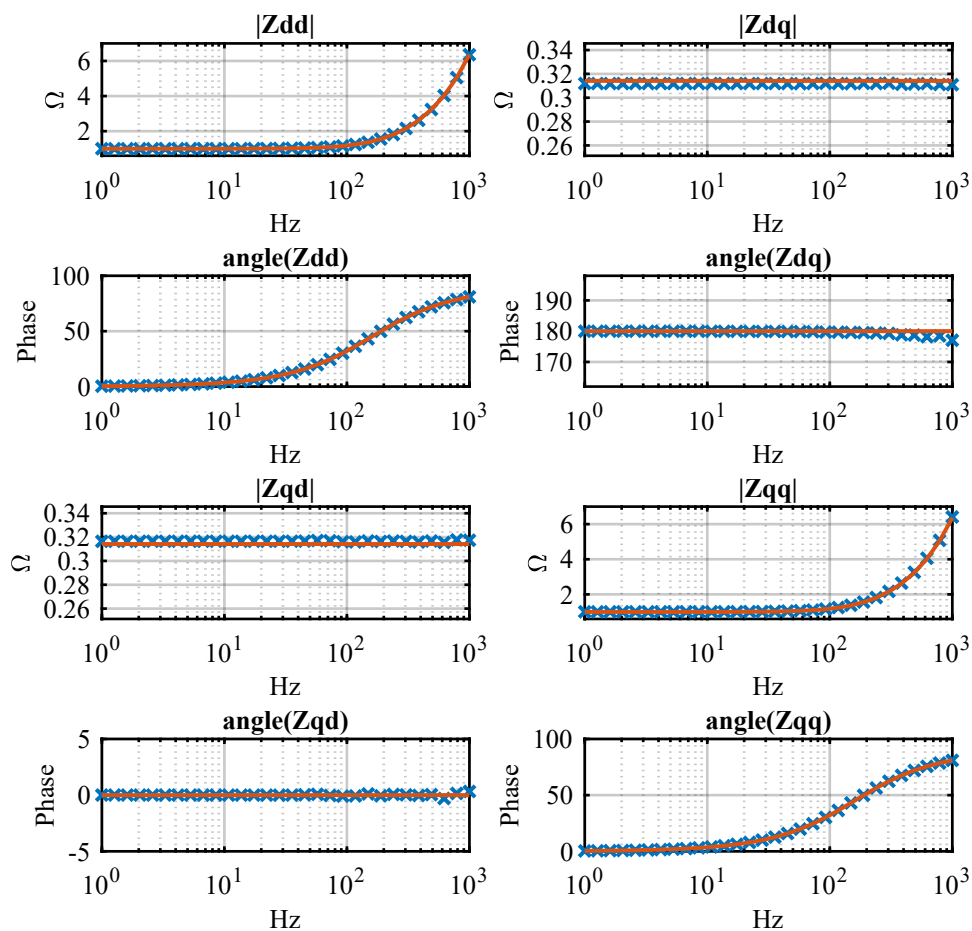


Figure 3.11: Comparison between measured points (in blue) and analytical transfer function (in orange) for a RL circuit when injecting current perturbations.

As the reader can notice, the results are very similar to the analytically obtained impedances. However, there is a small deviation at high frequencies. This is caused

by the reconstructed voltage angle, which is more distorted at high frequencies and therefore transmits this distortion to the  $(d, q)$  data. In general with signal injection techniques, the higher the injected frequency is, the lower the accuracy on the results is. For measurements on power converters this inaccuracy is not due to the inaccurate voltage angle, which is obtained from the PLL with an excellent level of precision. The major cause of this phenomenon is the lower number of samples that are available at high injected frequencies. This is particularly true when the sampling is done directly by the converter at ISR update frequency. Therefore, if an external data acquisition unit is available, it is best to sample at a higher frequency than the converter sampling frequency.

## 3.6 PLECS Simulation of Voltage Injection

After the voltage injection block and the MATLAB signal processing script had been validated through the *PLECS* simulation, they were applied to a converter simulation which considered the system that was described and sized in Chapter 2. Various cases were considered, in order to study the effect of every part of the control and compare the results with the theoretical curves:

- At first a simulation was done with the current control only. DC voltage came from an ideal generator and no SOGI was applied to the PLL input voltages. The results were compared to a theoretical calculation, according to [26].
- Then a simulation was done with the effect of a voltage control as well. These results were compared to a theoretical calculation as well.
- At last a simulation was done with DC voltage fed by a Boost converter, as in the available experimental set-up.

The considered PLECS equivalent of the electrical circuit is shown in Fig. 3.12.

The voltage injection block is placed between the grid equivalent circuit and the converter, while sampling is done at the LCL filter capacitor. The choice of the injection block positioning and the point of sampling was done to reflect the structure of the real converter that would have been used for the experiment.

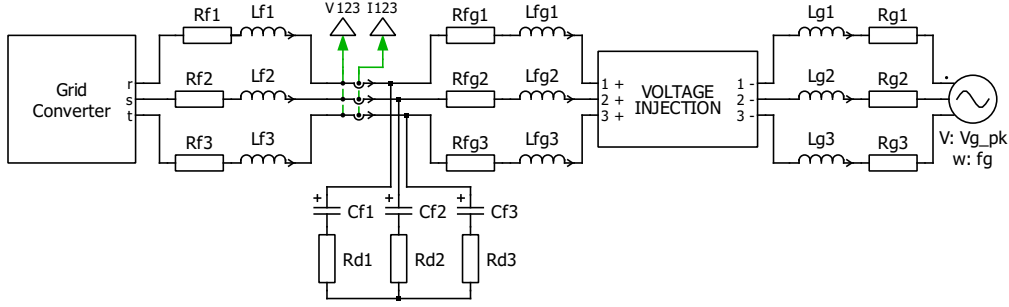


Figure 3.12: PLECS equivalent of a voltage injection test for a grid converter.

### 3.6.1 Inverter Average Value Equivalent Model

The process of multiple simulations is computationally quite heavy and requires many hours to complete. In order to reduce the computational burden, a PLECS average value equivalent circuit of the converter was made. This choice does not affect the quality of the results, since the obtained models are valid at frequencies that are lower than the switching one. A first version without the DC/DC stage was initially considered, with an ideal DC load. This model is shown in Fig. 3.13.

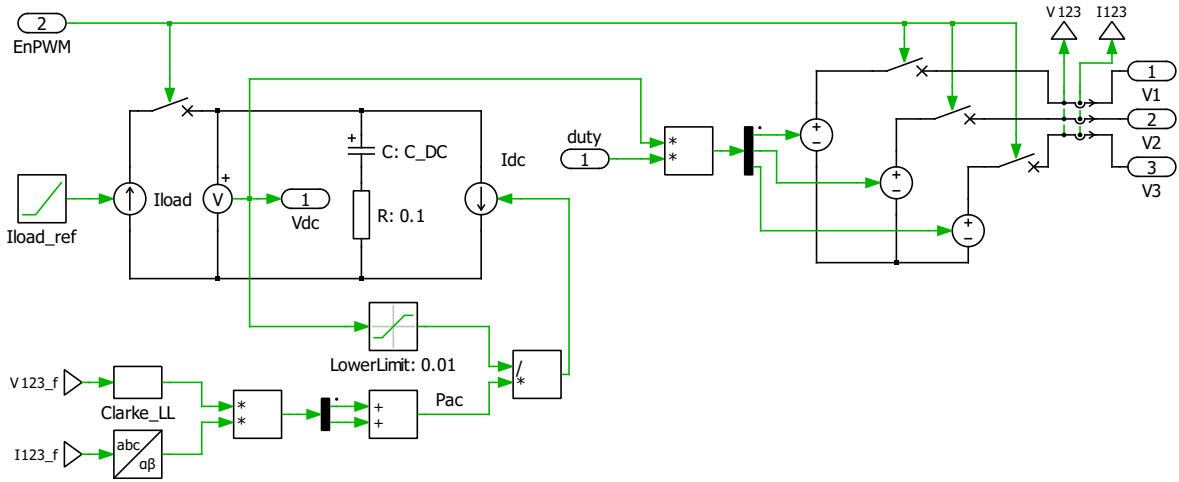


Figure 3.13: PLECS average value equivalent circuit of the three-phase inverter and DC imposed current.

The converter output phase voltage is given by the product of the DC-link voltage and the duty cycles computed by the control. DC-side current coming from the inverter is calculated by dividing the inverter output power  $P_{AC}$ , calculated in

the  $(\alpha, \beta)$  frame, by the DC-link voltage:

$$P_{out} = \frac{3}{2} \cdot (v_\alpha \cdot i_\alpha + v_\beta \cdot i_\beta) = v_{DC} \cdot i_{DC} \quad (3.31)$$

$$i_{DC} = \frac{3}{2} \cdot \frac{v_\alpha \cdot i_\alpha + v_\beta \cdot i_\beta}{v_{DC}} \quad (3.32)$$

DC load current is considered ideal and feded through an ideal current generator.

For simulations that considered only current control, the input for controlled voltage generators was simply obtained by multiplying the duty cycles by a constant, equal to the chosen DC-link voltage.

### 3.6.2 Simulation Results

The results of the various simulations are shown and commented in this section.

#### Equivalent admittance with Current Loop

The first *PLECS* simulation that was carried out considered only an output current control loop, while the DC-link was approximated to an ideal generator. This was done in order not to take into account the effect of the voltage control on the equivalent admittance. Therefore the result is produced by the dynamic behaviour of the PLL, current control and output filter. The converter works as an active rectifier and absorbs 10 A on the  $d$ -axis, while  $I_q$  is controlled to zero. The equivalent admittance results are shown in Fig. 3.14.

As the reader can notice, the correspondence of the measurement with the theoretical result is very high. The only noticeable difference occurs at very low frequencies on the  $Y_{dq}$  mutual admittance. This difference can be attributed to the very low magnitude of the current perturbation responses at low frequencies. For instance, the current response amplitude when a voltage perturbation of 2 Hz is injected is around 100 mA.

The inaccuracy at very low frequencies is common in technical literature and can be neglected, since instability problems are more probable in proximity of the bandwidth frequency of the current control, which occurs at higher frequencies.

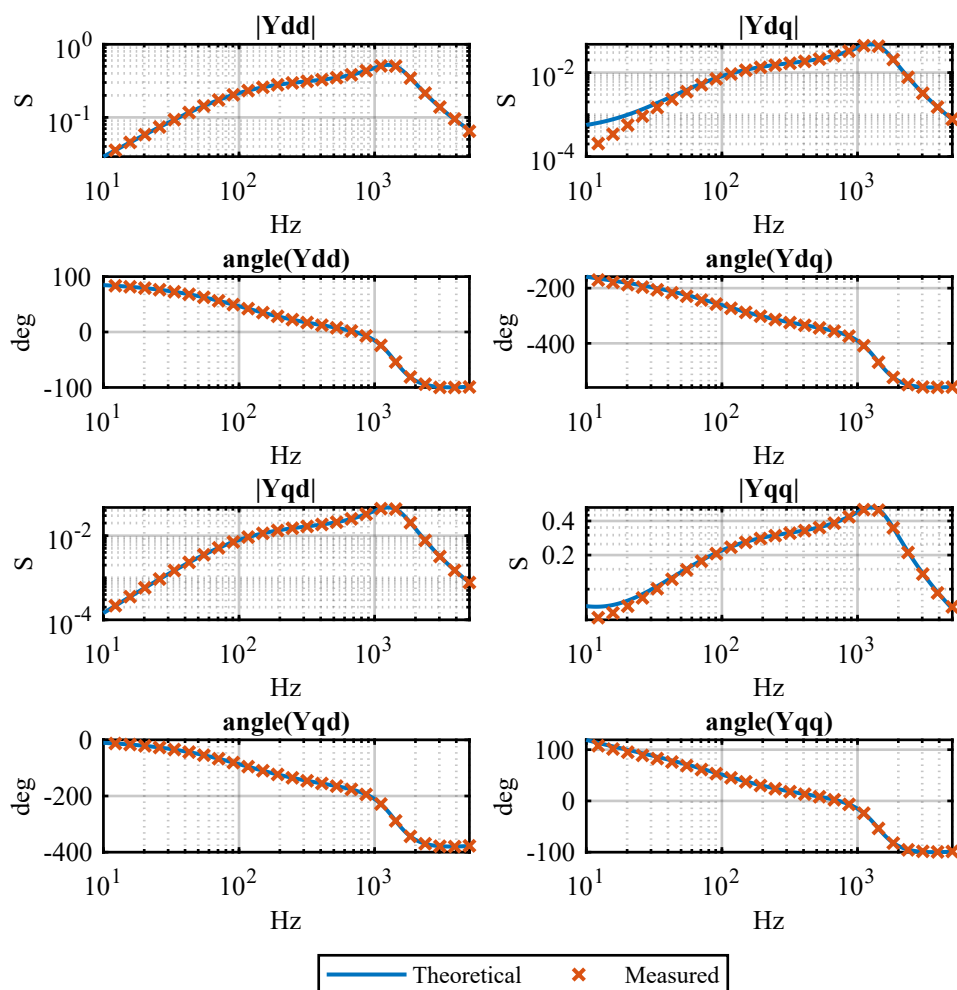


Figure 3.14: Comparison between the theoretical calculation and the measured admittance when considering a simulation with only current loop and  $I_d = 10A$  and  $I_q = 0A$  in rectifier mode.

### Equivalent admittance with DC Voltage Loop

Another simulation that was accomplished considered the effect of the DC-link voltage control as well. Analogously to the results shown in Fig. 3.14, in this simulation converter works as an active rectifier as well, with  $I_d = 10A$  and  $I_q = 10A$ . The obtained equivalent admittances are shown in Fig. 3.15.

The reader must consider that the disturbance that occurs at around 100 Hz in the theoretical impedance is an issue due to the inversion of the matrices required

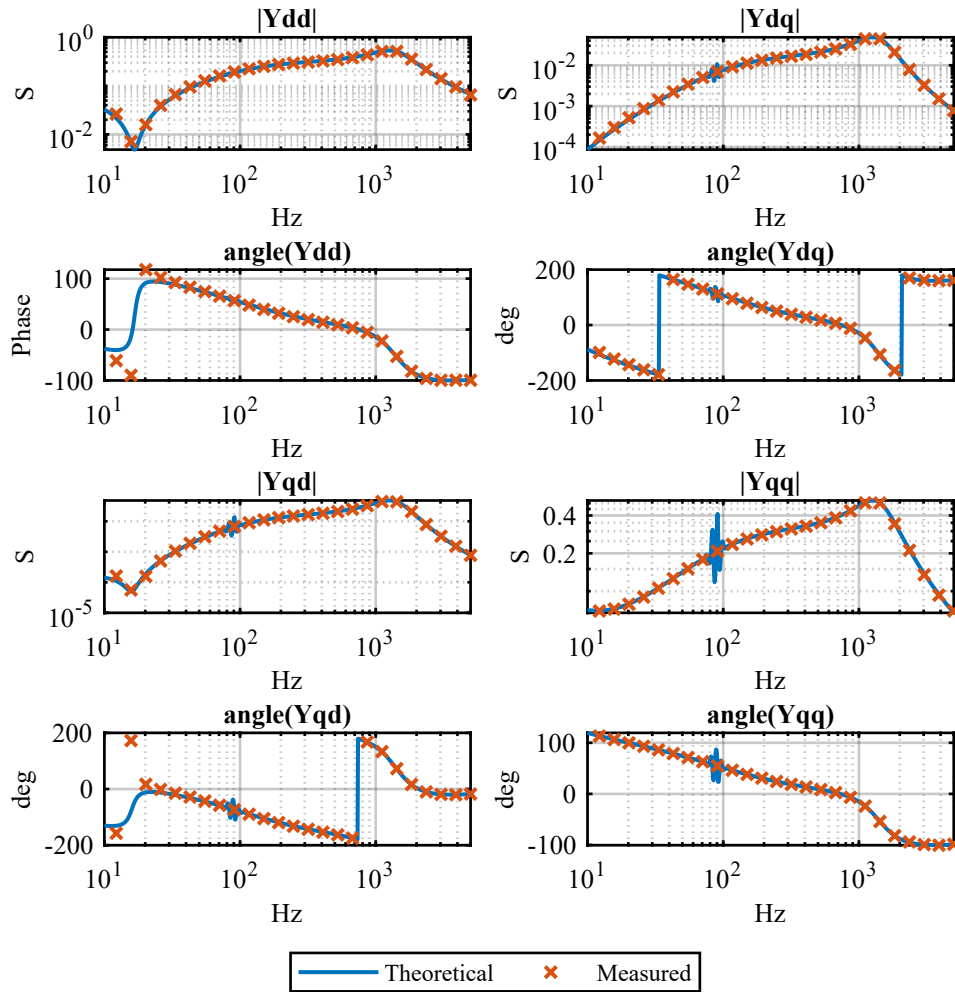


Figure 3.15: Comparison between the theoretical calculation and the measured admittance when considering a simulation with voltage and current control with  $I_d = 10A$  and  $I_q = 0A$ . The theoretical calculation does not consider a decoupling term on the output of the current controller.

for the analytical calculation, and should not be considered. When a decoupling term on the output of the current controller is added to the theoretical calculation, the inaccuracies due to this inversion become negligible. This can be observed in Fig. 3.16, where the theoretical solution considers a feed-forward. As the reader can notice, while the disturbance has disappeared the measured admittances are slightly shifted from the theoretical ones. This difference is due to the fact that in

simulations no feed-forward was considered.

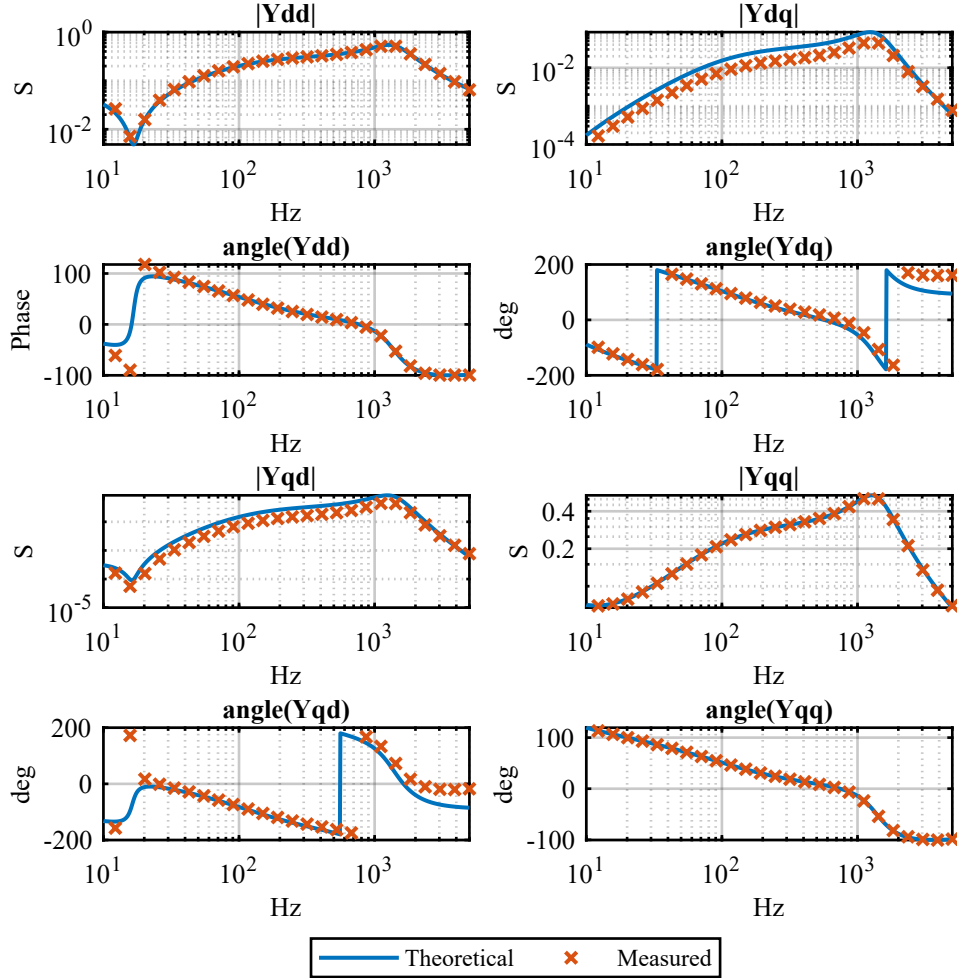


Figure 3.16: Comparison between the theoretical calculation and the measured admittance when considering a simulation with voltage and current control with  $I_d = 10A$  and  $I_q = 0A$ . The theoretical calculation considers a decoupling term on the output of the current controller.

### Equivalent admittance with Two-Stage Converter

A third simulation considered the inverter fed by a step-up DC/DC converter. The equivalent admittance results are shown in Fig. 3.17. Since no theoretical solution was available, the comparison was made with the equivalent admittance obtained

with the only output current and DC-link voltage loops. Both admittances were computed considering the converter working as an active rectifier as well, with  $I_d = 10A$  and  $I_q = 10A$ . As conceivable, the two-stage configuration is more sensitive to disturbances. However this occurs most at low frequencies, while at high frequencies the results are quite similar, depending more on the hardware components rather than on the control.

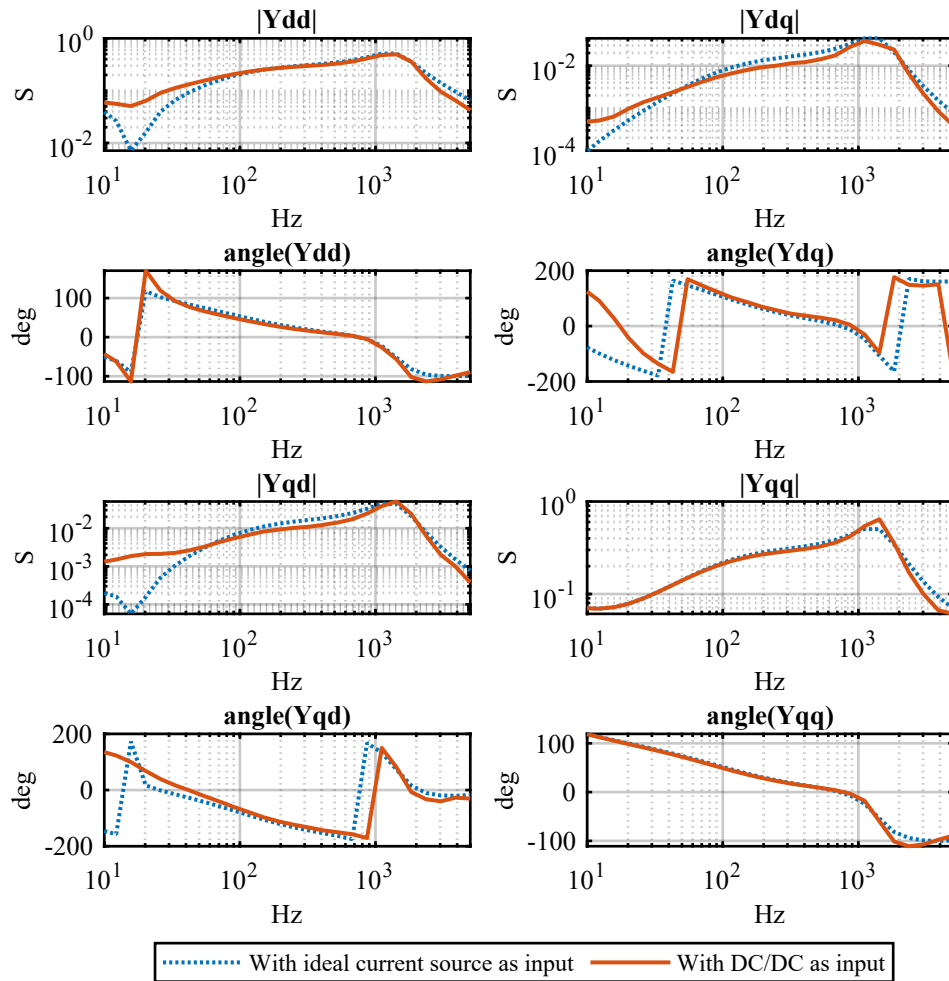


Figure 3.17: Comparison between the equivalent admittance of a two-stage converter and the one of a single stage converter with DC voltage loop and AC current loop. Both solutions were computed considering a rectifier operation with  $I_d = 10A$  and  $I_q = 0A$

## 3.7 Experimental Validation of Voltage Injection

After the injection methods were validated through simulations, the signal perturbation was implemented on a real converter.

The perturbation was a voltage injection since there was no available converter apart from the one under test, thus it was not possible to use a secondary converter for current injection. On the contrary, voltage injection could be performed directly by the grid simulator that was used to model the grid.

The grid simulator was used as a signal amplifier, where the input signal came from a real-time simulator. This could run a *PLECS* model in real time and output a signal through a physical analog output port.

Before performing the tests on the converter, the experimental setup was tested on an RL circuit in order to verify the correct functioning of the data acquisition and data processing.

### 3.7.1 Description of the Experimental Setup with an RL Circuit

The perturbation signals were generated by a *PLECS RT Box* real-time simulator (Fig. 3.18a) running a *PLECS* model. The output of this model was sent through an analog output port to a *REGATRON TopCon TC.ACS* full 4-quadrants grid simulator (Fig. 3.18b), that was set to work as an amplifier. The power outputs of the grid simulator were connected to a three phase RL load (Fig. 3.18c). The data acquisition was done through a *HBM Genesis HighSpeed 1-GEN7tA-2* data acquisition system (Fig. 3.18d), which was capable to perform most of the post processing operations. The acquisition start and stop of the HBM was controlled with triggers generated from the RT Box. A block diagram of the experimental setup is shown in Fig. 3.19.

#### Real-Time Simulator

The model that was loaded on the real time simulator is shown in Fig. 3.20.

As the reader can notice, six output signals are generated. These are connected to analog output ports, as visible in Fig. 3.18a. The  $V_{abc}$  output is the reference

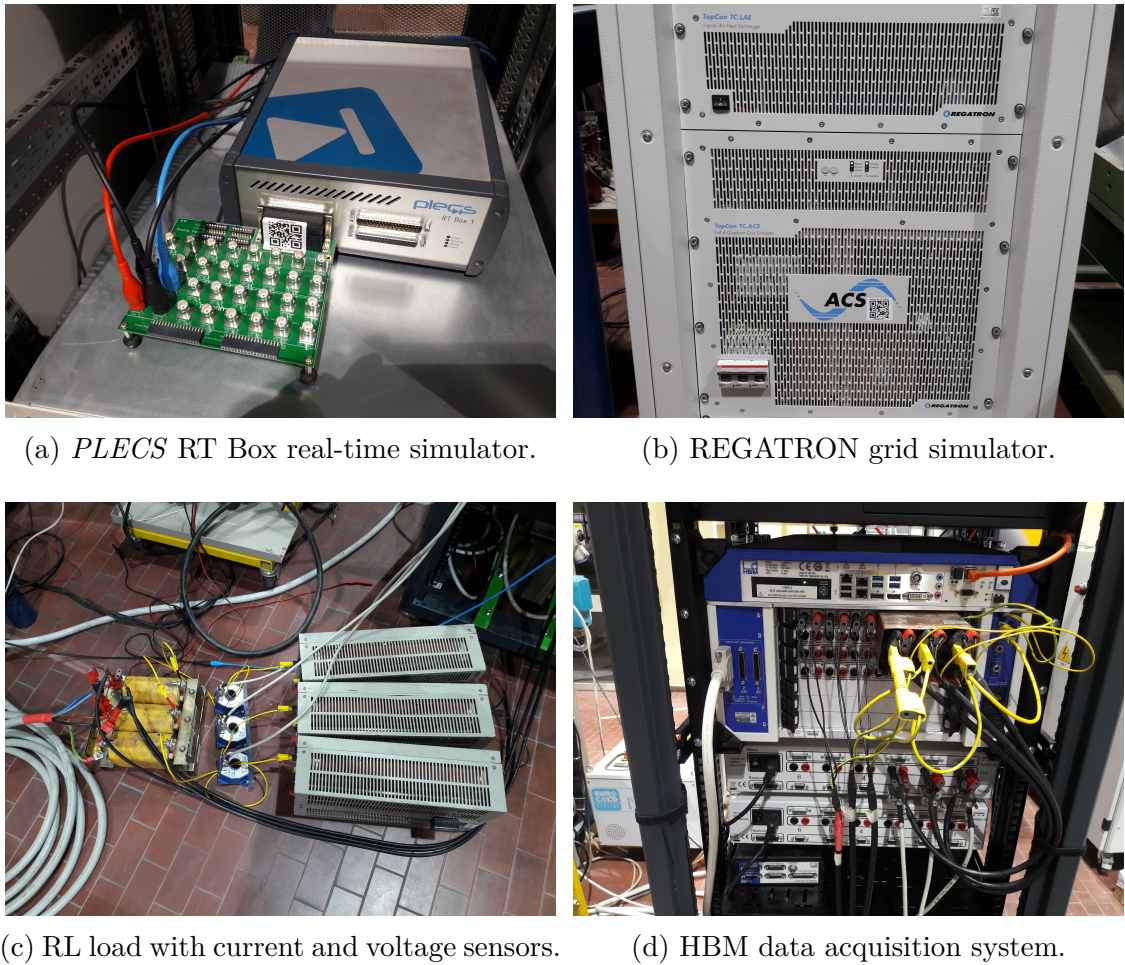


Figure 3.18: Experimental setup components.

voltage for the grid emulator, while `TriggerStart` and `TriggerStop` are connected with the data acquisition system and trigger the start and stop of the measurements. The two outputs `SinTheta` and `CosTheta` output the sine and cosine of the fundamental voltage and are used to rotate the currents and voltages in the  $(d, q)$  frame in the data acquisition system. The output of these signals is extremely useful in the rotation, since it is difficult to estimate the angle of the fundamental when the perturbation signal is overlapped. The "Signal Generation" block is equivalent to the one already described in 3.4.1. However, in this case the perturbation frequency is given as an input by a C-Script (contained in the "Frequency Selector" subsystem) which automatically performs a sweep of the selected frequencies and controls the start and stop of the acquisitions. The logic of the frequency selection

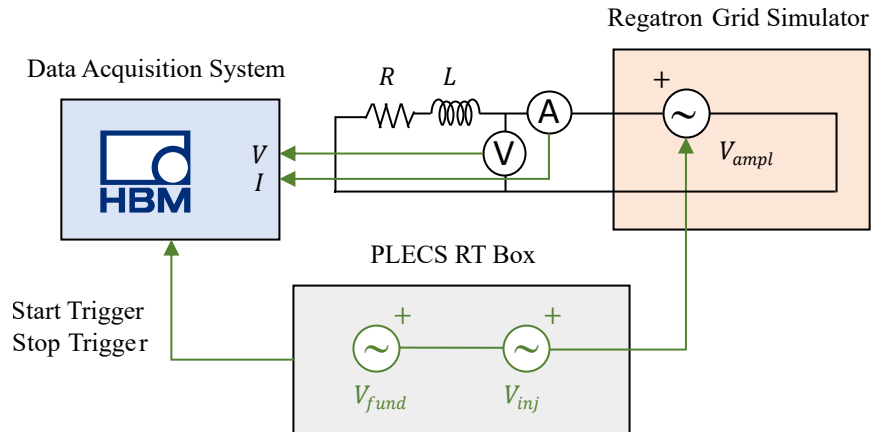
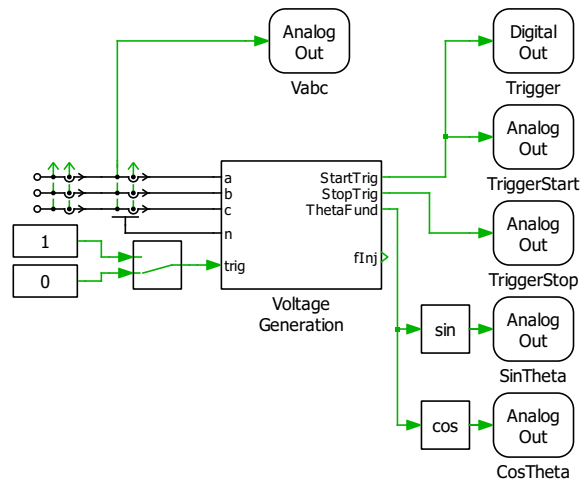


Figure 3.19: Single-line block diagram of the experimental setup.

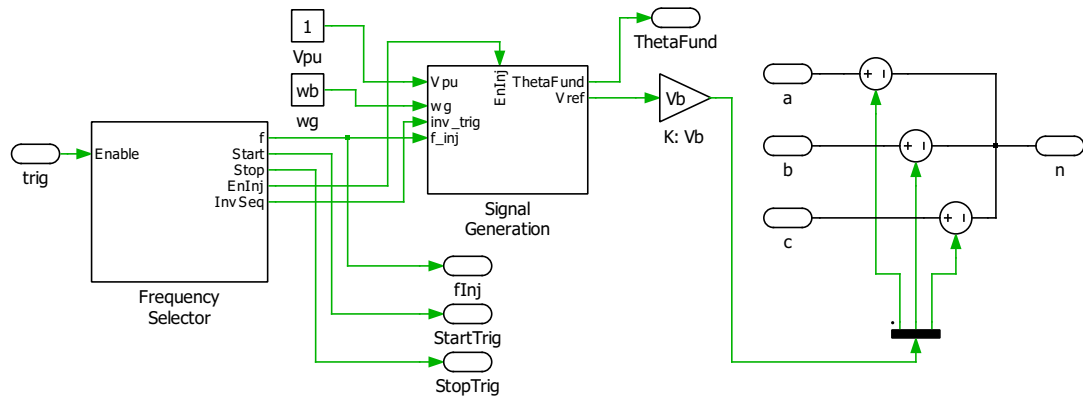
script is shown in Fig. 3.21. The basic idea is the same that was behind the Octave script that was used for PLECS simulations.

There are, however, some differences. The frequency selection script is also responsible for controlling the acquisitions of the Data Acquisition System through an acquisition start trigger and an acquisition stop trigger. The time for which each injection is performed  $T_{inj}$  is calculated as in simulations, *i.e.* either 20 periods of the perturbation signal saturated to a minimum time of 1 second. However, a fixed time  $T_{blank}$  is also considered at the start of each frequency injection. During this period no injection is performed and no acquisition is done. When  $T_{blank}$  has passed, the acquisition start trigger is set to its *HIGH* value. After  $T_{inj}$  has passed from the start of the acquisition the injection stops and the acquisition stop trigger is set to *HIGH*. This process is repeated two times for every frequency, alternating direct and inverse sequences. At the end of every frequency contained in the frequency vector, the injection stops.

Through this script the test is fully automated and requires no intervention until the end. Each frequency is saved in a MATLAB-compatible file format that will be automatically picked up and processed by the MATLAB signal injection processing algorithm described in Section 3.4.2.



(a) General block diagram with output signals.



(b) "Voltage Generation" subsystem.

Figure 3.20: *PLECS* RT Box model

## Experimental Results

A test was performed with 35 logarithmically spaced frequencies from 1 to 1000 Hz. The results are shown in 3.22.

As the reader can notice, results at low frequencies are quite accurate, but start to deviate from the theoretical RL solution as frequencies increase. The explanation of this phenomenon can be obtained if parasitic capacitances are considered. In fact, the considered resistor is actually a wire-wound rheostat. The capacitance between coils is negligible at low frequencies, but starts to be influential as the frequency rises. This phenomenon produces resonances that modify the high frequency results

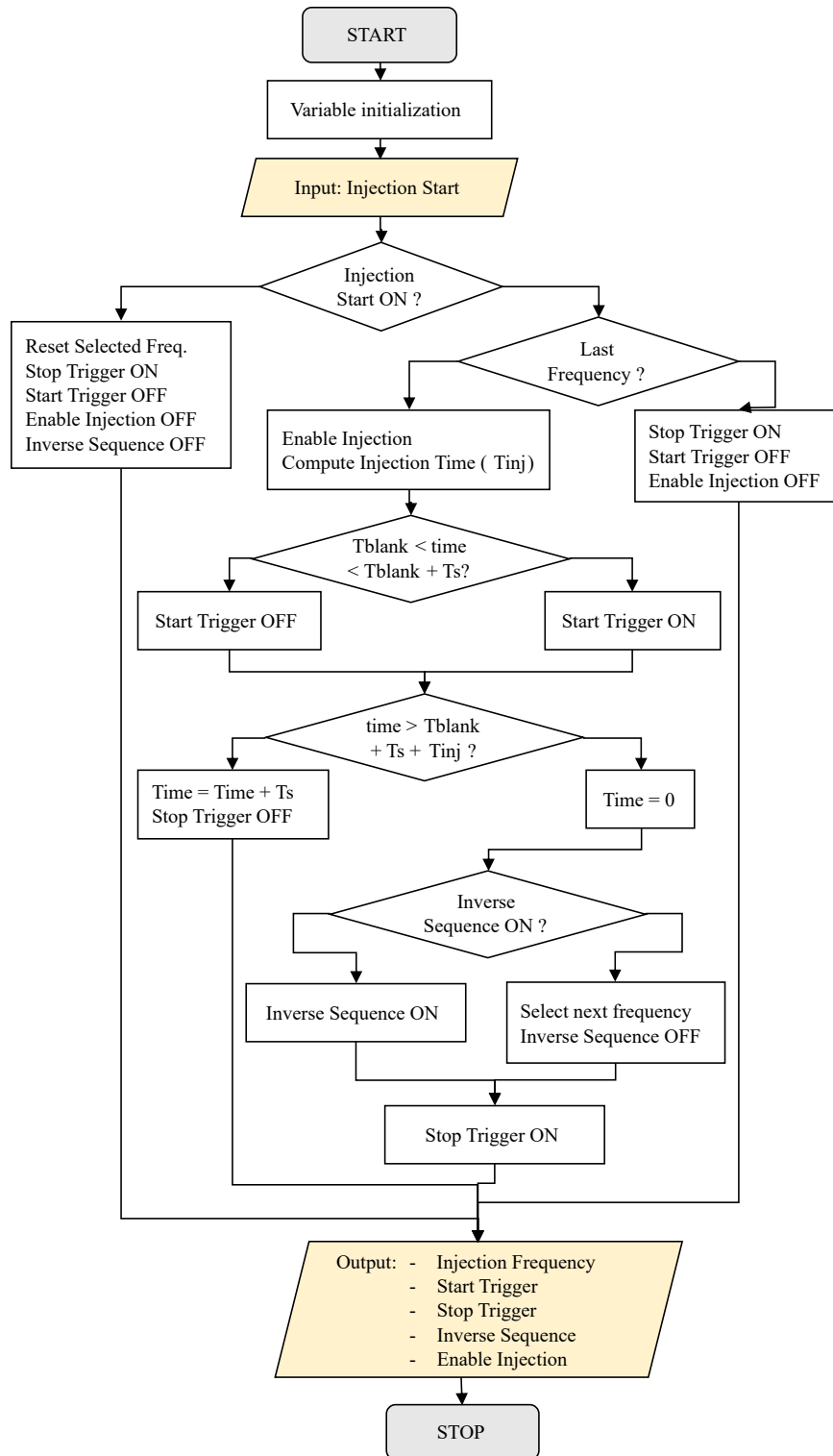


Figure 3.21: Flow chart of the frequency selection script.

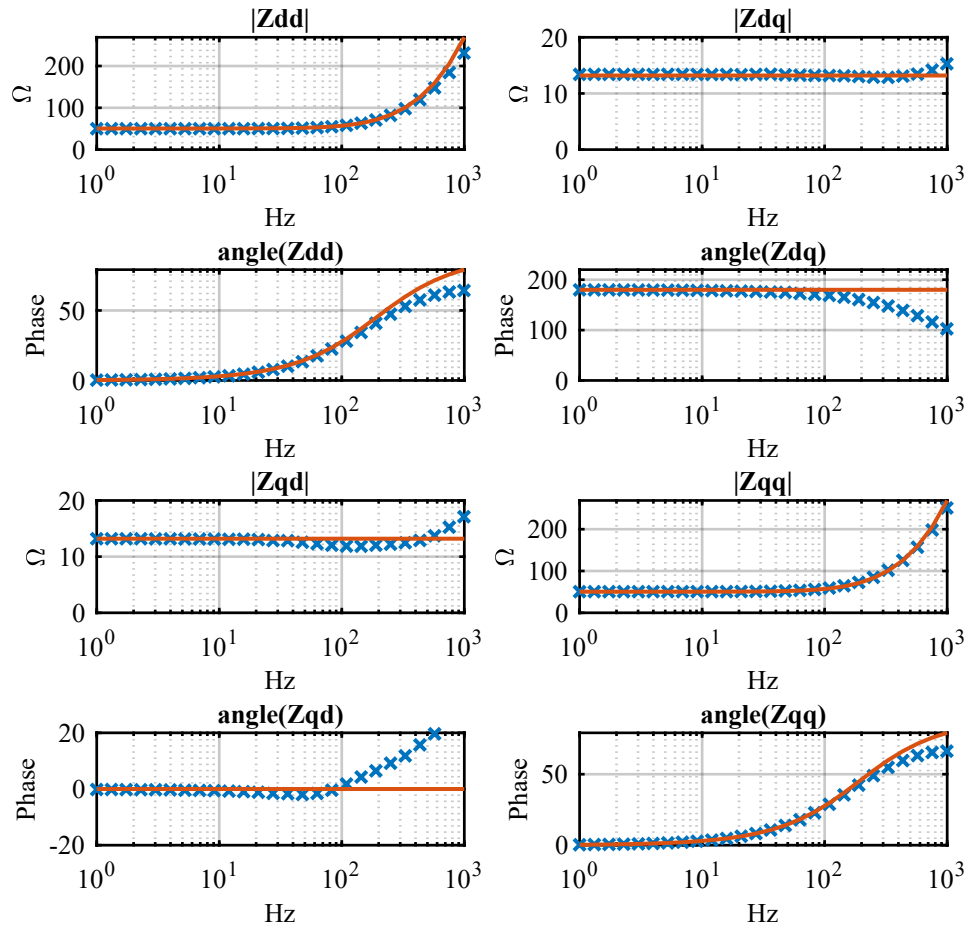


Figure 3.22: Experimental results of the measurements of the RL circuit through voltage injection.

of the measurements.

### 3.7.2 Experimental Measurement with Grid-Connected Converter

After the voltage injection method was tested through simulations and the experimental set-up was first applied to a passive circuit, an experimental measurement of the converter admittance was carried out with the voltage perturbation injection

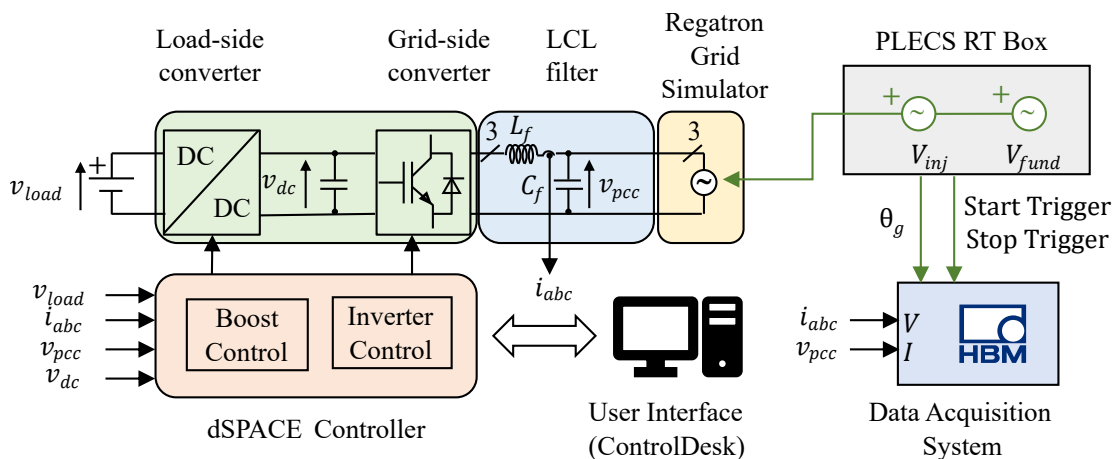
method.

Fig. 3.23a shows a block diagram of the experimental set-up that was used, while Fig. 3.23b and 3.23c show the converter that was used and the output LC filter. Table 3.1 shows the utilized converter values. The converter under test is provided with an LCL filter, but the grid side inductor was bypassed in order to consider a system as close as possible as the theoretical system considered in [26], which analytically calculates the equivalent admittance of a single-stage AC/DC converter with output current control, DC voltage control and output RL filter.

<b>Grid electrical data</b>		
Grid RMS phase voltage	$V_{g,RMS}$	120 V
Grid frequency	$f_g$	50 Hz
<b>Output LC filter</b>		
Output inductor	$L_f$	545 $\mu$ H
Output capacitor	$C_f$	22 $\mu$ F
<b>DC-link</b>		
DC-link capacitor	$C_{DC}$	1.8 mF
DC-link set point	$V_{DC,ref}$	370 V
<b>DC/DC Converter</b>		
DC/DC input inductor	$L_{DC}$	10 mH
Input DC voltage	$V_{load}$	300 V
Input DC current	$I_{load}$	8.5 A
<b>Converter switching data</b>		
ISR update frequency	$f_{sw}$	10 kHz
ISR timing	$T_{sw}$	100 $\mu$ s
<b>Maximum ratings</b>		
Maximum output power	$S_{AC,max}$	15 kVA

Table 3.1: Converter values.

The considered system in the experimental set-up therefore presents some differences from the theoretically analysed one, which consist in the presence of a



(a) Experimental Measurement set-up.



(b) DC/AC grid-connected converter. The input filter is placed on the opposite side.

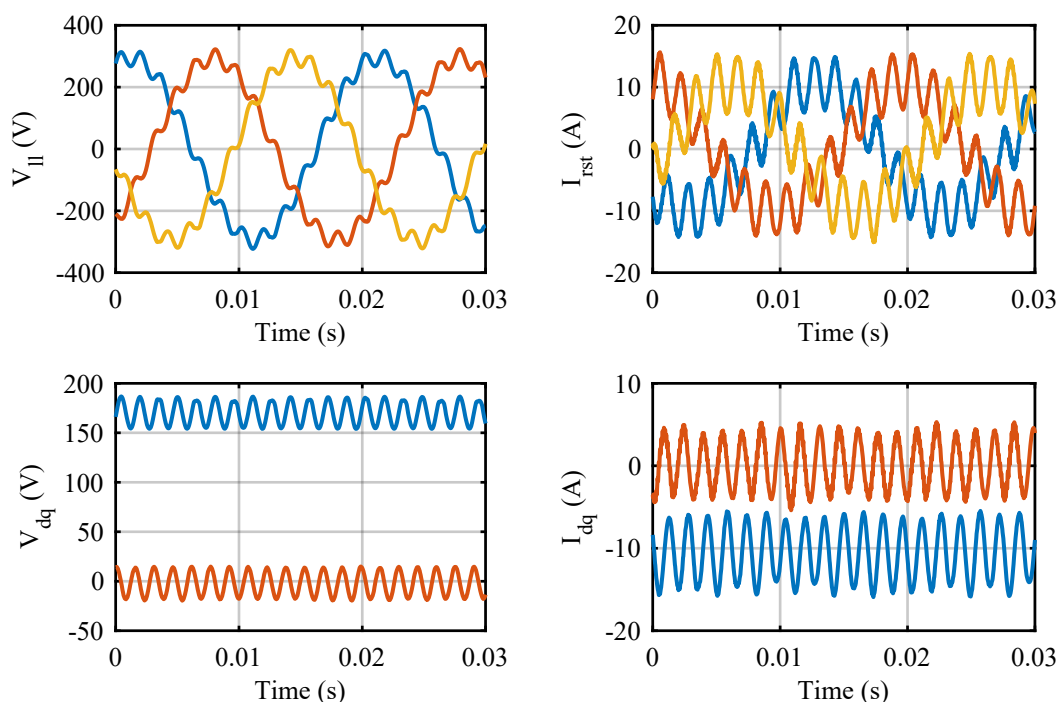


(c) Converter LCL filter. The grid is directly connected to the inductor near the converter, bypassing one inductor bank.

Figure 3.23: Converter experimental set-up pictures.

capacitor bank in the output filter and, most importantly, a DC/DC step-up converter stage that controls the DC current that inputs (or outputs) the DC side of the AC/DC converter. A comparison between the measured and theoretical admittances is nevertheless still applicable, the major contribution to the converter dynamic comes from the AC/DC stage.

An example of the voltages and currents that were measured in the experimental set-up is shown in Fig. 3.24, for a positive-sequence voltage injection at  $f_{inj} = 650$  Hz and  $I_{dc} = 8.5$  A (absorbed).



(a) PCC line voltages in the three-phase reference frame (upper image) and in the  $(d, q)$  reference frame (lower image). (b) Output currents in the three-phase reference frame (upper image) and in the  $(d, q)$  reference frame (lower image).

Figure 3.24: Experimental Measurement of PCC line voltages and output currents in the three-phase and in the  $(d, q)$  reference frame.

The equivalent admittance results for the experimental measurement are shown in Fig. 3.25 for a test with an absorbed  $I_{dc} = 8.5$  A. Some considerations can be done:

- The correspondence between measured and theoretical self-admittances  $Y_{dd}$  and  $Y_{qq}$  is very high.
- The mutual-admittances present good correspondence at frequencies higher than 50-100 Hz, but present a difference at low frequencies. This can be attributed to two causes:
  - The considered system under test is not the same as the theoretical one.
  - In the comparison between single-stage and two-stage converter shown in

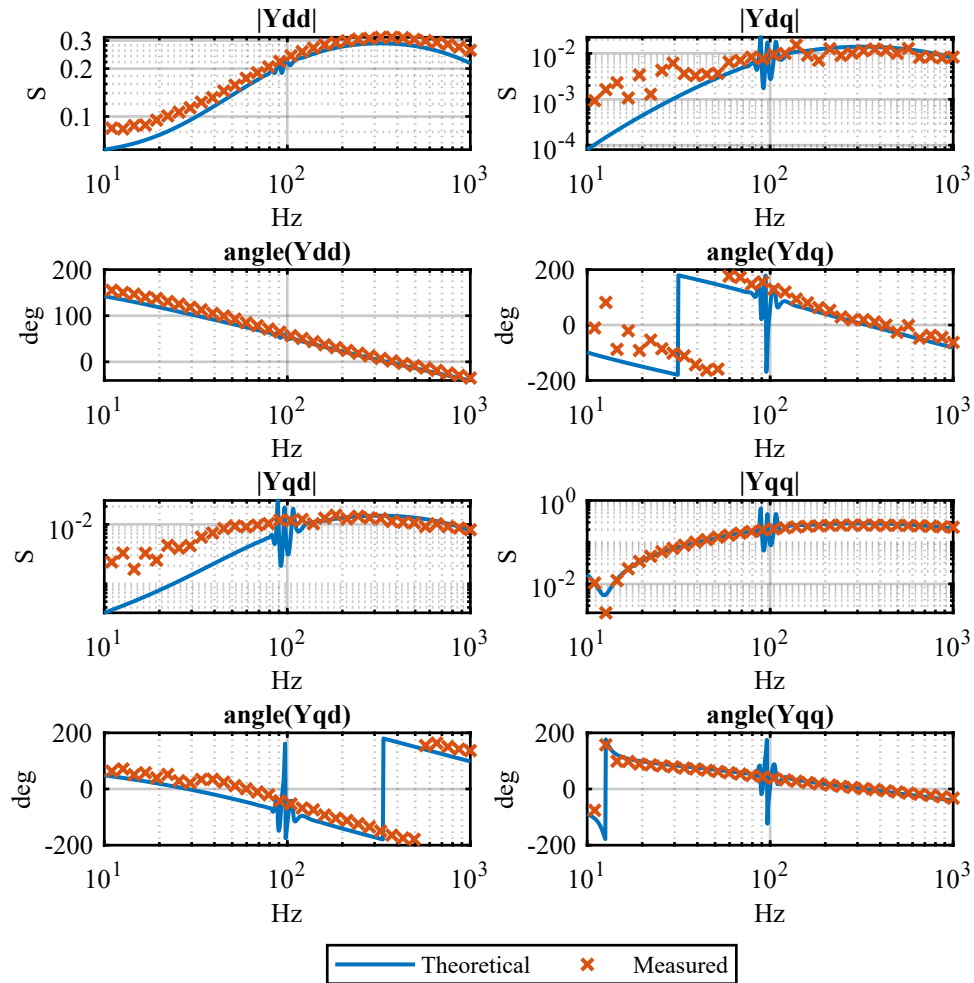


Figure 3.25: Comparison between the experimental measurements of the equivalent admittance of the considered grid-connected converter and the theoretical solution.

Fig. 3.17, the reader can notice that while the results are almost the same at high frequencies, they differ by one order of magnitudes at frequencies under 50 Hz. Since the difference with the experimental results occurs around 50-100 Hz, the cause can be the effect of the DC/DC converter

- The current sensors that were used are *LEM* hall effect sensors with a 200 A full scale. At low frequencies, the measured currents were less than 1 A. Therefore the uncertainty on the measurements was quite high. Since the admittances that should be measured are very little, a small error in

the measurements produces a strong variation on the result.

- As already mentioned in Section 3.6.2, the disturbance that occurs at around 100 Hz is an issue due to the inversion of the matrices required for the analytical calculation, but should not be considered. This phenomenon becomes negligible when a feed-forward is considered, as shown in Fig. 3.26. However,

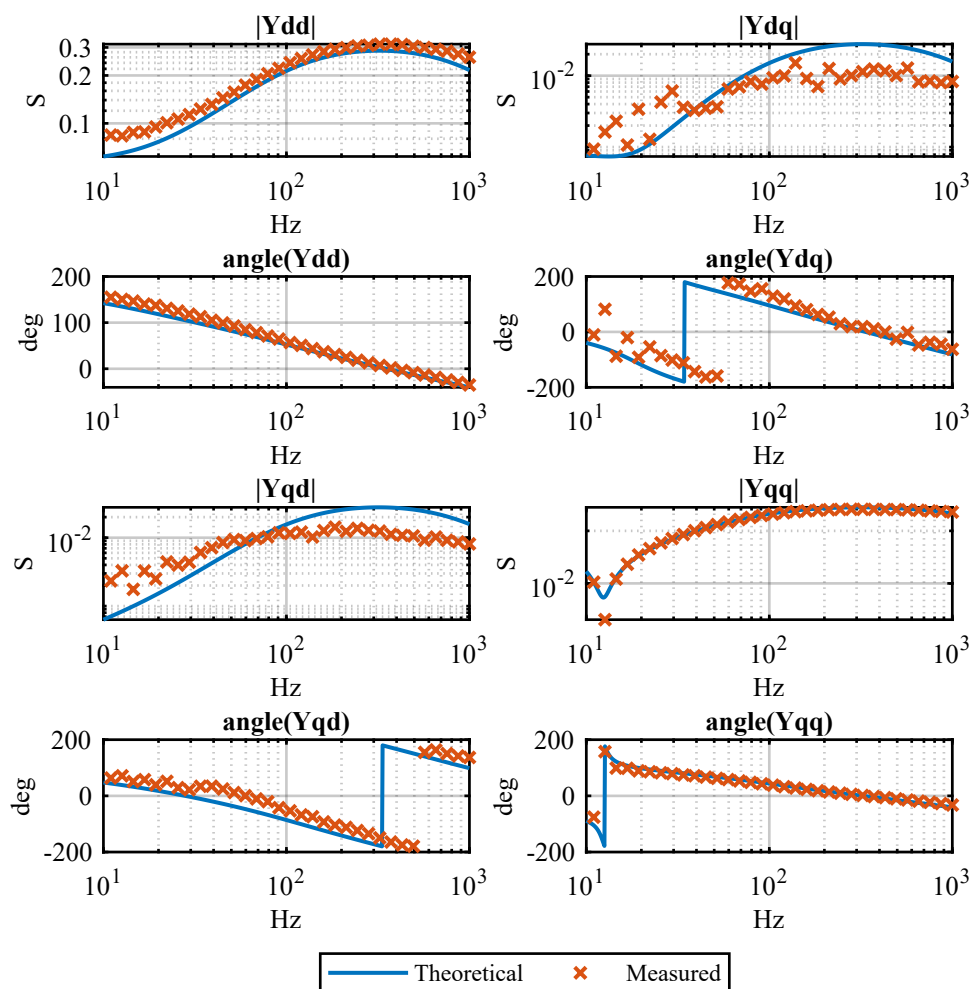


Figure 3.26: Comparison between the experimental measurements of the equivalent admittance of the considered grid-connected converter and the theoretical solution.

in this comparison while the 100 Hz disturbance has disappeared there is a difference at high frequencies, produced by the feed forward. This phenomenon

was already described in Section 3.6.2.

- As already stated in Section 3.6.2, instability problems are more likely in proximity of the bandwidth frequency of the current control. Therefore the inaccuracy at very low frequencies, although common in technical literature, is usually neglected.



## Chapter 4

# Impedance Estimation Through Transient Analysis

A possible technique in order to obtain the equivalent impedance of a converter is to analyse the transient response of a converter in steady-state operation when a discontinuity perturbation is applied.

This method has not been greatly explored in technical literature. In fact, only [35] and [34] deal with this topic. These considered a very simple case of a DC/DC converter, for which the perturbation on the steady-state operation could be obtained by varying a passive load. This was obtained by considering a resistive-capacitive load to make the converter work at a specific operating point, and a second load that was connected (or disconnected) to obtain a step variation in the load. Since the control was a voltage control, the load step variation produced a step on the currents supplied by the converter. In particular, if the  $(d, q)$  rotating frame is considered, the connection/disconnection of a resistive load produces a step on the  $d$ -axis current, while the connection/disconnection of a reactive load such as a capacitor produces a step on the  $q$ -axis current. The reason of this behaviour is immediately clear when the power absorbed by the converter is written in the

$(d, q)$  reference frame, as explained in Section 2.2.3:

$$p = \frac{3}{2} \cdot v_d \cdot i_d \quad (4.1)$$

$$q = \frac{3}{2} \cdot v_d \cdot i_q \quad (4.2)$$

However, this solution is only valid for voltage-controlled converters. It is unfortunately inapplicable to grid-connected converters, that usually control the output currents. No contribution in technical literature was found for current-controlled converters.

This work explores the possibility of an equivalent impedance measurement through the analysis of a transient response. The proposed method emulates a grid fault that produces a perturbation on grid voltage in the  $(d, q)$  frame, and observes the converter response through the analysis of the transient on  $(d, q)$  currents.

## 4.1 System Identification Overview

The aim of System Identification (SI) methods is to estimate a transfer function that, given a measured input to a dynamic system, produces an output that is as similar as possible to the measured output. This is a black box process that tries to evaluate the transfer function coefficients given a specific order as input. However, the dynamic system order is usually unknown, and thus must be guessed. If no information is available, an iterative process that gives an order to identification method and compares results of various orders. Because of this reason, the identification method complexity greatly influences estimation time and low complexity methods are preferred.

The general procedure for identification methods has been widely analysed by [6] and [17]. This first paragraph will only highlight the main points of the topic.

### 4.1.1 Identification Procedure

In general, every method requires the execution of four main steps:

1. Measurement of the input and output signals from the dynamic system. This can be obtained through specifically designed experiments or in some cases

by exploiting the normal operation of the system. However, this last case is not applicable to grid connected converters. In fact, the input perturbation should preferably be a step type variation in order to contain every frequency. Therefore a specifically designed experiment is used in this work, consisting in a step variation of a current in the  $(d, q)$  axis and the observation of the voltage response.

2. Selection of an identification type. This depends on the family of models among which the model will be chosen. In fact, identification types can be divided in various ways, as described in [6]. Some examples are:

- white, grey or black box identifications. In white box identifications, model structure is known and its parameters have to be estimated from measured data, while in grey box model structure is partially known, but has to be partially reconstructed from measured data (and its parameters as well). In black box methods, both the model structure and the parameters have to be completely estimated from measured data.
- parametric or non parametric methods. Given a specific model that is specified by the user and that is characterized by a finite set of unknown parameters  $\theta$ , parametric methods try to estimate the best  $\theta$  that produce the minimum error between an estimated and a measured output. On the contrary, non parametric methods try to identify a dynamic model without defining an *a priori* model structure. They describe the dynamics of a system through curves and tables, and can be useful for a preliminary analysis of a system.
- linear or non linear models. Non linear models have a higher computational burden. It can therefore be convenient to consider a non linear system as linear around specific operating points, and to evaluate a certain number of linear models (in the chosen operating points) instead of a single non linear model.
- continuous time or discrete time models. Usually models from identification methods are in the  $z$  domain. If a continuous time model is necessary, it is possible to transform the discrete time model into a Laplace domain

continuous time model.

3. Application of an estimation method for the evaluation of the parameters of the model structure. This process is carried out with the goal of minimizing the error between the model output  $\hat{y}$  and the measured response  $y$ . Although there are some exceptions, this procedure is usually iterative. Some commercial solutions are available in order to facilitate the estimation process. One of the most common is the *MATLAB System Identification Toolbox*, which provides a vast set of algorithms and commands that implement the main identification methods. Since the aim of this work was not the analysis of identification methods, the System Identification Toolbox was used for data processing.
4. Evaluation of the estimated model to test if it is adequate for the application needs. This can be carried out by comparing the measured response of the estimated model to the physical system measured response. This process is called *validation*, and must be done using different data from the one used in the estimation step. If the model prediction based on validation data input (*e.g* a current step) is near to validation data output (*e.g* a voltage response), then the model can be considered accurate.

### 4.1.2 Type of model

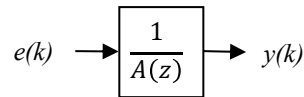
In dynamic systems the outputs depend both on the system input signals and on the past outputs. A dynamic model is a mathematical relation between the system input and output variables. This is usually a set of differential equations for continuous time systems or a set of difference equations for discrete time systems. Both can be represented through transfer functions or state space models. Since the final goal of this work is an admittance transfer function to which the Nyquist Stability Criterion can be applied, a transfer function model is a more straightforward representation.

### 4.1.3 Main Parametric Methods

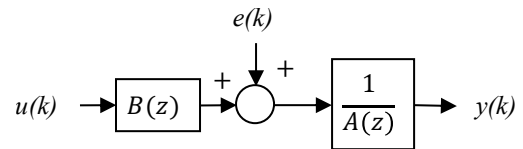
Although many parametric models are available, the most widely used models are five:

- AR models
- ARX models
- ARMAX models
- OE models
- BJ models

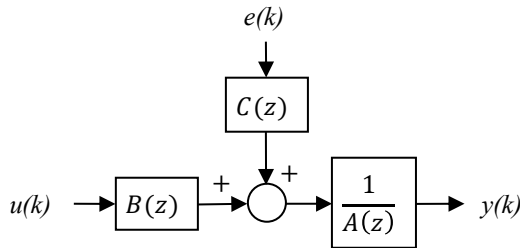
The following lines paragraphs highlight the structure of each model, while Fig. 4.1 represents them through block diagrams in the  $z$  domain.



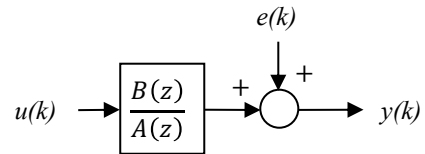
(a) AR model block diagram.



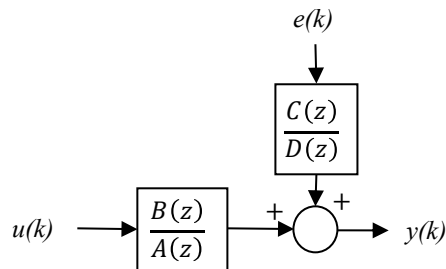
(b) ARX model block diagram.



(c) ARMAX model block diagram.



(d) OE model block diagram.



(e) BJ model block diagram.

Figure 4.1: Block diagrams of main identification models.

## AR Models

AR stands for *AutoRegressive* and is a model that has no input signal. It is the most simple model, consisting in only one polynomial. Its block diagram is shown in Fig. 4.1a.

As the name suggests, it is useful when an observed time variable presents a serial autocorrelation, *i.e.* a linear correlation with previous variable observations. Therefore this model is useful when past observations  $y(t - T_s)$ ,  $y(t - 2 \cdot T_s) \dots$  can help predicting current observation  $\hat{y}(t)$ .

It can be described by the following equation:

$$y(t) + a_1 \cdot y(t - T_s) + a_2 \cdot y(t - 2 \cdot T_s) + \dots + a_{n_a} \cdot y(t - n_a \cdot T_s) = \varepsilon(t) \quad (4.3)$$

where  $T_s$  is the sample time of the discrete system,  $\varepsilon(t)$  is a white noise disturbance with a null average and  $n_a$  is the order of the model, *i.e.* the number of previous observations used to produce the output. It must be highlighted that order of a transfer function in the discrete domain is different from the order in the Laplace domain. In fact, it does not represent the number of poles or zeros of the transfer function, but the number of past observations used to produce the output.

For compactness of notation the time delay operator  $q$  is introduced:

$$q^n = y(t - n \cdot T_s) \quad (4.4)$$

Then Eq. (4.3) can be rewritten in a compact way as:

$$A(q) \cdot y(t) = \varepsilon(t) \quad (4.5)$$

Where  $A(q)$  is a polynomial:

$$A(q) = 1 + a_1 \cdot q^{-1} + \dots + a_{n_a} \cdot q^{-n_a} \quad (4.6)$$

This model is not useful for the analysis of an equivalent impedance, since correlation with the input is clearly necessary.

## ARX Models

ARX stands for *AutoRegressive with eXtra inputs* because, differently from AR models, it includes an input signal. It is also called *AutoRegressive with Exogenous*

*Variables*, referring to the input signal as the exogenous variable. It is represented through a block diagram in Fig. 4.1b.

In ARX models the dynamic system is represented as a linear correlation of past input and output observations:

$$\begin{aligned} y(t) + a_1 \cdot y(t - T_s) + a_2 \cdot y(t - 2 \cdot T_s) + \dots + a_{n_a} \cdot y(t - n_a \cdot T_s) = \\ = b_1 \cdot y(t - n_k \cdot T_s) + b_2 \cdot y(t - 2 \cdot T_s - n_k \cdot T_s) + \dots + \\ + b_{n_b} \cdot y(t - (n_b - 1) \cdot T_s - n_k \cdot T_s) + \epsilon(t) \end{aligned} \quad (4.7)$$

where:

- $n_k$  is the number of input samples that occur before the input affects the output, also called system dead time. While it can be useful to model real systems, in this work system dead time is neglected and thus  $n_k$  is set to zero.
- $n_a$  is the number of past output observations used for the correlation.
- $n_b$  is the number of past input observations used for the correlation.

By applying the delay operator  $q$  described in (4.4) for input and output observations we can write (4.7) in a compact form:

$$A(q) \cdot y(t) = B(q) \cdot u(t) + \epsilon(t) \quad (4.8)$$

where:

$$A(q) = 1 + a_1 \cdot q^{-1} + \dots + a_{n_a} \cdot q^{-n_a} \quad (4.9)$$

$$B(q) = b_1 + b_2 \cdot q^{-1} + \dots + b_{n_b} \cdot q^{-n_b+1} \quad (4.10)$$

Therefore two polynomials have to be estimated. However, differently from the OE method, ARX is not iterative and therefore it is the most simple model to compute.

The output can be written as follows:

$$y(t) = \frac{B(q)}{A(q)} \cdot u(t) + \frac{1}{A(q)} \cdot \epsilon(t) \quad (4.11)$$

#### 4.1.4 OE Models

The term stands for *Output Error*, and its block diagram is shown in Fig. 4.1d. Its structure can be represented in the following way:

$$y(t) = \frac{B(q)}{A(q)} \cdot u(t) + \varepsilon(t) \quad (4.12)$$

where

$$A(q) = 1 + a_1 \cdot q^{-1} + \dots + a_{n_a} \cdot q^{-n_a} \quad (4.13)$$

$$B(q) = b_1 + b_2 \cdot q^{-1} + \dots + b_{n_b} \cdot q^{-n_b+1} \quad (4.14)$$

Similarly to the ARX model, two polynomials have to be estimated. This is one of the most used models because of its simplicity.

#### 4.1.5 ARMAX Models

The term stands for *AutoRegressive Moving Average with eXtra inputs*, and it can be represented through a block diagram as shown in Fig. 4.1c. It is structured as follows:

$$A(q) \cdot y(t) = B(q) \cdot u(t) + C(z) \cdot \varepsilon(t) \quad (4.15)$$

Therefore, differently from OE and ARX, three polynomials have to be estimated instead of two. Because of this reason the required computational burden for this model is higher than the one of ARX and OE.

In this model the input and the noise are filtered by the same dynamics:

$$y(t) = \frac{B(q)}{A(q)} \cdot u(t) + \frac{C(q)}{A(q)} \cdot \varepsilon(t) \quad (4.16)$$

As clearly stated by [6], "this is justified if the source of the disturbance enters early in the process, together with the input".

#### BJ Models

The term stands for *Box Jenkins*, and it is the most complete model. It is shown in Fig. 4.1e. It is structured in the following way:

$$y(t) = \frac{B(q)}{A(q)} \cdot u(t) + \frac{C(q)}{D(q)} \cdot \varepsilon(t) \quad (4.17)$$



supplied by three controlled voltage generators. At 0.1 seconds a voltage step is performed, in order to produce a current transient. The voltage amplitude was calculated in order to have steady state currents in the three phase reference frame with a peak of 2 A before the step, while the step amplitude was calculated in order to have a peak variation on the currents of 1 A. The used values are shown in Table 4.1.

Resistor	R	50 $\Omega$
Inductor	L	32 mH
Initial phase voltage amplitude	V	102 V
Phase voltage step amplitude	dV	51 V
Initial line-to-line voltage amplitude	V	88.3 V
Phase voltage step amplitude	dV	51 V
Initial current amplitude	I	2 A
Current amplitude after step	dI	1 A
Grid frequency	fg	50 Hz

Table 4.1: Values used in the PLECS simulation of Fig. 4.2

Fig. 4.3 shows the current and line-to-line voltage variation in the three phase reference frame.

### 4.2.2 Identification Procedure

Data in Fig. 4.3 was used to perform a system identification procedure using the *MATLAB System Identification Toolbox*.

The measurements were transformed into the  $(\alpha, \beta)$  frame and consequently into the  $(d, q)$  rotating reference frame. The result is visible in Fig. 4.4.

The identification was done with a OE model with order (1,2) in order to reduce the computational burden. At first a sampling frequency of 10 kHz was chosen and the identification was applied.

The resulting discrete transfer function are the measured admittances. These can be represented on the Bode diagram as shown in Fig. 4.5.

Some considerations can be done on the obtained results:

- As the reader can notice, the model is accurate enough at every frequency.

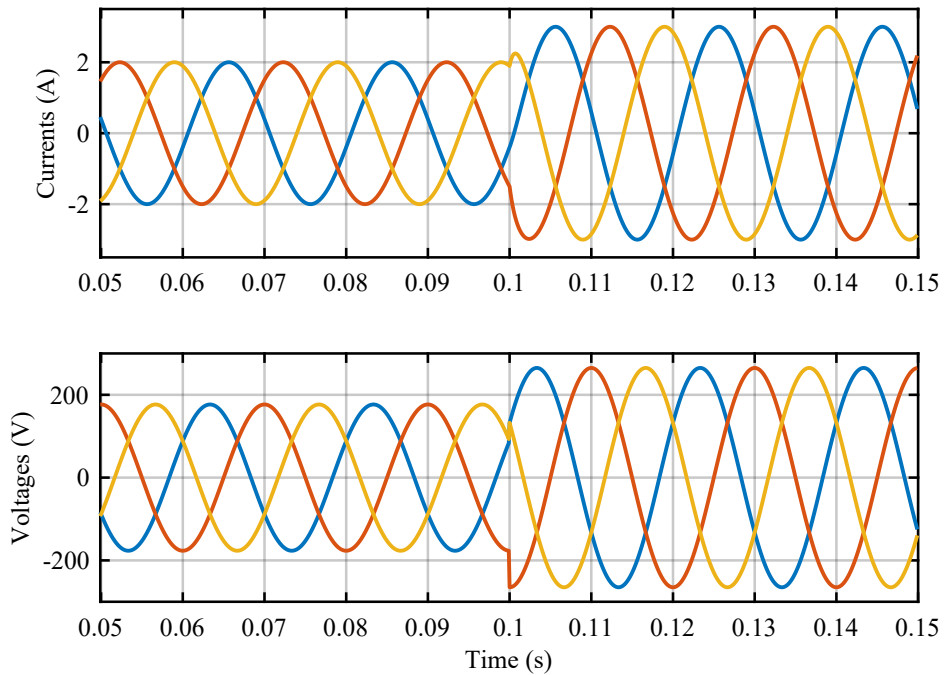


Figure 4.3: Voltage step and current transient in the three phase reference frame.

However, at high frequencies the identified transfer function starts to deviate from the theoretical solution. This is an effect of the proximity to the sampling frequency. As a rule of thumb for identification, the sampling frequency should be at least a decade higher than the frequency of interest for the model. Because of this reason, the identified model is valid until 1000 Hz. To demonstrate this statement, the same identification was repeated with a sampling frequency of 1 MHz. The result is shown in Fig. 4.6. As the reader can notice, when the sampling frequency is much higher than the model limit frequency, the difference in the transfer functions is negligible.

- In order to analyse the differences in the results between the different identification methods, a test was performed on an  $\text{ARX}(2,1)$ <sup>1</sup> and an  $\text{ARMAX}(2,1,1)$  as well. Results are shown in Fig. 4.7 for the most critical part of the model,

---

<sup>1</sup>The numbers in the parenthesis are the model order, written in the order in which polynomials appear when the model is written in the compact form used in Section 4.1.3

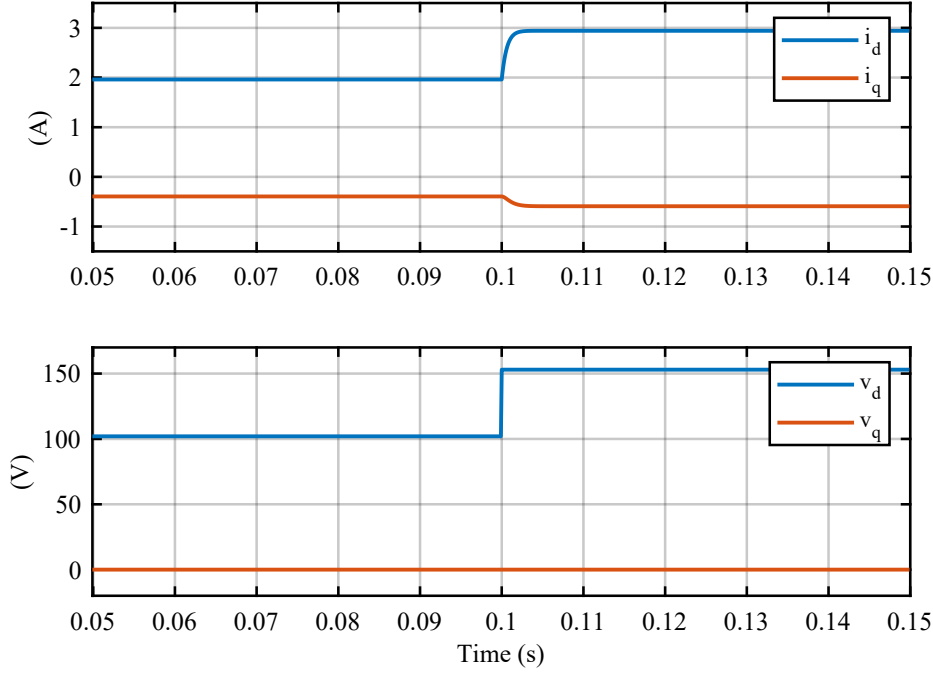


Figure 4.4: Voltage step and current transient in the  $(d, q)$  reference frame.

*i.e.* the highest frequencies. It can be observed that while there is a substantial difference between the correct phase and the identified one, the magnitudes are quite near to the analytical result. The best result is obtained with the ARMAX model. However, this model is computationally much heavier than the others. The ARX model produces a slightly better result than the OE model. Since this method is not iterative and thus computationally lighter, it can be considered a valid alternative to OE.

- The order of the discrete transfer function depends on the number of previous samples that are used from the input and output measurements to obtain the transfer function coefficients. Because of this reason, and since it is not possible to determine *a priori* the minimum order, the identified transfer function could have higher order from the theoretic transfer function of a generic system. Therefore while the different transfer functions have the same Bode diagram and behave in a similar way when the same input perturbations are applied, this is not valid for their inverse. The inverse of the identified transfer

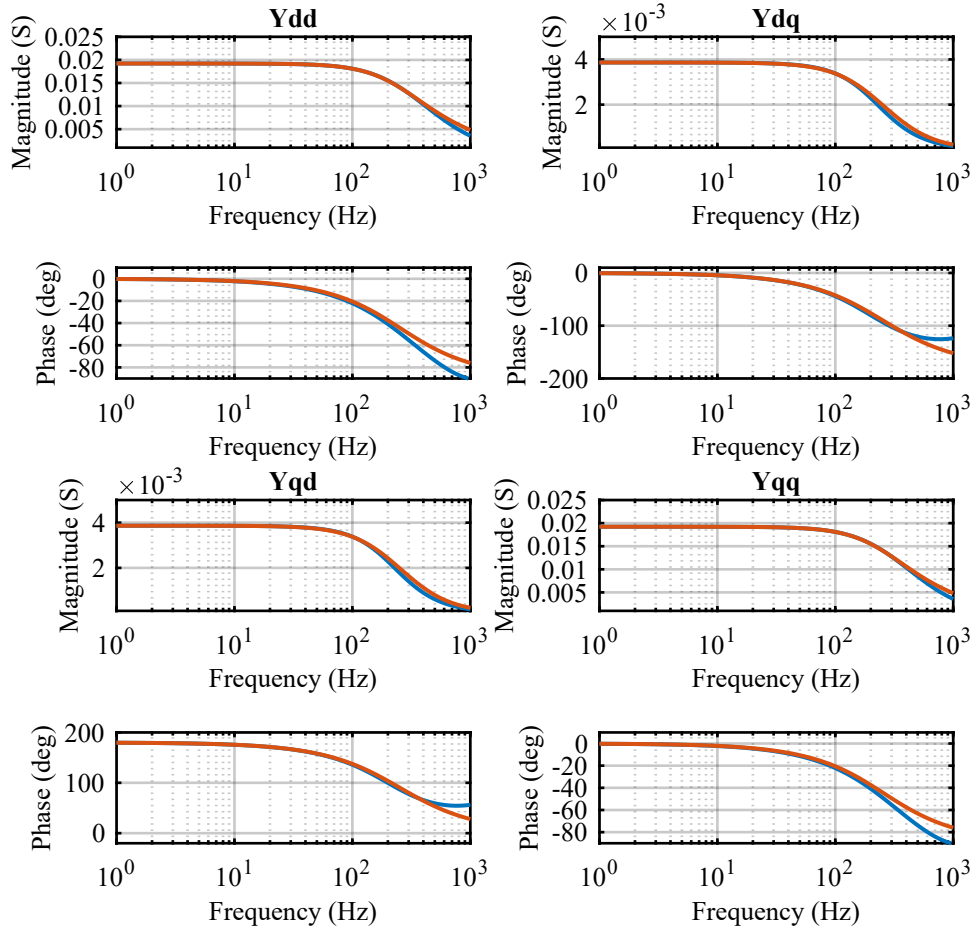


Figure 4.5: Bode diagram of identified RL admittance transfer function (in blue) when data is sampled at 10 kHz. For comparison the correct theoretical admittance is also reported (orange).

function will produce a different Bode diagram from the inverse of the theoretic transfer function, and the behaviour when the same input signals are applied is different. Because of this reason, the only way to invert an admittance matrix and obtain an impedance matrix is to calculate the magnitude and phase of the transfer function for every frequency of interest in order to obtain, for every frequency, a 2x2 complex matrix. This can be inverted to obtain the equivalent impedance at that frequency. This procedure must be repeated for

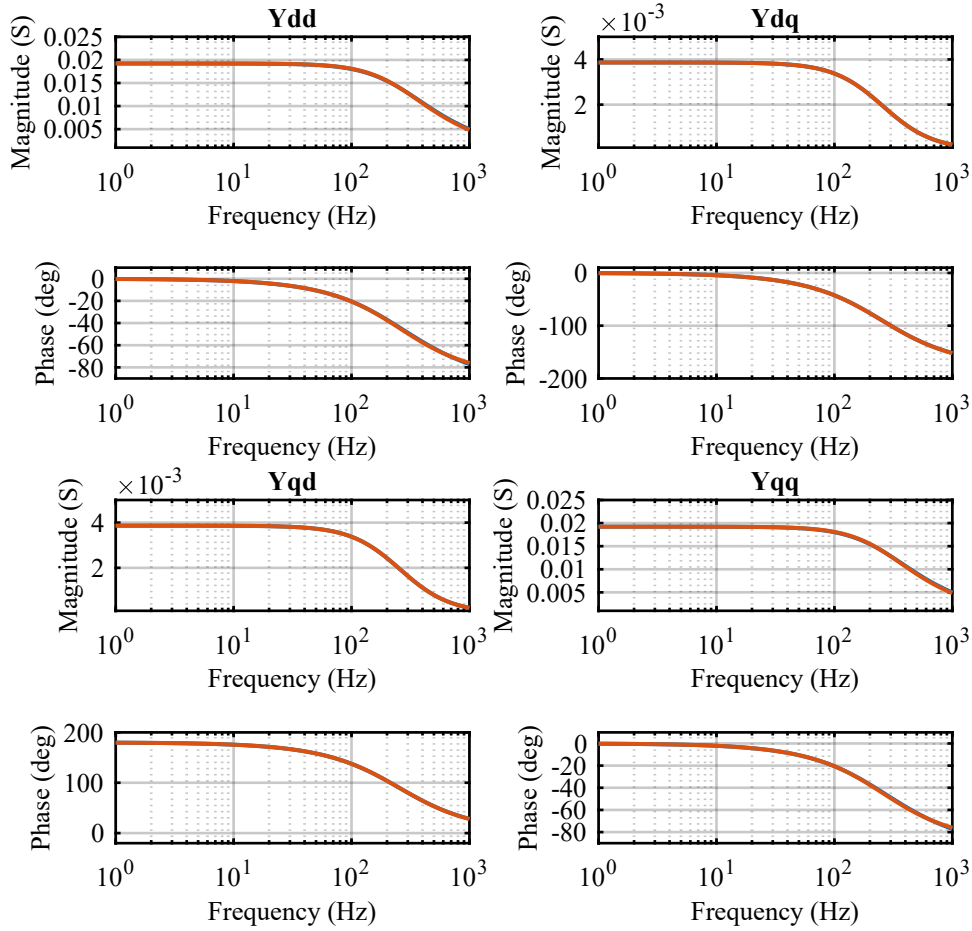


Figure 4.6: Bode diagram of identified RL admittance transfer function (in blue) when data is sampled at 1 MHz. For comparison the correct theoretical admittance is also reported (orange).

every frequency. Because of this procedure, the identified analytical solution is lost when the inverse is computed.

- The necessity to know the order of the identified system is a disadvantage of identification methods, since for complex circuits it is not known and must be guessed through iterations. This process is computationally heavy.

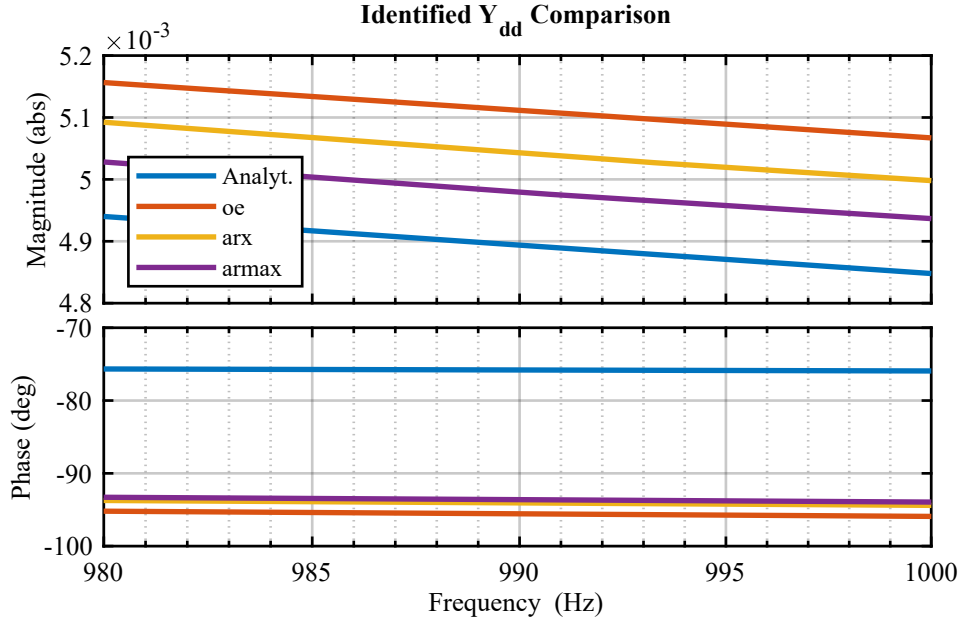


Figure 4.7: Comparison between identification methods for the estimation of  $Y_{dd}$

### 4.3 Simulation of Converter Identification

The characterization through transient analysis of a VSI with controlled output current is quite different from the one of DC/DC converters and inverters with controlled output voltage. In fact, no previous studies in technical literature were found on equivalent admittance measurements of current controlled DC/AC converters through transient analysis.

The characterization of a DC/DC converter or a VSI with controlled output voltage through transient analysis is much more simple, and has been investigated by [35].

Since the output voltage is controlled, a step in the output current produces the necessary transient on the voltage to perform an identification. This step can be easily obtained by performing a step on a passive load using the circuit in Fig. 4.8. If the Ohm's Law is considered:

$$\begin{bmatrix} v_d \\ v_q \end{bmatrix} = \begin{bmatrix} Z_{dd} & Z_{dq} \\ Z_{qd} & Z_{qq} \end{bmatrix} \cdot \begin{bmatrix} i_d \\ i_q \end{bmatrix} \quad (4.18)$$

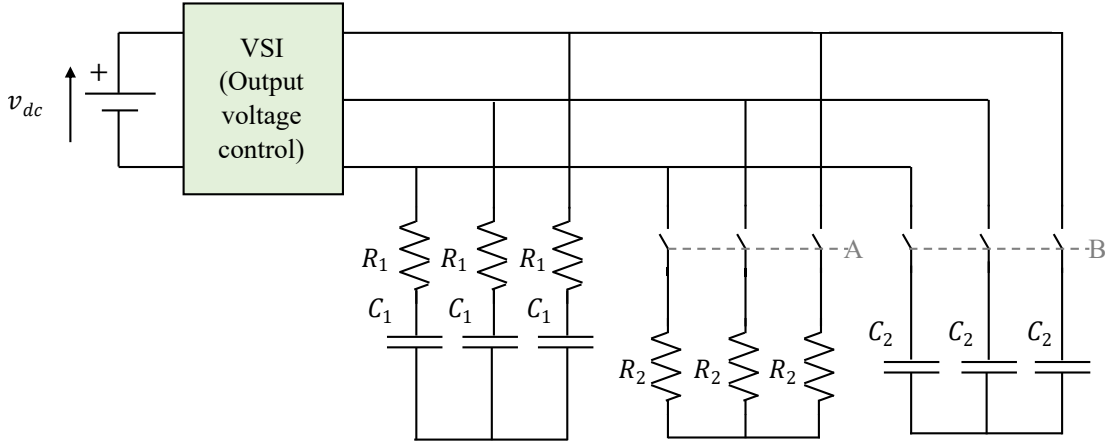


Figure 4.8: Test circuit for output voltage controlled VSI.

Therefore when the step is performed on  $i_d$  and  $i_q$  is null it is possible to measure  $Z_{dd}$  and  $Z_{qd}$ :

$$\begin{bmatrix} v_d \\ v_q \end{bmatrix} = \begin{bmatrix} Z_{dd} \cdot i_d \\ Z_{qd} \cdot i_d \end{bmatrix} \quad (4.19)$$

$$\begin{bmatrix} Z_{dd} \\ Z_{qd} \end{bmatrix} = \begin{bmatrix} v_d \cdot i_d \\ v_q \cdot i_d \end{bmatrix} \quad (4.20)$$

In order to obtain a step on the  $i_d$  it is possible to perform a resistive load connection or disconnection, *i.e.* considering a state change in switches A in Fig. 4.8.

On the contrary, when the step is performed on  $i_q$  and  $i_d$  is null it is possible to measure  $Z_{dq}$  and  $Z_{qq}$ :

$$\begin{bmatrix} Z_{dq} \\ Z_{qq} \end{bmatrix} = \begin{bmatrix} v_d \cdot i_q \\ v_q \cdot i_q \end{bmatrix} \quad (4.21)$$

Similarly, a step on the  $i_q$  is possible by performing a reactive load connection or disconnection, *i.e.* considering a state change in switches B in Fig. 4.8.

This procedure is not applicable to grid-connected converters, which usually behave as current sources. For this configuration a possibility explored in this work is the performance of steps on the grid voltage in the  $(d, q)$  rotating reference frame

through a grid simulator. This procedure is equivalent to the voltage transient during grid faults: a downwards step on the  $v_d$  is equivalent to a voltage sag, while a phase shift produces an impulsive transient on the  $v_q$ . In order to obtain a cleaner transient on the  $v_q$ , more similar to a transient, a step can be performed on the  $(d, q)$  frame angle. This produces a step on the  $v_q$  as well. However, in this case the  $d$ -axis of the new rotating reference frame is not coincident any more with the voltage vector, although it is still synchronous.

The test circuit that must be considered is briefly described by Fig. 4.9.

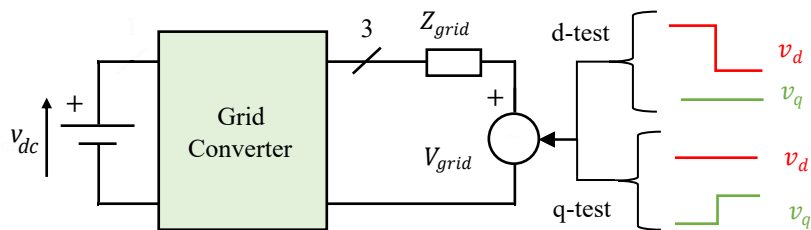


Figure 4.9: Transient analysis method test circuit.

This procedure can be obtained in *PLECS* with the circuits shown in Fig. 4.10. An example of voltage step tests and current response for a converter with only output current control is shown in Fig. 4.11.

### 4.3.1 Simulation Results of Equivalent Admittance Measurements

Two simulations were done considering the converter current response to voltage steps. This was used to perform a transient analysis through system identification techniques, whose output was the estimated equivalent admittance. The results are shown in the following paragraphs.

#### Identification of Converter with Output Current Control

The first simulation considered a converter with only output current control, working as a generator and injecting  $I_d = 10A$  into the grid. The system identification was performed by considering the methods and the orders reported in Table 4.2. The results of the identification and their comparison with the theoretical results

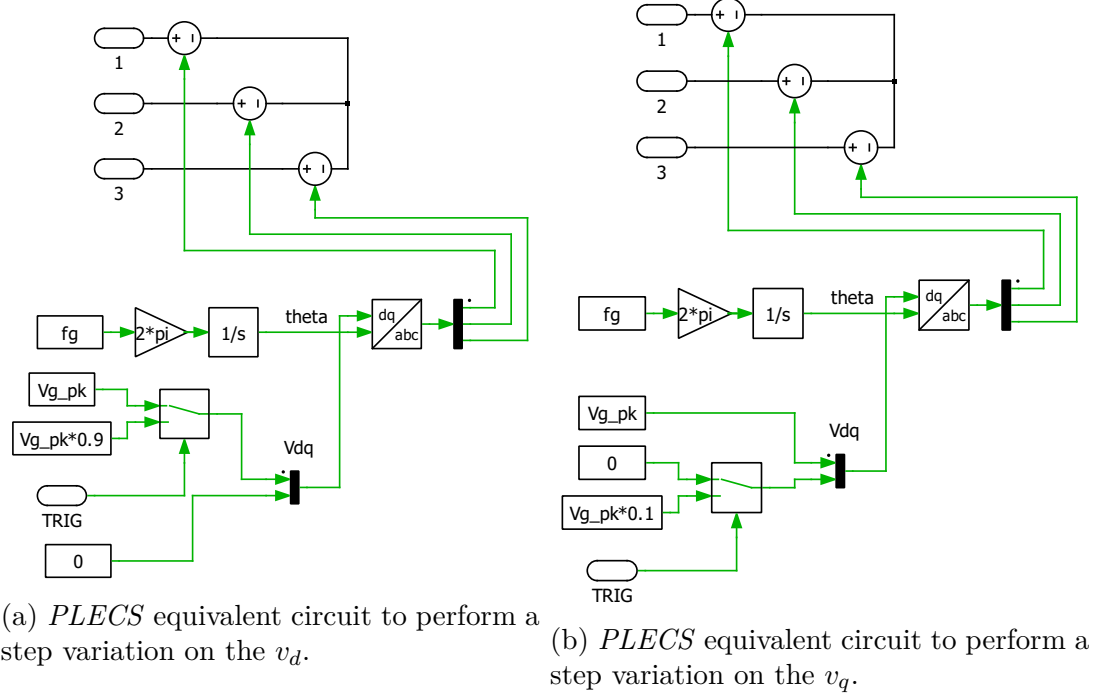


Figure 4.10: Block diagrams of main identification models.

Admittance	Identification Method	Order
$Y_{dd}$	oe	(10,10)
$Y_{dq}$	oe	(5,5)
$Y_{qd}$	oe	(50,50)
$Y_{qq}$	oe	(90,90)

Table 4.2: Admittance identification methods and orders for the admittance measurement with only current control.

are shown in Fig. 4.12.

The reader can notice how the self-admittances  $Y_{d,d}$  and  $Y_{q,q}$  perfectly correspond to the theoretical results. As for the mutual-admittances,  $Y_{q,d}$  has a perfect correspondence at almost every frequency up to 2000 Hz, then it starts to deviate from the theoretical solution. This deviation is, however, quite small. On the contrary  $Y_{d,q}$  has a good correspondence for every frequency over 100 Hz. Before 100 Hz the measured admittance is near the theoretical result but not coincident. The difficulty in measuring the mutual-admittances can be explained by considering the

amplitude of the current responses to the step perturbations. The auto-admittances are calculating by estimating a transfer function between a voltage step on one axis and the current step response on the same axis, while mutual-admittances are calculating considering a voltage step on one axis and the current response on the other axis. As the reader can notice in Fig. 4.11, while the current response on the same axis has an easily observable transient, with a transient peak of around 6 A, current responses on the other axis have a much lower amplitude, with a transient peak of around 400 mA. For this reason the numerical identification encounters some difficulties and sometimes fails to explain some dynamics.

### Identification of Converter with Output Current and DC Voltage Control

the second simulation considered a converter controlled with an output current loop and a DC voltage loop. As for the previous simulation, the converter worked as a generator, injecting  $I_d = 10A$  and  $I_q = 0A$  into the grid. The identification was carried out considering the methods and orders shown in Table 4.3. The results of

Admittance	Identification Method	Order
$Y_{dd}$	oe	(50,50)
$Y_{dq}$	oe	(70,70)
$Y_{qd}$	oe	(40,40)
$Y_{qq}$	oe	(11,57)

Table 4.3: Admittance identification methods and orders for the admittance measurement with current and voltage control.

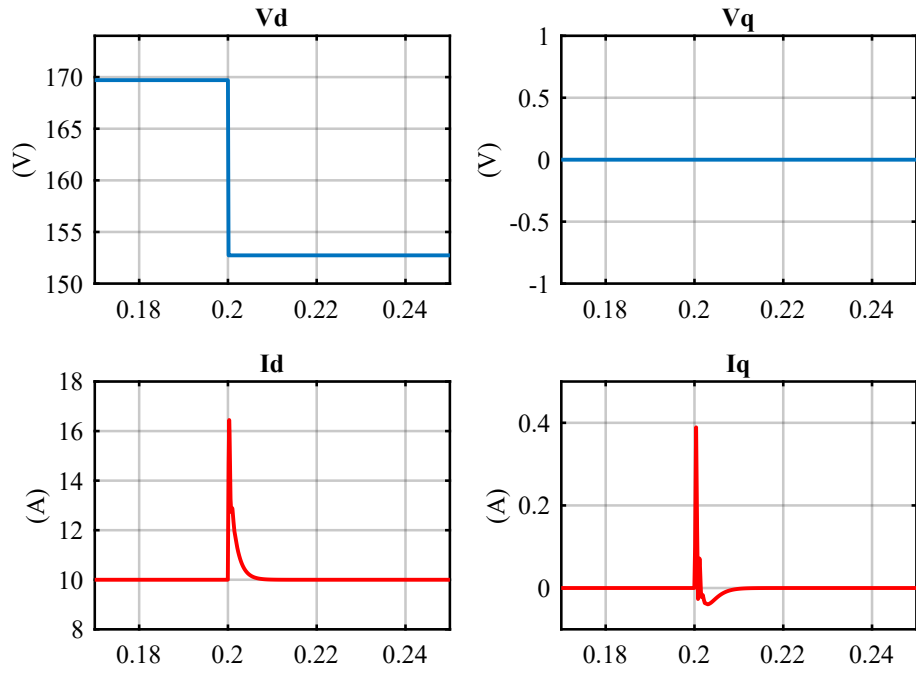
the identification and the comparison with the theoretical results are shown in Fig. 4.13.

As the reader can notice, the auto-admittances  $Y_{d,d}$  and  $Y_{q,q}$  and the mutual-admittance  $Y_{q,d}$  perfectly fit the theoretical results. The only difference is in the  $Y_{d,q}$ , where the theoretical and measured admittances are different for frequencies under 100 Hz. This problem is the same that was presented showing the result comparison in Fig. 4.12 and derives from the very little  $i_d$  current response with respect to the  $v_q$  voltage perturbation.

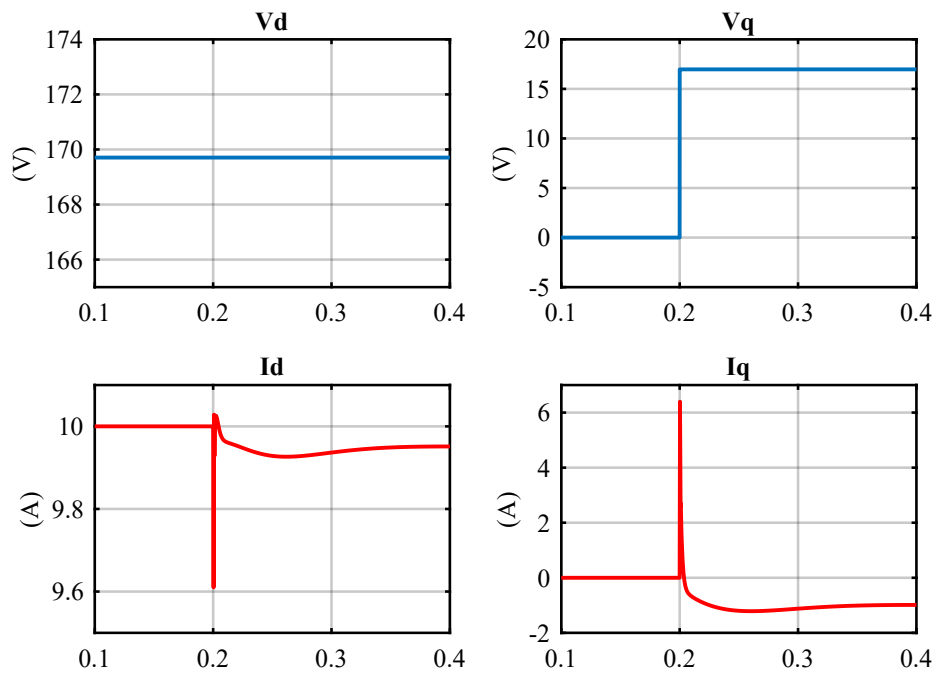
Using the MATLAB *compare* function from the *System Identification Toolbox* the measured admittances were used to estimate the system response to voltage steps. The result is shown in Fig. 4.14 and 4.15. The estimated responses using  $Y_{d,d}$ ,  $Y_{q,d}$  and  $Y_{q,q}$  are very accurate, while  $Y_{d,q}$  fails to predict transients at very low frequencies. This problem is related to the measured admittance at low frequencies, which is different from the theoretical result. As already stated in Section 3.6.2, equivalent admittance inaccuracies are common in technical literature and usually neglected, since harmonic stability problems mostly occur in proximity of the bandwidth frequency of the current control.

Moreover, there is a disturb in the theoretical result near 100 Hz. This issue was already discussed in Section 3.6.2. It depends on the matrix manipulation that is used for obtaining the final curve, but should not be considered.

Overall, it can be stated that the measured impedances through simulation well correspond to the theoretical results, this proving that this method is valid.



(a) *PLECS* simulation of  $v_d$  step and relative current transients.



(b) *PLECS* simulation of  $v_q$  step and relative current transients.

Figure 4.11: *PLECS* simulation of voltage steps and relative current transients for a converter with only current control. 115

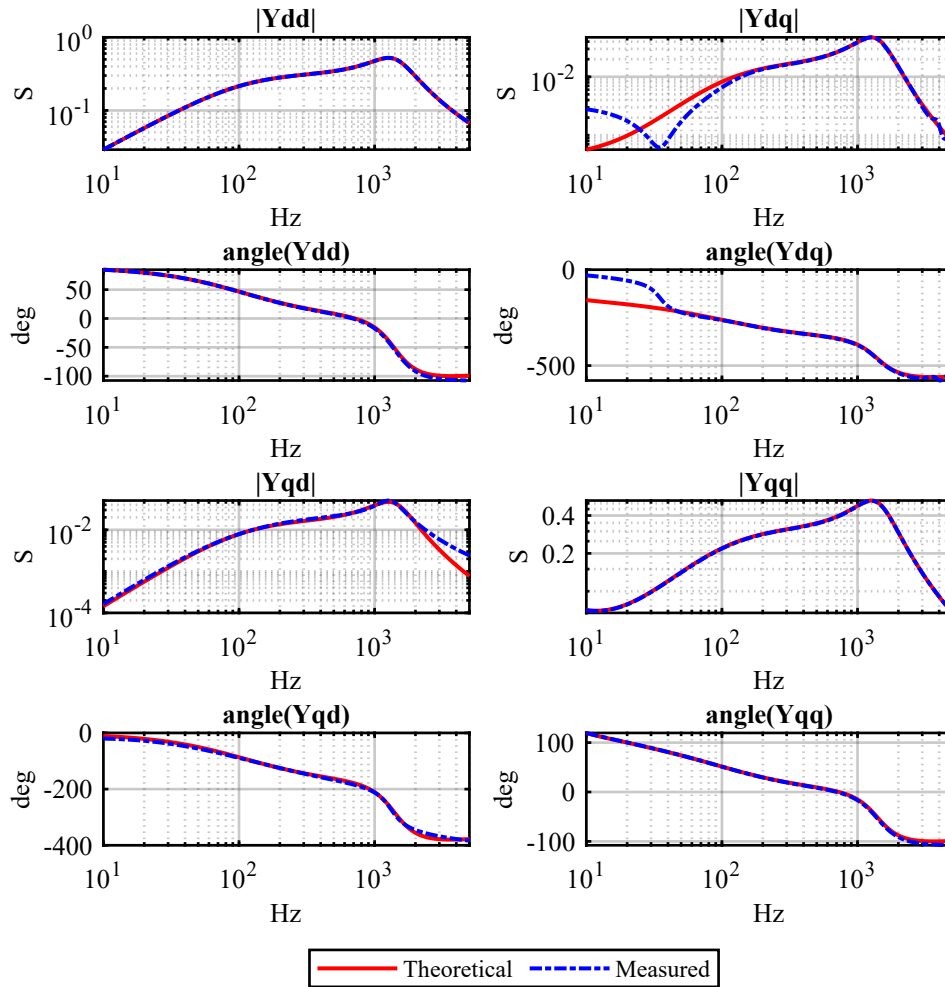


Figure 4.12: Comparison between theoretical equivalent admittance and measured admittance through transient analysis method when only output current control is considered.

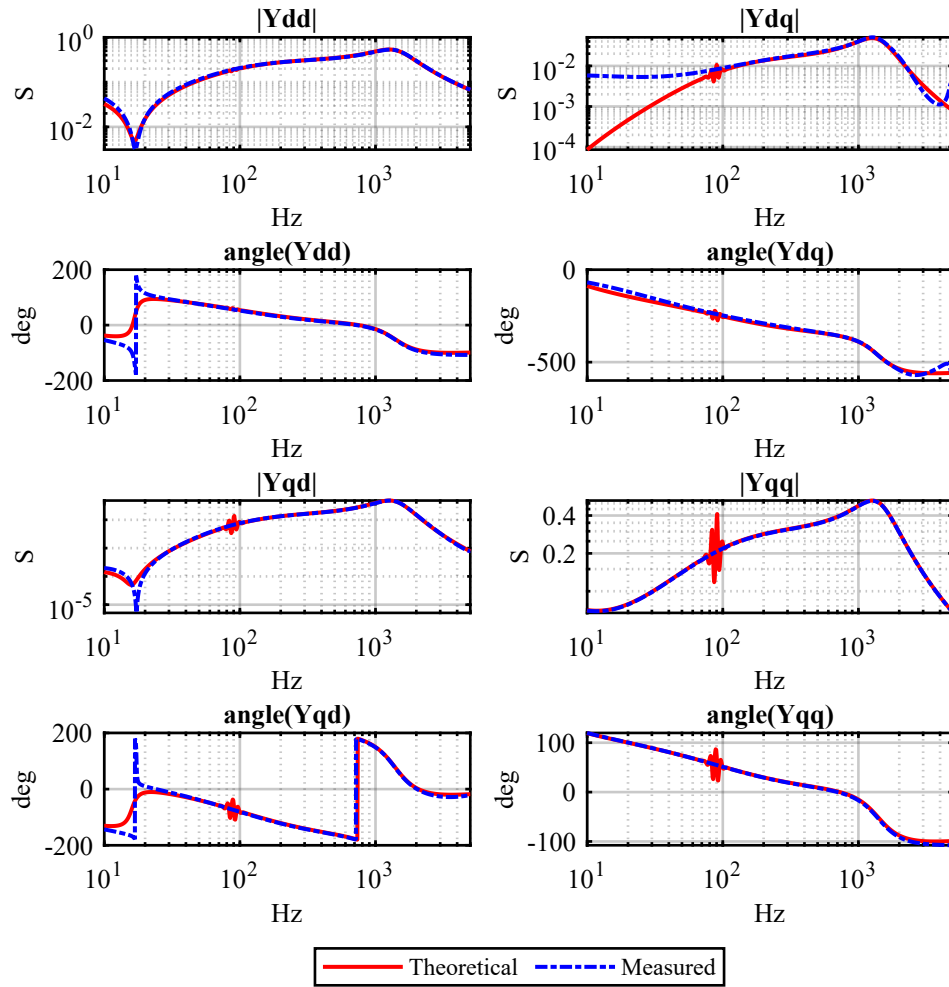


Figure 4.13: Comparison between theoretical equivalent admittance and measured admittance through transient analysis method when both output current control and DC voltage control are considered.

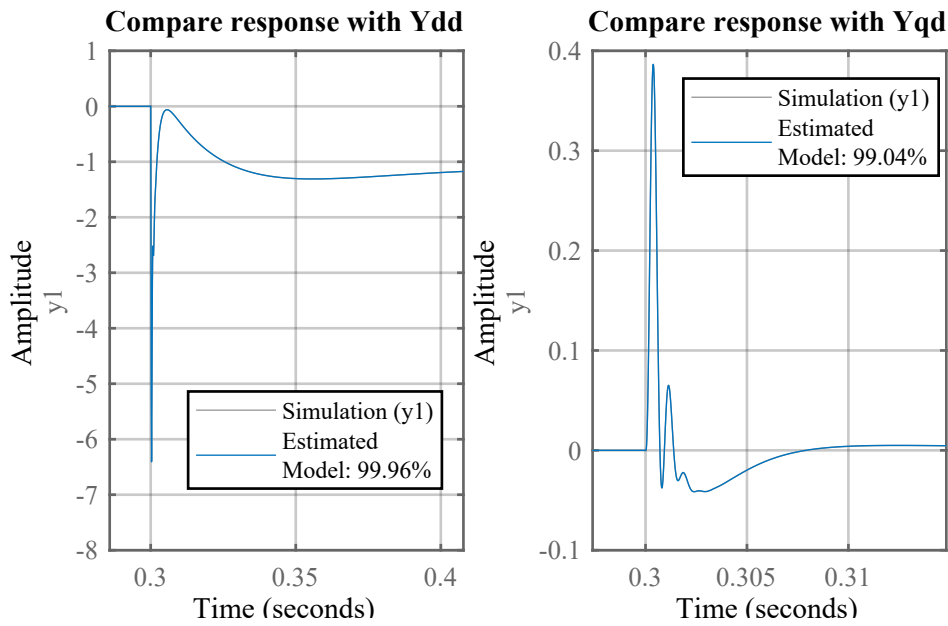


Figure 4.14: Comparison between estimated system response to a  $v_d$  step through measured impedance and simulation data.

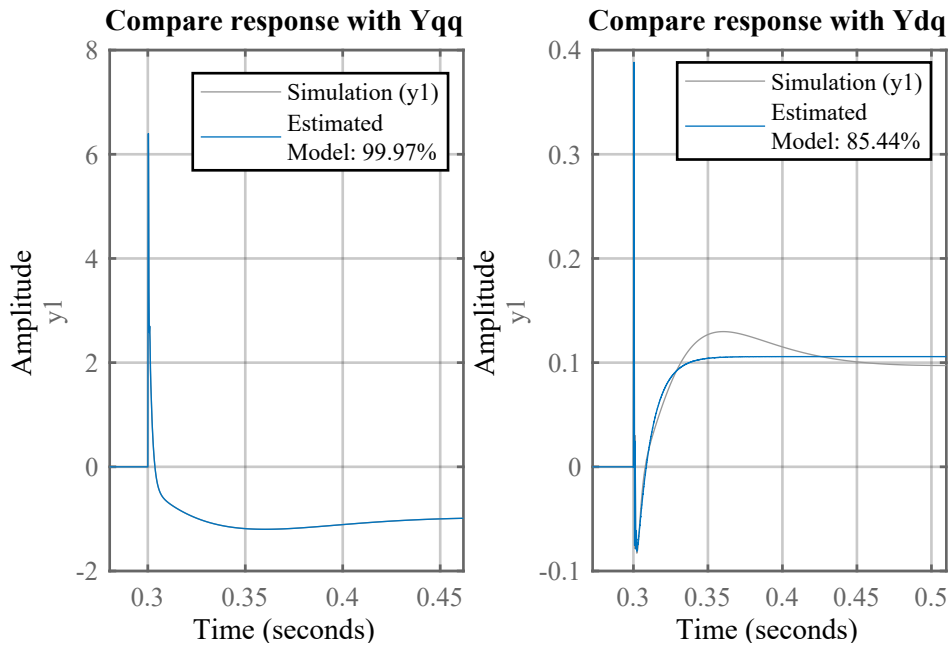


Figure 4.15: Comparison between estimated system response to a  $v_q$  step through measured impedance and simulation data.

# Chapter 5

## Conclusions

In this work two black-box methods for the measurement of the equivalent admittance of a grid converter were analysed and implemented. First, the voltage injection method was validated both in simulation and experimentally, then the transient analysis only in simulation. The results were then compared to a theoretical calculation of the converter admittance.

My personal contributions to this work were:

- analysis of technical literature on black-box methods for equivalent admittance measurement;
- analysis of main System Identification methods;
- sizing and experimental implementation of a discrete control on a grid-connected converter;
- admittance measurement of a grid converter with the voltage injection method through simulation and experimental set-up;
- admittance measurement of a grid converter with the transient analysis method through simulation;

While technical literature expressed the possibility of VSI admittance measurement through injection of a voltage perturbation, it lacked on describing an implementation of this method on an experimental set-up. This was deeply studied in Chapter 3 of this work in every aspect of its implementation.

The admittance measurement through transient analysis was described in Chapter 4 of this work. This measurement method is described in technical literature only for converters with AC output voltage control, therefore it was not applicable to grid converters such as battery chargers, which usually control the AC output current. This work considered a new method of performing transient analyses on grid converters by applying step perturbations on the grid voltage and validated it in simulation.

The comparison among these two methods can be summarized as follows:

- In a simulation environment both methods can measure the equivalent admittance in a satisfactory way. However, the experimental implementation of the transient analysis method is more difficult because of the very low-amplitude current responses with respect to the ripple and measurement disturbances. This issue still needs to be solved. The transient analysis method is therefore not mature enough for an experimental validation.
- The signal injection method can be applied to the converter under test more easily than the transient analysis method, and can be performed automatically without the interaction of the user. Therefore, in an industrial environment almost no previous knowledge or training is required to the testing engineer in order to perform this test. This is not the case of the transient analysis method, where the testing engineer must have a basic knowledge of system identification methods and must manually examine the behaviour of different orders of the transfer function by comparing the estimated output of the model with the measured one. This can be automated, but with a very high computational burden and therefore requiring long times to be done.
- Data processing of the transient analysis method requires the System Identification Toolbox from MATLAB or an equivalent system identification library, while the data processing of the signal injection method can be easily implemented on many programming languages. A company that needs to perform an equivalent admittance measurement of a converter may not have MATLAB licenses, thus the system identification method could be not feasible. Therefore an identification software should be written by zero on a different environment.

This is time consuming and requires a great knowledge of system identification methods.

- The transient analysis method is faster to accomplish than the signal injection method, therefore can be useful to obtain fast results and a first idea of the admittance curve even when the order of the transfer function is not known.

These statements suggest that the signal injection method is at the moment the most preferable solution in an industrial environment for its easiness of use.

While the voltage injection method can therefore be considered a quite mature procedure, the transient analysis method is new and needs to be further developed. Future works will consist in the improvement of this method through the experimental implementation, trying to solve the problem of very low response amplitudes with respect to ripple and measurement disturbances.



# Appendix A

## PLL Sizing Insights

### PI Controller Sizing through the Open Loop Transfer Function

To determine the bandwidth of the PLL using the open loop transfer function method, we can consider that at high frequencies  $G_{OL,PLL}$  can be approximated to:

$$G_{OL,PLL} \Big|_{h,f} \simeq \frac{k_{p,PLL} \cdot |V_{dq}|}{s} \quad (\text{A.1})$$

$$G_{OL,PLL} \Big|_{\omega_{bw,PLL}} = 1 \simeq \frac{k_{p,PLL} \cdot |V_{dq}|}{\omega_{bw,PLL}} \quad (\text{A.2})$$

From which the bandwidth frequency can be calculated as:

$$\omega_{bw,PLL} = k_{p,PLL} \cdot |V_{dq}| \quad (\text{A.3})$$

$$k_{p,PLL} = \frac{\omega_{bw,PLL}}{|V_{dq}|} \quad (\text{A.4})$$

This approximation is valid only if the zero of the controller transfer function is sufficiently far from the bandwidth frequency. Moreover, the zero must be far from the bandwidth frequency in order to ensure a sufficient phase margin at the bandwidth frequency. We can therefore position  $\omega_{z,PLL}$  a decade before  $\omega_{bw,PLL}$ :

$$\omega_{z,PLL} = \frac{\omega_{bw,PLL}}{10} = \frac{k_{i,PLL}}{k_{p,PLL}} \quad (\text{A.5})$$

From (A.5) we can calculate the integral gain of the controller:

$$k_{i,PLL} = k_{p,PLL} \cdot \frac{\omega_{bw,PLL}}{10} \quad (\text{A.6})$$

For the sizing of the controller the reader must consider that the PLL bandwidth  $\omega_{bw,PLL}$  must be low in order to reduce PLL sensitivity to voltage disturbances. A too low frequency however results in long transients, hence the PLL output will suffer of load variations for a longer time. A good compromise is to keep a bandwidth between 4 and 20 Hz. If a  $f_{bw,PLL}$  of 5 Hz and a constant voltage amplitude of 325 V are considered, the results of the PLL sizing are shown in Table A.1. The Bode diagram of the results with this PLL setup is shown in Fig. A.1.

Parameter	Value
$f_{bw,PLL}$	5 Hz
$\omega_{bw,PLL}$	31.4159 rad/s
$f_{bw,PLL}$	0.5 Hz
$\omega_{z,PLL}$	3.1416 rad/s
$k_{p,PLL}$	0.0967 1/(V·s)
$k_{i,PLL}$	0.307 rad/(V·s <sup>2</sup> )
Phase margin	84.318°

Table A.1: PLL setup values.

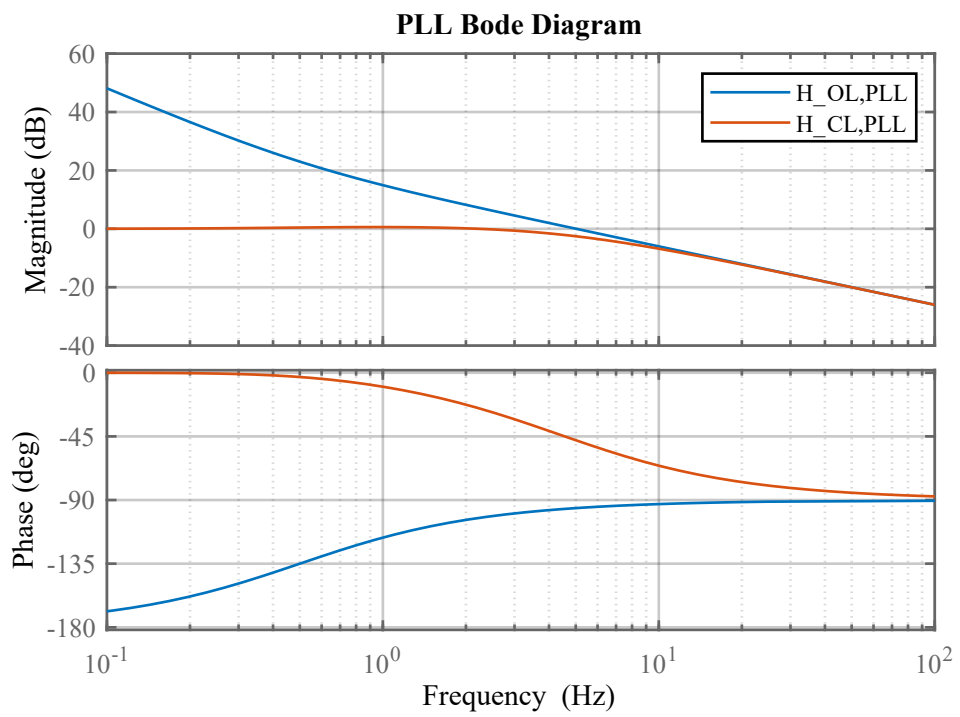


Figure A.1: Bode diagram of  $G_{OL,PLL}$  and  $G_{CL,PLL}$ .



## Appendix B

# Considered Transformation Matrices

### Amplitude Invariant Clarke Transformation

The matrix  $\mathbf{A}$  is used to transform a balanced signal<sup>1</sup> into a three phase reference frame into a  $(\alpha, \beta)$  frame without modifying the amplitude of the vectors:

$$\begin{bmatrix} x_\alpha \\ x_\beta \end{bmatrix} = \frac{2}{3} \cdot \begin{bmatrix} 1 & -\frac{1}{2} & -\frac{1}{2} \\ 0 & \frac{\sqrt{3}}{2} & -\frac{\sqrt{3}}{2} \end{bmatrix} \cdot \begin{bmatrix} x_a \\ x_b \\ x_c \end{bmatrix} = \mathbf{A} \cdot \begin{bmatrix} x_a \\ x_b \\ x_c \end{bmatrix} \quad (\text{B.1})$$

The MATLAB code to obtain this transformation is:

```
1 function [ab] = clarke_PH(rst)
2     tmp = (rst.r + rst.s + rst.t) / 3.0;
3     ab.a = rst.r - tmp;
4     ab.b = (rst.s - rst.t) / sqrt(3);
5 end
```

If the three phase signals are line-to-line voltages it is possible to unite in the transformation the line-to-line to phase transformation and the three phase to  $(\alpha, \beta)$

---

<sup>1</sup>Therefore  $x_a + x_b + x_c = 0$

transformation with the matrix  $\mathbf{A}_{ll}$ :

$$\begin{bmatrix} x_\alpha \\ x_\beta \end{bmatrix} = \frac{2}{3} \cdot \begin{bmatrix} \frac{1}{3} & 0 & \frac{1}{3} \\ 0 & \frac{1}{\sqrt{3}} & 0 \end{bmatrix} \cdot \begin{bmatrix} x_{a,ll} \\ x_{b,ll} \\ x_{c,ll} \end{bmatrix} = \mathbf{A}_{ll} \cdot \begin{bmatrix} x_{a,ll} \\ x_{b,ll} \\ x_{c,ll} \end{bmatrix} \quad (\text{B.2})$$

The MATLAB code to obtain this transformation is:

```
1 function [ab] = clarke_LL(rst)
2     ab.a = (rst.r - rst.t)/3.0;
3     ab.b = rst.s/sqrt(3);
4 end
```

### Inverse Clarke Transformation

The matrix  $A^{-1}$  is used to transform a  $(\alpha, \beta)$  frame signal into a three phase reference frame signal without modifying the amplitude of the vectors:

$$\begin{bmatrix} x_a \\ x_b \\ x_c \end{bmatrix} = \frac{3}{2} \cdot \begin{bmatrix} \frac{2}{3} & 0 \\ -\frac{1}{3} & \frac{\sqrt{3}}{3} \\ -\frac{1}{3} & -\frac{\sqrt{3}}{3} \end{bmatrix} \cdot \begin{bmatrix} x_\alpha \\ x_\beta \end{bmatrix} = \mathbf{A}^{-1} \cdot \begin{bmatrix} x_\alpha \\ x_\beta \end{bmatrix} \quad (\text{B.3})$$

The MATLAB code to obtain this transformation is:

```
1 function [rst] = clarke_LL(ab)
2     rst.r = ab.a;
3     rst.s = -0.5*ab.a + 0.5*sqrt(3)*ab.b;
4     rst.t = -0.5*ab.a - 0.5*sqrt(3)*ab.b;
5 end
```

### Rotation Transformation $\mathbf{R}(\theta)$

The matrix  $\mathbf{R}(\theta)$  is used to transform a  $(\alpha, \beta)$  frame signal into a  $(d, q)$  rotating frame signal:

$$\begin{bmatrix} x_d \\ x_q \end{bmatrix} = \begin{bmatrix} \cos(\theta) & \sin(\theta) \\ -\sin(\theta) & \cos(\theta) \end{bmatrix} \cdot \begin{bmatrix} x_\alpha \\ x_\beta \end{bmatrix} = \mathbf{R}(\theta) \cdot \begin{bmatrix} x_\alpha \\ x_\beta \end{bmatrix} \quad (\text{B.4})$$

The MATLAB code to obtain this transformation is:

```

1 function [dq] = rot(ab, theta)
2     sc.cos = cos(theta);
3     sc.sin = sin(theta);
4     dq.d = ab.a.*sc.cos + ab.b.*sc.sin;
5     dq.q = - ab.a.*sc.sin + ab.b.*sc.cos;
6 end

```

### Inverse Rotation Transformation $\mathbf{R}^{-1}(\theta)$

The matrix  $\mathbf{R}^{-1}(\theta)$  is used to transform a  $(d, q)$  frame signal into a  $(\alpha, \beta)$  frame signal:

$$\begin{bmatrix} x_\alpha \\ x_\beta \end{bmatrix} = \begin{bmatrix} \cos(\theta) & -\sin(\theta) \\ \sin(\theta) & \cos(\theta) \end{bmatrix} \cdot \begin{bmatrix} x_d \\ x_q \end{bmatrix} = \mathbf{R}^{-1}(\theta) \cdot \begin{bmatrix} x_d \\ x_q \end{bmatrix} \quad (\text{B.5})$$

The MATLAB code to obtain this transformation is:

```

1 function [ab] = invrot(dq, theta)
2     sc.cos = cos(theta);
3     sc.sin = sin(theta);
4     ab.a = dq.d.*sc.cos - dq.q.*sc.sin;
5     ab.b = dq.d.*sc.sin + dq.q.*sc.cos;
6 end

```



# Appendix C

## PLECS Code for the C-Script Block

### Output function code

```
1 // — VARIABLE ACQUISITION —
2 //Sampled Inverter Currents
3 Iabc.a      = InputSignal(0,0);
4 Iabc.b      = InputSignal(0,1);
5 Iabc.c      = InputSignal(0,2);
6 //Sampled DC Link Voltage
7 Vdc        = InputSignal(0,3);
8 //Enable Signal
9 USER_BUTTON = InputSignal(0,4);
10 //Sampled Voltage on the capacitors
11 Vabc.a     = InputSignal(0,5);
12 Vabc.b     = InputSignal(0,6);
13 Vabc.c     = InputSignal(0,7);
14 // Boost input current
15 Idc        = InputSignal(0,8);
16
17 // — PROTECTIONS —
18 // Overcurrent protection
19 if((fabs(Iabc.a) > iMax) || (fabs(Iabc.b) > iMax) || (fabs(Iabc.c) >
    iMax))
```

```

20     STATE = ERROR;
21     // Overvoltage protection
22     if (Vdc > vMax)
23         STATE = ERROR;
24
25     // Eliminate common mode current from sampled phase currents
26     tmp1      = (Iabc.a + Iabc.b + Iabc.c)*one_third;
27     Iabc.a    -= tmp1;
28     Iabc.b    -= tmp1;
29     Iabc.c    -= tmp1;
30     // Vdc filtering
31     Vdc_filt  += k_LPF_v*(Vdc - Vdc_filt);
32
33     //abc -> alpha,beta Transformation
34     DirectClarkePH(&Iabc, &Iab);
35     DirectClarkeLL(&Vabc, &Vab);
36
37     // Normalized voltages
38     Vab_peak  = Amplitude(&Vab);
39     if (Vab_peak < 0.1f)    Vab_peak = 0.1f;
40
41     // Secondary Order Generalized Integrator - Quadrature Signal
42     // Generator
43     sogiFilt.input      = Vab.alpha;
44     sogiFilt.output     = Vab_filt.alpha;
45     ResFilter(&sogiFilt);
46     Vab_filt.alpha     = sogiFilt.x1;
47     Vab_filt.beta      = -sogiFilt.x2;
48
49     // First estimation of voltage vector position
50     if (FIRST_TIME) {
51         Sin_Cos_theta.cos = Vab_filt.alpha/Vab_peak;
52         Sin_Cos_theta.sin  = Vab_filt.beta/Vab_peak;
53         theta_PLL          = atan2(Sin_Cos_theta.sin, Sin_Cos_theta.cos);
54         FIRST_TIME        = 0;
55     }
56
57     // alpha,beta -> d,q Transformation
58     DirectRot(&Iab, &Sin_Cos_theta, &Idq);

```

```
58 DirectRot(&Vab_filt, &Sin_Cos_theta, &Vdq);
59
60 // Third harmonic filtering (only for PLECS)
61 vd_filt.input = Vdq.d;
62 notch(&vd_filt);
63 Vdq.d = vd_filt.output;
64 vq_filt.input = Vdq.q;
65 notch(&vq_filt);
66 Vdq.q = vq_filt.output;
67
68 // PLL regulator
69 PLLReg.ref = Vdq.q/Vab_peak;
70 PLLReg.actual = 0.0f;
71 PLLReg.vfw = wg;
72 PIReg(&PLLReg);
73 w_PLL = fabs(PLLReg.out);
74 theta_PLL += Ts*w_PLL;
75 if(theta_PLL >= double_pi) theta_PLL -= double_pi;
76 if(theta_PLL < 0.0f) theta_PLL += double_pi;
77
78 // Sin Cos Calc
79 Sin_Cos_theta.sin = sinf(theta_PLL);
80 Sin_Cos_theta.cos = cosf(theta_PLL);
81
82 // Control states
83 switch(STATE) {
84
85     case ERROR:
86         // Counters initialization
87         counter = 0;
88         //Flags
89         PWM_EN = 0;
90         GRID_EN = 0;
91         PREC_EN = 0;
92         // Duty Cycles initialization
93         duty.a = 0.5f;
94         duty.b = 0.5f;
95         duty.c = 0.5f;
96         // Integrators initialization
```

```
97 VdcReg.integral = 0.0f;
98 IdReg.integral = 0.0f;
99 IqReg.integral = 0.0f;
100 // Wait for USER_BTN
101 if ( USER_BUTTON>0.5f ){
102     STATE = PRECHARGE;
103 }
104 break;
105
106 case PRECHARGE:
107     // Connection to grid
108     GRID_EN = 1;
109     // Precharge resistors are connected
110     PREC_EN = 1;
111     // Elapsed time update
112     counter++;
113     // This state persists until 90% of Vpk is reached. The minimum
time is 0.2s.
114     if ( (counter>2000) & (Vdc > 0.9*VgLL_pk) ){
115         counter = 0;
116         PREC_EN = 0;
117         STATE = SYNC;
118     }
119 break;
120
121 case SYNC:
122     counter++;
123     // This state persists until PLL is synced. The minimum time is
0.1s.
124     if ( (counter>1000) & (Vdq.q <= th_PLL) ){
125         counter = 0;
126         STATE = READY;
127     }
128 break;
129
130 case READY:
131     // Vdc ramp reference will start from the actual Vdc value.
132     VdcReg.ref = Vdc_filt;
133     // Wait for USER_BTN
```

```

134     if ( USER_BUTTON>0.5f ){
135         STATE = START;
136     }
137     break;
138
139     case START:
140
141         // Enable PWM
142         PWM_EN = 1;
143         // Elapsed time update
144         counter++;
145
146         // — DC-LINK VOLTAGE CONTROL —
147         // Reference changes with a ramp
148         Vdc_Target    = 400.0f;
149         Vdc_Slope     = Vdc_Target*Ts/0.5f; //0.1s to rise
150         SlewRateLimiter( &Vdc_Target , &Vdc_Slope , &VdcReg.ref );
151         // Regulator
152         VdcReg.actual  = Vdc_filt;
153         PIReg(&VdcReg);
154         IdReg.ref     = -1.0f*VdcReg.out*(2*one_third*VdcReg.ref/Vdq.d);
155
156         // —CURRENT CONTROL —
157         // References. Id reference comes from DC-Link control
158         IqReg.ref     = 5.0f;
159         // Current control - d axis
160         IdReg.actual  = Idq.d;
161         IdReg.vfw     = Vdq.d - wg*Lf*IqReg.ref;
162         IdReg.lim     = Vdc*2*sqrt3_inv;
163         PIReg(&IdReg);
164         Vdq_ref.d     = IdReg.out;
165         // Current control - q axis
166         IqReg.actual  = Idq.q;
167         IqReg.vfw     = Vdq.q + wg*Lf*IdReg.ref;
168         IqReg.lim     = sqrt(IdReg.lim*IdReg.lim - IdReg.ref*IdReg.ref);
169         if (IqReg.lim < 0.001) IqReg.lim = 0.001;
170         PIReg(&IqReg);
171         Vdq_ref.q     = IqReg.out;
172         // dq -> ab Transformation

```

```

173     InvRot(&Vdq_ref, &Sin_Cos_theta, &Vab_ref);
174     InvClarke(&Vab_ref, &Vabc_ref);
175
176     // — BOOST CONTROL —
177     // Reference. Ramp starts after 0.5s from control starting.
178     if (counter < 5000) {
179         IboostReg.ref      = 0.0 f;
180     } else {
181         Iboost_Target      = 10.0 f;
182         Iboost_Slope      = Iboost_Target*Ts/0.0001 f;
183         Iprec              = IboostReg.ref;
184         SlewRateLimiter( &Iboost_Target , &Iboost_Slope , &IboostReg.
ref );
185     }
186     // Regulator
187     IboostReg.actual      = Idc;
188     IboostReg.lim        = Vdc;
189     PIReg(&IboostReg);
190
191     // — DUTY CYCLES —
192     PWMCompute(&Vabc_ref, &duty, &Vdc);
193     duty_boost           = IboostReg.out/Vdc;
194     break;
195 }
196
197 // — OUTPUTS —
198 OutputSignal(0,1)      = duty.a;
199 OutputSignal(0,2)      = duty.b;
200 OutputSignal(0,3)      = duty.c;
201 OutputSignal(0,4)      = duty_boost;
202 OutputSignal(0,5)      = GRID_EN;
203 OutputSignal(0,6)      = PREC_EN;
204 OutputSignal(0,7)      = PWM_EN;

```

# Appendix D

## Signal Injection Insights

### (d,q) Impedance of an RL Circuit

The voltage-current relation for a RL circuit is:

$$\begin{cases} v_r = R \cdot i_r + L \cdot \frac{di_r}{dt} \\ v_s = R \cdot i_s + L \cdot \frac{di_s}{dt} \\ v_t = R \cdot i_t + L \cdot \frac{di_t}{dt} \end{cases} \quad (\text{D.1})$$

In a compact form (D.1) becomes:

$$\mathbf{V}_{rst} = \mathbf{R} \cdot \mathbf{I}_{rst} + \mathbf{L} \cdot \dot{\mathbf{I}}_{rst} \quad (\text{D.2})$$

where  $\dot{\mathbf{I}}$  is the time derivative of  $\mathbf{I}$  and:

$$\mathbf{V}_{rst} = \begin{bmatrix} v_r \\ v_s \\ v_t \end{bmatrix} \quad \mathbf{I}_{rst} = \begin{bmatrix} i_r \\ i_s \\ i_t \end{bmatrix} \quad \mathbf{R} = \begin{bmatrix} R & 0 & 0 \\ 0 & R & 0 \\ 0 & 0 & R \end{bmatrix} \quad \mathbf{L} = \begin{bmatrix} L & 0 & 0 \\ 0 & L & 0 \\ 0 & 0 & L \end{bmatrix} \quad (\text{D.3})$$

To switch to the  $(\alpha, \beta)$  frame, the amplitude invariant Clarke matrix  $\mathbf{A}$  is used. As for the currents:

$$\mathbf{I}_{\alpha\beta} = \mathbf{A} \cdot \mathbf{I}_{rst} \quad (\text{D.4})$$

$$\mathbf{I}_{rst} = \mathbf{A}^{-1} \cdot \mathbf{I}_{\alpha\beta} \quad (\text{D.5})$$

Since  $\mathbf{R} = \mathbf{R} \cdot \mathbf{I}$  and  $\mathbf{L} = \mathbf{L} \cdot \mathbf{I}$ , where  $\mathbf{I}$  is a 3x3 identity matrix, (D.2) can be expressed in the  $(\alpha, \beta, 0)$  frame as:

$$\begin{aligned}
 \mathbf{V}_{\alpha\beta 0} &= \mathbf{A} \cdot \mathbf{V}_{rst} \\
 &= \mathbf{A} \cdot \mathbf{R} \cdot \mathbf{A}^{-1} \cdot \mathbf{I}_{\alpha\beta 0} + \mathbf{A} \cdot (\mathbf{L} \cdot \mathbf{A}^{-1} \cdot \dot{\mathbf{I}}_{\alpha\beta 0}) \\
 &= \mathbf{R} \cdot \mathbf{A} \cdot \mathbf{A}^{-1} \cdot \mathbf{I}_{\alpha\beta 0} + \mathbf{L} \cdot \mathbf{A} \cdot \mathbf{A}^{-1} \cdot \dot{\mathbf{I}}_{\alpha\beta 0} \\
 &= \mathbf{R} \cdot \mathbf{I}_{\alpha\beta 0} + \mathbf{L} \cdot \dot{\mathbf{I}}_{\alpha\beta 0}
 \end{aligned} \tag{D.6}$$

Therefore  $\mathbf{R}$  and  $\mathbf{L}$  in the  $(\alpha, \beta, 0)$  frame are the same as in the three-phase frame. As said before, the homopolar component is neglected. Therefore  $\mathbf{R}$  and  $\mathbf{L}$  become 2x2 matrices.

For the  $(d, q)$  rotating frame, the rotation transformation matrix  $\mathbf{R}(\theta_r)$  is used:

$$\mathbf{V}_{dq} = \mathbf{R}(\theta_r) \cdot \mathbf{V}_{\alpha\beta} \tag{D.7}$$

$$\mathbf{V}_{\alpha\beta} = \mathbf{R}^{-1}(\theta_r) \cdot \mathbf{V}_{dq} = \mathbf{R}(-\theta_r) \cdot \mathbf{V}_{dq} \tag{D.8}$$

By replacing (D.8) into (D.6) the following is obtained:

$$\begin{aligned}
 \mathbf{V}_{\alpha\beta} &= \mathbf{R}(-\theta_r) \cdot \mathbf{V}_{dq} \\
 &= \mathbf{R} \cdot \mathbf{R}(-\theta_r) \cdot \mathbf{I}_{dq} + \mathbf{L} \cdot \frac{d(\mathbf{R}(-\theta_r))}{dt} \cdot \mathbf{I}_{dq}
 \end{aligned} \tag{D.9}$$

The latter term of (D.9) can be expressed as:

$$\mathbf{L} \cdot \frac{d(\mathbf{R}(-\theta_r) \cdot \mathbf{I}_{dq})}{dt} = \mathbf{L} \cdot \mathbf{I}_{dq} \cdot \frac{d\theta_r}{dt} \cdot \frac{d(\mathbf{R}(-\theta_r))}{d\theta} + \mathbf{L} \cdot \mathbf{R}(-\theta_r) \cdot \frac{d\mathbf{I}_{dq}}{dt} \tag{D.10}$$

since it can easily derived that:

$$\frac{d(\mathbf{R}(\theta_r))}{d\theta} = \mathbf{R}(\theta_r) \cdot \begin{bmatrix} 0 & -1 \\ 1 & 0 \end{bmatrix} \tag{D.11}$$

$\mathbf{R}(\theta_r)$  can be simplified from (D.9). Then by rewriting in the Laplace domain:

$$\mathbf{V}_{dq} = \mathbf{R} \cdot \mathbf{I}_{dq} + \omega_r \cdot \mathbf{L} \cdot \begin{bmatrix} 0 & -1 \\ 1 & 0 \end{bmatrix} \cdot \mathbf{I}_{dq} + s \cdot \mathbf{L} \cdot \mathbf{I}_{dq} \tag{D.12}$$

If  $\mathbf{I}_{dq}$  is collected:

$$\begin{bmatrix} v_d \\ v_q \end{bmatrix} = \begin{bmatrix} R + s \cdot L & -\omega_r \cdot L \\ \omega_r \cdot L & R + s \cdot L \end{bmatrix} \cdot \begin{bmatrix} i_d \\ i_q \end{bmatrix} \quad (\text{D.13})$$

## PLECS Voltage Perturbation Generation Code

The following code is used to automate the PLECS simulation process for a predefined set of positive and negative sequence voltage perturbations.

```

1  % — VOLTAGE INJECTION SCRIPT —
2
3  % Clear Octave console
4  plects('clc', 'clear')
5  % Initialize variables
6  mdlVars = struct('f_inj', 0.0, 'Vinj', 0.0, 'v_case', 'a', '
    inv_trig', 0);
7  Vg_pk   = 120*sqrt(2);
8  Vinj    = 0.1*Vg_pk;
9  fg      = 50.0;
10 simTime = 0.0;
11 simIter = 0;
12 % Define frequencies under test
13 F_inj    = logspace(0,3,35);
14 Lv      = length(F_inj);
15
16 % Simulate for every frequency
17 for i = 1:Lv
18     % Calculate simlatoon time
19     injStart = 0.3;
20     injTime  = 20/F_inj(i);
21     if (injTime < 1)
22         injTime = 1;
23     end
24     simTime   = injStart + injTime;
25     % Solver options
26     simOpt    = struct('StopTime', simTime);
27     % Set variables
28     mdlVars.f_inj = F_inj(i);

```

```

29     mdlVars.Vinj = Vinj;
30     % —— First test ——
31     mdlVars.inv_trig= 0;
32     mdlVars.v_case = 'a';
33     simIter      = simIter + 1;
34     simStruct    = struct('ModelVars', mdlVars, 'SolverOpts', simOpt)
35     ;
36     plecs('simulate', simStruct);
37     % —— Second test ——
38     mdlVars.inv_trig= 1;
39     mdlVars.v_case = 'b';
40     simIter      = simIter + 1;
41     simStruct    = struct('ModelVars', mdlVars, 'SolverOpts', simOpt)
42     ;
43     plecs('simulate', simStruct);
44 end

```

## PLECS Signal Perturbation Data Processing Code

The following code is used to process measurements obtained from signal perturbation tests.

```

1  % VOLTAGE INJECTION PROCESSING SCRIPT
2
3  clc , clear , close
4  addpath(genpath('lib/'));
5  data_folder = 'DATA_OUT';
6  % Used frequency vector
7  F_inj      = logspace(0,3.69897,35);
8  Lf         = length(F_inj);
9  % Vectors
10 Zdd = zeros(1, Lf);
11 Zqd = zeros(1, Lf);
12 Zdq = zeros(1, Lf);
13 Zqq = zeros(1, Lf);
14
15 % Open files
16 for k = 1:Lf
17

```

```

18 % —— Vd perturbation ——
19 filename = [ 'DATA_OUT_', num2str(F_inj(k), '%5.4f'), 'Hz_a.mat' ];
20 measures = load(fullfile(data_folder, filename));
21 % Save data in structures
22 t          = measures.data(1, :);
23 % Calculate sampling time
24 Ts         = mean(diff(t));
25 fs         = 1/Ts;
26 % Start only from significant part
27 Lt         = length(t);
28 tmax       = t(Lt);
29 T          = 1/F_inj(k);
30 dT         = 10*T;
31 t_s        = tmax - dT;
32 [~, s]     = min(abs(t - t_s));
33 % Save data
34 a_inj.t    = measures.data(1, s:Lt);
35 a_inj.irst.r = measures.data(2, s:Lt);
36 a_inj.irst.s = measures.data(3, s:Lt);
37 a_inj.irst.t = measures.data(4, s:Lt);
38 a_inj.vrst.r = measures.data(5, s:Lt);
39 a_inj.vrst.s = measures.data(6, s:Lt);
40 a_inj.vrst.t = measures.data(7, s:Lt);
41 a_inj.theta = measures.data(8, s:Lt);
42 clear measures
43 % Filter with moving average
44 f_ISR = 10e3;
45 mov_window = fs/f_ISR;
46 a_inj.irst.r = movmean(a_inj.irst.r, mov_window);
47 a_inj.irst.s = movmean(a_inj.irst.s, mov_window);
48 a_inj.irst.t = movmean(a_inj.irst.t, mov_window);
49 a_inj.vrst.r = movmean(a_inj.vrst.r, mov_window);
50 a_inj.vrst.s = movmean(a_inj.vrst.s, mov_window);
51 a_inj.vrst.t = movmean(a_inj.vrst.t, mov_window);
52 % Transform into alpha-beta
53 a_inj.vab = clarke_LL(a_inj.vrst);
54 a_inj.iab = clarke_PH(a_inj.irst);
55 % Transform into dq
56 a_inj.vdq = rot(a_inj.vab, a_inj.theta);

```

```

57     a_inj.idq = rot(a_inj.iab, a_inj.theta);
58     % Perform DFT
59     % Vd
60     [dft_calc.f, dft_calc.vd.amp, dft_calc.vd.phase] = dft(a_inj.vdq.d
, a_inj.t);
61     [~, index] = min(abs(dft_calc.f - F_inj(k)));
62     Vd1 = dft_calc.vd.amp(index)*exp(1i*dft_calc.vd.phase(index));
63     % Vq
64     [dft_calc.f, dft_calc.vq.amp, dft_calc.vq.phase] = dft(a_inj.vdq.q
, a_inj.t);
65     [~, index] = min(abs(dft_calc.f - F_inj(k)));
66     Vq1 = dft_calc.vq.amp(index)*exp(1i*dft_calc.vq.phase(index));
67     % Id
68     [dft_calc.f, dft_calc.id.amp, dft_calc.id.phase] = dft(a_inj.idq.d
, a_inj.t);
69     [~, index] = min(abs(dft_calc.f - F_inj(k)));
70     Id1 = dft_calc.id.amp(index)*exp(1i*dft_calc.id.phase(index));
71     % Iq
72     [dft_calc.f, dft_calc.iq.amp, dft_calc.iq.phase] = dft(a_inj.idq.q
, a_inj.t);
73     [~, index] = min(abs(dft_calc.f - F_inj(k)));
74     Iq1 = dft_calc.iq.amp(index)*exp(1i*dft_calc.iq.phase(index));
75     clear dft_calc
76
77     % — Vq perturbation —
78     filename = [ 'DATA_OUT_', num2str(F_inj(k), '%5.4f'), 'Hz_b.mat' ];
79     measures = load(fullfile(data_folder, filename));
80     % Save data
81     b_inj.t = measures.data(1, s:Lt);
82     b_inj.irst.r = measures.data(2, s:Lt);
83     b_inj.irst.s = measures.data(3, s:Lt);
84     b_inj.irst.t = measures.data(4, s:Lt);
85     b_inj.vrst.r = measures.data(5, s:Lt);
86     b_inj.vrst.s = measures.data(6, s:Lt);
87     b_inj.vrst.t = measures.data(7, s:Lt);
88     b_inj.theta = measures.data(8, s:Lt);
89     clear measures
90     % Filter with moving average
91     f_ISR =10e3;

```

```

92     mov_window = fs/f_ISR;
93     a_inj.irst.r = movmean(a_inj.irst.r, mov_window);
94     a_inj.irst.s = movmean(a_inj.irst.s, mov_window);
95     a_inj.irst.t = movmean(a_inj.irst.t, mov_window);
96     a_inj.vrst.r = movmean(a_inj.vrst.r, mov_window);
97     a_inj.vrst.s = movmean(a_inj.vrst.s, mov_window);
98     a_inj.vrst.t = movmean(a_inj.vrst.t, mov_window);
99     % Transform into alpha-beta
100    b_inj.vab = clarke_LL(b_inj.vrst);
101    b_inj.iab = clarke_PH(b_inj.irst);
102    % Transform into dq
103    b_inj.vdq = rot(b_inj.vab, b_inj.theta);
104    b_inj.idq = rot(b_inj.iab, b_inj.theta);
105    % Perform DFT
106    % Vd
107    [dft_calc.f, dft_calc.vd.amp, dft_calc.vd.phase] = dft(b_inj.vdq.d
, b_inj.t);
108    [~, index] = min(abs(dft_calc.f - F_inj(k)));
109    Vd2 = dft_calc.vd.amp(index)*exp(1i*dft_calc.vd.phase(index));
110    % Vq
111    [dft_calc.f, dft_calc.vq.amp, dft_calc.vq.phase] = dft(b_inj.vdq.q
, b_inj.t);
112    [~, index] = min(abs(dft_calc.f - F_inj(k)));
113    Vq2 = dft_calc.vq.amp(index)*exp(1i*dft_calc.vq.phase(index));
114    % Id
115    [dft_calc.f, dft_calc.id.amp, dft_calc.id.phase] = dft(b_inj.idq.d
, b_inj.t);
116    [~, index] = min(abs(dft_calc.f - F_inj(k)));
117    Id2 = dft_calc.id.amp(index)*exp(1i*dft_calc.id.phase(index));
118    % Iq
119    [dft_calc.f, dft_calc.iq.amp, dft_calc.iq.phase] = dft(b_inj.idq.q
, b_inj.t);
120    [~, index] = min(abs(dft_calc.f - F_inj(k)));
121    Iq2 = dft_calc.iq.amp(index)*exp(1i*dft_calc.iq.phase(index));
122    clear dft_calc
123
124    % Calculate voltage and current matrices
125    I = [Id1, Id2; Iq1, Iq2];
126    V = [Vd1, Vd2; Vq1, Vq2];

```

```
127 Z = V/I;  
128 Zdd(k) = Z(1,1);  
129 Zdq(k) = Z(1,2);  
130 Zqd(k) = Z(2,1);  
131 Zqq(k) = Z(2,2);  
132  
133 clear a_inj b_inj  
134 end
```

# Bibliography

- [1] Flexible Component Connection Method-Based Modeling of Grid-Connected Converters.
- [2] *EU reference scenario 2016 : energy, transport and GHG emissions : trends to 2050*. Publications Office of the European Union, August 2016.
- [3] Hirofumi Agaki, Edson Hirokazu Watanabe, and Mauricio Aredes. *Instantaneous Power Theory and Applications to Power Conditioning*. IEEE Press Series on Power Engineering. IEEE, April 2007.
- [4] Luis Amedo, Rolando Burgos, Fred Wang, and Dushan Boroyevich. Black-Box Terminal Characterization Modeling of DC-to-DC Converters. In *APEC 07 - Twenty-Second Annual IEEE Applied Power Electronics Conference and Exposition*, pages 457–463, February 2007. ISSN: 1048-2334.
- [5] Mohammad Amin and Marta Molinas. A Gray-Box Method for Stability and Controller Parameter Estimation in HVDC-Connected Wind Farms Based on Nonparametric Impedance. *IEEE Transactions on Industrial Electronics*, 66(3):1872–1882, March 2019.
- [6] Alberto Bemporad. *Identification, Analysis and Control of Dynamical Systems*, 2019.
- [7] R.I. Bojoi, G. Griva, V. Bostan, M. Guerriero, F. Farina, and F. Profumo. Current control strategy for power conditioners using sinusoidal signal integrators in synchronous reference frame. *IEEE Transactions on Power Electronics*, 20(6):1402–1412, November 2005.
- [8] Pantelis Capros, European Commission, Directorate-General for Energy and Transport, European Commission, Climate Action DG, European Commission, and Directorate General for Mobility and Transport. *EU reference scenario*

- 2016: *energy, transport and GHG emissions : trends to 2050*. Publications Office of the European Union, Luxembourg, 1 edition, 2016. OCLC: 971169468.
- [9] CEI. CEI 0-16: Regola tecnica di riferimento per la connessione di Utenti attivi e passivi alle reti AT ed MT delle imprese distributrici di energia elettrica, April 2019.
- [10] CEI. CEI 0-21: Regola tecnica di riferimento per la connessione di Utenti attivi e passivi alle reti BT delle imprese distributrici di energia elettrica, April 2019.
- [11] Gianfranco Chicco. Distributed Energy Resources.
- [12] Gerald Francis, Rolando Burgos, Dushan Boroyevich, Fred Wang, and Kamiar Karimi. An algorithm and implementation system for measuring impedance in the D-Q domain. In *2011 IEEE Energy Conversion Congress and Exposition*, pages 3221–3228, September 2011. ISSN: 2329-3748.
- [13] Jing Huang, Keith A. Corzine, and Mohamed Belkhatat. Small-Signal Impedance Measurement of Power-Electronics-Based AC Power Systems Using Line-to-Line Current Injection. *IEEE Transactions on Power Electronics*, 24(2):445–455, February 2009.
- [14] IEEE. IEEE Recommended Practice for Monitoring Electric Power Quality. *IEEE Std 1159-2019 (Revision of IEEE Std 1159-2009)*, page 98, August 1998.
- [15] International Energy Agency. *Global EV Outlook 2019: Scaling-up the transition to electric mobility*. OECD, June 2019.
- [16] Wei Liu, Xiaorong Xie, Xu Zhang, and Xuan Li. Frequency-coupling Admittance Modeling of Converter-Based Wind Turbine Generators and the Control-Hardware-in-the-Loop Validation. *IEEE Transactions on Energy Conversion*, pages 1–1, 2019.
- [17] Lennart Ljung. *System Identification: Theory for the User*. Prentice Hall, 2 edizione edition, 1998.
- [18] Lennart Ljung, Qinghua Zhang, Peter Lindskog, and Anatoli Juditsky. *System Identification Toolbox™ Getting Started Guide*, volume 1. The MathWorks, Inc., 26 edition, September 2019.
- [19] Fabio Mandrile. SSI Filter Exact Discretisation, August 2018.
- [20] Fabio Mandrile, Frede Blaabjerg, Enrico Carpaneto, Tomislav Dragicevic, and

- Radu Bojoi. Flexible Component Connection Method-Based Modeling of Grid-Connected Converters. 2020.
- [21] Fabio Mandrile and Radu Bojoi. Impedance Models of Power Electronics Converters.
- [22] Fabio Mandrile and Enrico Carpaneto. S-VSC Linearized State Space Representation, 2020.
- [23] Fabio Mandrile, Enrico Carpaneto, and Radu Bojoi. Grid-Tied Inverter with Simplified Virtual Synchronous Compensator for Grid Services and Grid Support. 2019.
- [24] Marta Molinas. Impedance-based Stability Evaluation of power electronics dominated power systems, January 2019.
- [25] E. Mollerstedt and B. Bernhardsson. Out of control because of harmonics-an analysis of the harmonic response of an inverter locomotive. *IEEE Control Systems Magazine*, 20(4):70–81, August 2000.
- [26] Matteo Pasqualini. *Impedance Models of Grid-Tied Converters*. Politecnico di Torino, March 2020.
- [27] Atle Rygg, Marta Molinas, Chen Zhang, and Xu Cai. A Modified Sequence-Domain Impedance Definition and Its Equivalence to the dq-Domain Impedance Definition for the Stability Analysis of AC Power Electronic Systems. *IEEE Journal of Emerging and Selected Topics in Power Electronics*, 4(4):1383–1396, December 2016.
- [28] Alex Simpkins. System Identification: Theory for the User, 2nd Edition (Ljung, L.; 1999) [On the Shelf]. *IEEE Robotics Automation Magazine*, 19(2):95–96, June 2012.
- [29] Jian Sun. Impedance-Based Stability Criterion for Grid-Connected Inverters. *IEEE Transactions on Power Electronics*, 26(11):3075–3078, November 2011.
- [30] Remus Teodorescu, Marco Liserre, and Pedro Rodriguez. *Grid Converters for Photovoltaic and Wind Power Systems*, volume 1 of *Wiley - IEEE*. John Wiley & Sons Inc, 1 edition, 2011.
- [31] TERNA. Allegato A70 al Codice di Rete, August 2012.
- [32] TERNA. Allegato A17 al Codice di Rete, July 2018.
- [33] TERNA. Allegato al Codice di Rete A68, July 2018.

- [34] Virgilio Valdivia, Andrés Barrado, Antonio LÁzaro, Pablo Zumel, Carmen Raga, and Cristina FernÁndez. Simple Modeling and Identification Procedures for “Black-Box” Behavioral Modeling of Power Converters Based on Transient Response Analysis. *IEEE Transactions on Power Electronics*, 24(12):2776–2790, December 2009.
- [35] Virgilio Valdivia, Antonio LÁzaro, Andrés Barrado, Pablo Zumel, Cristina FernÁndez, and Marina Sanz. Impedance Identification Procedure of Three-Phase Balanced Voltage Source Inverters Based on Transient Response Measurements. *IEEE Transactions on Power Electronics*, 26(12):3810–3816, December 2011.
- [36] Xiongfei Wang and Frede Blaabjerg. Harmonic Stability in Power Electronic-Based Power Systems: Concept, Modeling, and Analysis. *IEEE Transactions on Smart Grid*, 10(3):2858–2870, May 2019. Conference Name: IEEE Transactions on Smart Grid.
- [37] Bo Wen, Dushan Boroyevich, Rolando Burgos, Paolo Mattavelli, and Zhiyu Shen. Analysis of D-Q Small-Signal Impedance of Grid-Tied Inverters. *IEEE Transactions on Power Electronics*, 31(1):675–687, January 2016.
- [38] Bo Wen, Dushan Boroyevich, Paolo Mattavelli, Zhiyu Shen, and Rolando Burgos. Influence of phase-locked loop on input admittance of three-phase voltage-source converters. In *2013 Twenty-Eighth Annual IEEE Applied Power Electronics Conference and Exposition (APEC)*, pages 897–904, March 2013. ISSN: 1048-2334.
- [39] Bo Wen, Dong Dong, Dushan Boroyevich, Rolando Burgos, Paolo Mattavelli, and Zhiyu Shen. Impedance-Based Analysis of Grid-Synchronization Stability for Three-Phase Paralleled Converters. *IEEE Transactions on Power Electronics*, 31(1):26–38, January 2016.
- [40] Bo Wen, Dong Dong, Dushan Boroyevich, Rolando Burgos, Paolo Mattavelli, and Zhiyu Shen. Impedance-Based Analysis of Grid-Synchronization Stability for Three-Phase Paralleled Converters. *IEEE Transactions on Power Electronics*, 31(1):26–38, January 2016.